Modeling, Design, and Fabrication of Spectrally-Selective Mirrors for Photovoltaic Thermal Management

A DISSERTATION

SUBMITTED TO THE FACULTY OF THE

UNIVERSITY OF MINNESOTA

BY

Ian McClurg Slauch

In Partial Fulfilment of the Requirements for the Degree of

DOCTOR OF PHILOSOPHY

Vivian E. Ferry, Advisor

July, 2020

Acknowledgements

During my time at the University of Minnesota, I have received the wonderful support and guidance of many people, without whom my experience here would not have been nearly as memorable.

I would first like to thank my advisor, Vivian Ferry, who has provided invaluable mentorship and advice throughout my time as a graduate student. Her obvious passion for research and her desire to constantly explore new questions and ideas has been inspirational. She has helped me to become a better scientist, teacher, and mentor. I am also very grateful for my collaborators at the National Renewable Energy Laboratory, Michael Deceglie and Tim Silverman, who have provided enormous support, not just with their time, advice, and suggestions, but who, along with Sarah Kurtz, made my internship at NREL unforgettable. My thanks also goes to Ed Cussler, Michael Harris, and Turan Birol, with whom I have worked as a teaching assistant during several of my semesters here. I would also like to thank Russell Holmes, Lorraine Francis, and James Leger as members of my doctoral thesis committee.

In my time at the University of Minnesota, I have worked and studied alongside many talented and devoted students. My thanks goes to current and former members of the Ferry group, Ryan Connell, Dana Dement, Matthew Quan, Pavlos Pachidis, and John Caputo. Ryan, Dana, and Matt, as senior students in the lab have been endless sources of advice for any number of topics, be it experiments, coding bugs, or qualifying exams. I would like to thank Dana in particular for her assistance with ellipsometry measurements, and surface probe microscopy. I thank Matt for his help with imaging using the visible microscope, and I thank Ryan for fixing many errors in my Lumerical simulations. Pavlos and John, who joined the Ferry group at the same time as I, have provided immeasurable help to me over the past five years. Whether in class, in the office, in the lab, or at the gym, they were always at my side. John I would like to thank for teaching me gold nanorod synthesis and use of the TEM. Pavlos I would like to thank especially for his assistance on many problem sets in the classes we shared, and for the sometimes fruitful, sometimes trivial discussion in the office. I also thank Bryan Cote for his help developing far-field scattering and multipole decomposition calculations. Finally, I would like to especially thank all members

of the Ferry group, including Christian Pinnell, Eleanor Mayes, John Keil, Maya Ramamurthy, Rohan Chakraborty, Mayank Puri, Sihoon Moon, Sydney Jones, Willa Mihalyi-Koch, Will Broomhead, and Jessica Chiu.

At the University of Minnesota and in the Department of Chemical Engineering and Materials Science, there are many outstanding staff members who have helped me throughout my time here. I would like to thank Julie Prince and Teresa Bredahl, who do a fantastic job coordinating many of the department events, and who have helped me many times to solve administrative issues. Special thanks goes to staff members at the Minnesota Nano Center, including Paul Kimani and Robert Amundson, who helped to train me and advise me on equipment for thin film deposition. I also thank Jason Myers and Nicholas Seaton at the Characterization Facility for training and assistance with electron microscopy, and Greg Haugstad for scanning probe microscopy measurements.

I am extremely grateful for the support provided by friends, who have made my experience here one filled with fond memories. Whether on the softball field, at the department round table, on a trip downtown, or at a Twins game, they have always provided me with laughs and smiles. Lastly, I thank my parents and my sister, for their constant love and encouragement.

Abstract

A typical c-Si photovoltaic module will operate 20-30K above ambient temperature due to waste heat generated as it converts incident sunlight into electrical power. As temperature increases, the conversion efficiency drops by ~0.4%/K, reducing overall power output. Reducing the total amount of waste heat generated during operation would both lower the module operating temperature and improve its efficiency and energy yield.

Waste heat is generated in the module in part due to parasitic absorption of sub-bandgap light that does not have enough energy to be useful for power conversion. Sub-bandgap reflection offers a method of preventing parasitic absorption, cooling the module, and increasing its efficiency. In this thesis, a time-independent matrix model is introduced to calculate module energy yield and waste heat generation through parasitic absorption, recombination, and electronic losses. The model considers the spectral and angular dependence of the optical properties of the module including modification by photonic structures, and is used to characterize and optimize the design of aperiodic photonic mirrors which selectively reflect sub-bandgap light from the module and enhance its energy yield. Importantly, these mirrors are designed considering weather and irradiance conditions typical for outdoor fixed-tilt module installations. As a result, it is shown that these mirrors are omnidirectional, achieving the required spectral selectivity regardless of the angle of incidence of sunlight or the geographic location of installation.

Low-complexity mirror designs which are simple to fabricate offer the most potential for reducing the cost of energy. These designs are primarily anti-reflection coatings, but also avoid a rise in operating temperature while increasing energy output. Two simple designs are fabricated, integrated into modules, and tested outdoors. The fabricated mirrors have the desired spectral selectivity, and reduce module operating temperature by over 1K.

Alternative strategies to reject sub-bandgap light, including reflection from the cell surface or cell rear contact, and backscattering from near the cell are also modeled and compared to result for reflection from the glass. Designing for the glass interface in particular allows maximization of the dual benefit, optical and thermal, of the mirrors.

Table of Contents

List of Tables

List of Figures

List of Publications

Portions of this thesis are drawn from:

(1) Slauch, I. M.; Deceglie, M. G.; Silverman, T. J.; Ferry, V. E. Spectrally Selective Mirrors with Combined Optical and Thermal Benefit for Photovoltaic Module Thermal Management. *ACS Photonics* **2018**, *5*, 1528–1538.

(2) Slauch, I. M.; Deceglie, M. G.; Silverman, T. J.; Ferry, V. E. Model for Characterization and Optimization of Spectrally Selective Structures to Reduce the Operating Temperature and Improve the Energy Yield of Photovoltaic Modules. *ACS Appl. Energy Mater.* **2019**, *2* (5), 3614–3623. https://doi.org/10.1021/acsaem.9b00347.

(3) Slauch, I. M.; Deceglie, M. G.; Silverman, T. J.; Ferry, V. E. Performance of Low-Complexity Spectrally Selective One-Dimensional Mirrors for Photovoltaic Thermal Management. In *2018 IEEE 7th World Conference on Photovoltaic Energy Conversion, WCPEC 2018 - A Joint Conference of 45th IEEE PVSC, 28th PVSEC and 34th EU PVSEC*; Institute of Electrical and Electronics Engineers Inc., **2018**; pp 2933–2938. https://doi.org/10.1109/PVSC.2018.8547965.

(4) Slauch, I. M.; Deceglie, M. G.; Silverman, T. J.; Ferry, V. E. Two-Layer Anti-Reflection Coatings with Optimized Sub-Bandgap Reflection for Solar Modules. In *New Concepts in Solar and Thermal Radiation Conversion and Reliability*; International Society for Optics and Photonics, **2018**; Vol. 10759, p 1075911. https://doi.org/10.1117/12.2323145.

(5) Slauch, I. M.; Deceglie, M. G.; Silverman, T. J.; Ferry, V. E. Outdoor Testing of C-Si Photovoltaic Modules with Spectrally-Selective Mirrors for Operating Temperature Reduction. In *Proceedings of the 46th IEEE PVSC*; Institute of Electrical and Electronics Engineers Inc.: Chicago, IL, **2019**.

Chapter 1 Introduction

1.1. Motivation

Solar energy is an attractive method of providing renewable power at the residential, commercial, and industrial scales. Solar photovoltaic installations worldwide continue to increase, while costs decrease. However, further expansion of solar energy requires reductions in the cost of energy to ~$0.03/kWh.[1] Technologies which boost the power output of photovoltaic modules can drive cumulative installations into the TW range, and allow photovoltaic energy to remain cost-competitive with traditional utility-scale energy sources.[2]

One main challenge limiting photovoltaic energy is the relatively low conversion efficiency of sunlight into energy. Therefore, most of the energy absorbed in a photovoltaic module generates heat instead of power. This heat causes the module temperature to rise 20-30K above the ambient temperature during operation, which in turn reduces its conversion efficiency.[3] Strategies to cool photovoltaic modules during operation can raise the efficiency of the module, increase its power output, delay degradation due to moisture ingress[4] or solder failure,[5] and increase service lifetime.[6] In particular, some waste heat is generated by parasitic absorption of sunlight in the module. Elimination of this parasitic absorption would reduce the module temperature and boost efficiency without compromising energy production. For a c-Si photovoltaic module, ~19% of the incident energy cannot be used for electricity generation and can only be parasitically absorbed. Reflection of this light, at wavelengths of ~1200 nm and longer, will reduce the waste heat generated.

Existing optical coatings commonly used in photovoltaic modules do not address this issue. A standard single-layer anti-reflection coating (ARC) on the glass of the module increases the energy yield by reducing reflection losses over useful incident wavelengths, but does not decrease, and in fact increases, the waste heat produced. A more sophisticated coating design would selectively reflect long wavelength, sub-bandgap light while also improving anti-reflection at shorter wavelengths compared to existing single-layer ARCs. However, designing such a coating is not straightforward. The incident sunlight arrives at

a time-varying angle of incidence upon the module, depending on the time of day and the time of year. Furthermore, the module collects both direct and diffuse light, which in general arrive from all possible directions. The optical coating, then, must successfully operate regardless of the angle of incidence of sunlight (see **Figure 1.1**).

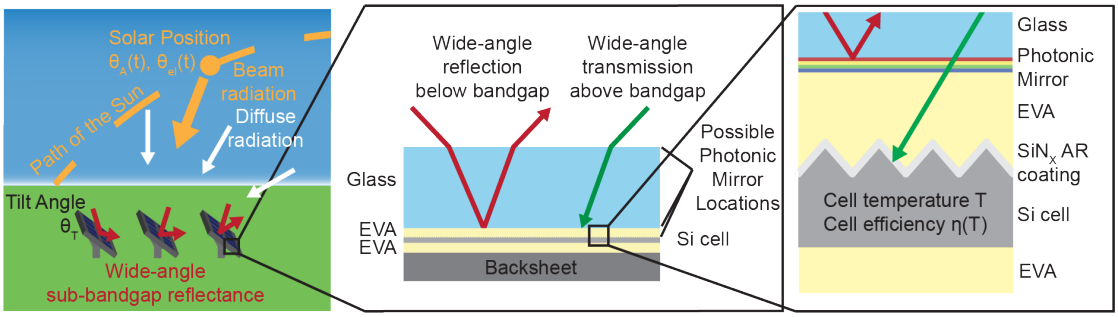

***Figure 1.1**: Schematic showing the operation of a spectrally-selective mirror in a photovoltaic module. (Left) The module receives both direct and diffuse light over all angles of incidence, depending on the time of day and year, and must be designed for wide-angle sub-bandgap reflectance. (Middle) In addition, the coating must transmit light above the bandgap across all angles as well, to avoid interfering with module current production. (Right) Inset showing the photonic mirror between the glass and encapsulant. The mirror could also be located on top of the module glass.*

To design these coatings, modeling which captures their optical properties is required. A more typical reflective coating consisting of quarter-wavelength films of alternating materials, known as a Bragg stack, will not suffice due to reflection outside of the main band.[7] Recent efforts[8,9] have shown that aperiodic 1-D photonic mirrors can simultaneously improve upon existing ARCs while providing sub-bandgap reflection and thermal management. Arriving at such an aperiodic design, however, requires a model which accounts for the wavelength and angle dependent properties of mirrors composed of real materials, projected over an entire year of simulated outdoor operation. Ideally, this model would be quick to compute, and focus on maximizing the module energy yield increase due to both the anti-reflective and reflective aspects of the mirror.

While photonic mirrors can provide the desired reductions in waste heat and improvement in energy yield of photovoltaic modules, their ability to reduce the cost of energy requires that they be cheaply and easily fabricated. Another challenge of photonic mirror design, then, is obtaining the required spectral selectivity and angle insensitivity regardless of the simplicity of the final design. Candidate designs can then be fabricated and tested to determine their effectiveness in an outdoor installation.

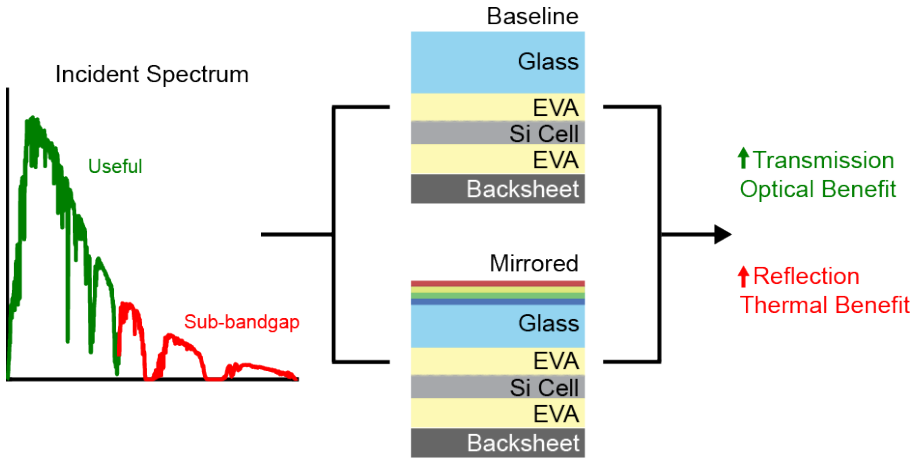

***Figure 1.2**: Schematic showing the goals of a model to optimize aperiodic photonic mirrors. Both optical benefit from transmission of useful sunlight, and thermal benefit from reflection of sub-bandgap light are included.*

1.2. Photovoltaic Operating Principles

1.2.1 The Solar Spectrum

Most locations in the United States receive 4-6 kWh m^{-2} day^{-1} total sunlight at ground level.[10] The solar spectral power (the solar power at each wavelength of light per unit wavelength) is similar to the spectral power of a blackbody at ~5500 °C.[11] However, the exact spectral composition reaching the ground depends on many factors, including the time of day and time of year, geographic location, ambient pressure and temperature, humidity, and particle content.[12] For simplicity, modeling and calculations involving absorption of sunlight often assume a standard spectrum representative of typical conditions at the Earth's surface.[13] In this work, the AM1.5G spectrum will represent all incident sunlight, and is plotted versus wavelength in **Figure 1.3**.

The 'AM' in AM1.5G stands for 'Air Mass,' a measure of the relative thickness of atmosphere through which sunlight must pass to arrive at the ground. AM1.5 radiation must pass through 1.5 times the thickness of the atmosphere, which occurs when the solar zenith angle is ~48.19°.[13,14] The AM1.5G Spectrum refers to global irradiance, in the sense that sunlight incident from all directions is included. The total power in the AM1.5G spectrum is ~1000 Wm^{-2}, with ~900 Wm^{-2} coming directly from the Sun, and the remainder being diffuse light from all other directions.[15] The AM1.5G spectrum differs from the

blackbody-like spectrum incident on the Earth's upper atmosphere because of absorption and scattering of light. Rayleigh scattering[16] and ozone absorption reduce the amount of blue and UV light reaching the surface, while absorption by water and CO_2 reduce atmospheric transmission in some bands of the infrared.[17]

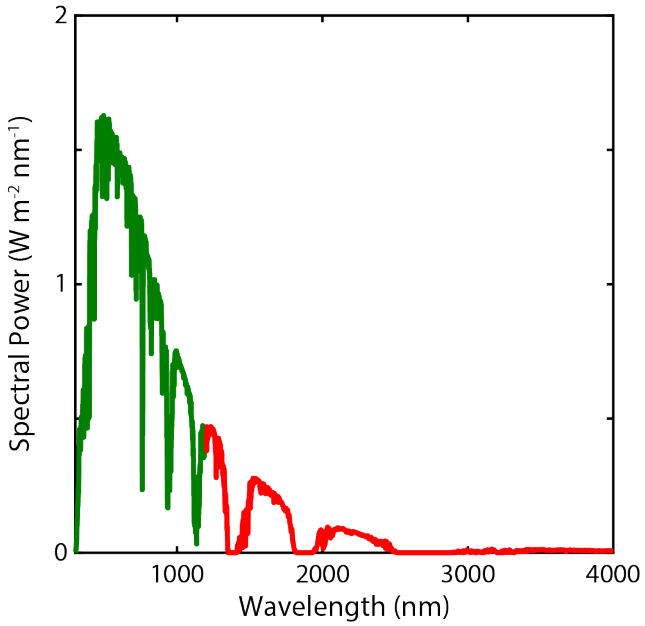

***Figure 1.3**: The AM1.5G spectrum, with the green curve at wavelengths with energy above the c-Si bandgap, and the red curve at wavelengths with energy below the c-Si bandgap.*

The power in the AM1.5G spectrum is assumed to pass through a plane which points at the Sun. Should a plane of interest such as the surface of a photovoltaic module point in some other direction, the total solar flux reaching the module is reduced by a geometric factor. Additionally, if the sky is overcast, then the total irradiance reaching the ground is also reduced. Changes in the level of irradiance are measured by e.g. the NREL Solar Radiation Research Laboratory[18] or given as historical data in the Typical Meteorological Year data sets,[19] and are incorporated into models used in this work. However, an air mass other than 1.5, or overcast skies, will shift the solar spectral power as well. Shifts in the shape of the solar spectrum versus time are not included in the modeling efforts presented here.

1.2.2 Photovoltaic Cell Absorption, Photocurrent, and Voltage

The vital element of a photovoltaic cell is the semiconductor, which absorbs sunlight as its valence electrons are excited across a bandgap. The bandgap is a range of energies over which the density of states, the number of available states which electrons can occupy, is zero.[20] Electrons in the valence band below the edge of the bandgap can gain energy greater than the bandgap and move to the conduction band, or relax across the bandgap while losing energy, but they cannot exist at an energy within the bandgap.[21] This work focuses on photovoltaic cells using crystalline silicon (c-Si), which has a bandgap spanning ~1.12 eV. Semiconductors commonly used in photovoltaic cells have bandgap energies that are similar in energy to the photons in sunlight. The energy, E, of a photon with wavelength λ is given in eq. 1.1, where h is the Planck constant and c is the speed of light.

$$E = \frac{hc}{\lambda} \tag{1.1}$$

Table 1.1 lists some common semiconductors, their bandgaps in units of electron volts (eV), and the wavelengths of light corresponding to that energy. For c-Si, this wavelength is between 1100 and 1200 nm; at longer wavelengths c-Si is transparent. Light which does not have enough energy to promote electrons across the bandgap is called 'sub-bandgap light.' For the c-Si bandgap, the corresponding portion of the AM1.5G spectrum is given by the red curve in **Figure 1.3**.

Table 1.1: Bandgap energies and wavelengths for common semiconductor materials[22]

Material	Bandgap (eV)	Wavelength (nm)
c-Si	1.12	1110
GaAs	1.43	870
CdTe	1.49	830
Ge	0.67	1870

Light with energy above the bandgap, shown as the green curve of the AM1.5G spectrum for c-Si, can be absorbed in the semiconductor. When this occurs, an electron is excited from the valence band to the conduction band. In a photovoltaic cell, electrons excited in this manner may be collected as photocurrent.[23] Depending on the wavelength of light and the design of the cell, the internal quantum efficiency (IQE), or the ratio of

charge carriers collected to photons absorbed, varies.[24] With known internal quantum efficiency, the photocurrent density, J_{ph} can be calculated using eq. 1.2.

$$J_{ph} = \int \varphi(\lambda) \cdot IQE(\lambda) \cdot \big(1 - R(\lambda)\big) d\lambda \tag{1.2}$$

Here, $\varphi(\lambda)$ is the incident spectral photon flux and R is the reflection. The photon flux is related to the spectral power $P(\lambda)$ as shown in eq. 1.3.

$$P(\lambda) = \varphi(\lambda)E = \varphi(\lambda)\frac{hc}{\lambda} \tag{1.3}$$

A quantity related to IQE is the external quantum efficiency (EQE), the ratio of carriers collected to incident photons (as opposed to absorbed photons). Typically, IQE is determined from measurements of EQE.[25] In this work, IQE is more relevant, as it is independent of optical modifications which change reflection and subsequently EQE.

$$IQE(\lambda) = \frac{EQE(\lambda)}{1 - R(\lambda)} \tag{1.4}$$

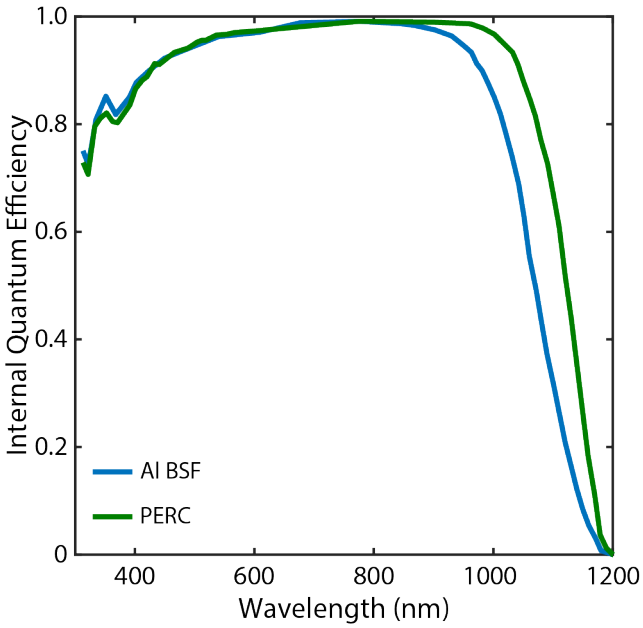

***Figure 1.4**: Internal Quantum Efficiency (IQE) of two c-Si cell types, Aluminum Back Surface Field (Al BSF) and Passivated Emitter Rear Contact (PERC). Data taken from Gatz et al.[26]*

Figure 1.4 gives as examples of IQE for two c-Si cell types, Aluminum Back Surface Field (Al BSF) and Passivated Emitter Rear Contact (PERC).[26] The solar absorber, c-Si, is the same for each cell, yet the PERC cell has improved IQE at longer wavelengths where

c-Si is a weak absorber. This difference affects the cell efficiency and operating temperature, which will be discussed further in Chapter 7.

The current density produced by a photovoltaic cell depends on the applied voltage, V, and can be approximated by the Shockley diode equation.[27]

$$J = J_{ph} - J_0\left(exp\left(\frac{qV}{mk_bT}\right) - 1\right) \tag{1.5}$$

In eq. 1.5, q is the elementary charge, k_B is the Boltzmann constant, and T is the absolute temperature. The combination k_BT/q is the thermal voltage, J_0 is the dark current, and m is an ideality factor that simplifies to 1 in the case of an ideal photovoltaic cell. A cell is typically characterized by its open circuit voltage, V_{oc}, and short circuit current density, J_{sc}. Open circuit voltage can be found by setting current equal to zero in eq. 1.5 and solving for the voltage.[28] The short-circuit current density is approximately equal to the photocurrent density J_{ph} in eq. 1.2.

$$V_{oc} = \frac{k_BT}{q} ln\left(\frac{J_{sc}}{J_o}\right) \tag{1.6}$$

The maximum power point, W_{mp}, where the product of J and V is largest, and the cell produces the most power. The maximum power point is related to the open-circuit voltage and short-circuit current density through the fill factor FF.[21,29]

$$W_{mp} = V_{mp}J_{mp} = V_{oc}J_{sc}FF \tag{1.7}$$

Finally, the cell efficiency, η, is defined by the ratio of the maximum power output to the incident power.

$$\eta = \frac{W_{mp}}{P_{in}} = \frac{V_{oc}J_{sc}FF}{P_{in}} \tag{1.8}$$

1.2.3 Temperature Effects

The properties of semiconductors and the performance of a photovoltaic cell are sensitive to their temperature. The efficiency of the cell depends on temperature,[30,31] which can be described using a temperature coefficient of efficiency, β, as in eq. 1.9.

$$\eta(T) = \eta_0(1 + \beta(T - T_0)) \tag{1.9}$$

For c-Si cells, $\beta \approx -0.39\,\%/K$, indicating that cell efficiency decreases with temperature. The temperature coefficient of efficiency can be broken down into the sum of temperature coefficients of open circuit voltage, short circuit current, and fill factor.[3]

$$\beta = \frac{1}{W_{mp}}\frac{dW_{mp}}{dT} = \frac{1}{V_{oc}}\frac{dV_{oc}}{dT} + \frac{1}{J_{sc}}\frac{dJ_{sc}}{dT} + \frac{1}{FF}\frac{dFF}{dT} = \beta_{Voc} + \beta_{Jsc} + \beta_{FF} \tag{1.10}$$

The majority of the decrease in efficiency with temperature is due to a decrease in open circuit voltage, which in turn depends on the dark current density. As temperature increases, the thermal energy allows more carriers to be excited across the bandgap, which increases the dark current density. The temperature dependence of the dark current density can be expressed following eq. 1.11,[32] where B is a constant, γ is a constant that depends on the recombination rate,[33] and E_{g0} is the bandgap energy extrapolated to zero temperature. Inserting eq. 1.11 into eq. 1.6 and differentiating gives the temperature dependence of open circuit voltage.

$$J_0 = BT^{\gamma} exp\left(\frac{-E_{g0}}{k_B T}\right) \tag{1.11}$$

$$\frac{dV_{oc}}{dT} \approx -\frac{\frac{E_{g0}}{q} - V_{oc} + \gamma\frac{k_B T}{q}}{T} \tag{1.12}$$

The dominant term in eq. 1.12 is $\frac{E_{g0}}{q} - V_{oc}$, with $\gamma\frac{k_B T}{q}$ accounting for up to 10% of the magnitude of the expression.[3] Additionally, dependence on J_{sc} has been ignored. Plugging in values gives $\frac{dV_{oc}}{dT} \approx 2\ mV/K$.

The short circuit current density increases with temperature because the bandgap decreases with temperature.[34] Therefore, a slightly larger fraction of the incident solar spectrum can excite electrons into the conduction band, generating more carriers overall. Measurement of β_{Jsc} is difficult, as the result depends strongly on the incident spectrum. Indoor measurements made with solar simulators may give different results than what would be seen under the AM1.5G spectrum.[3] Hishikawa *et al.*[35] provide a correction for spectral mismatch, and report $\beta_{Jsc} \approx 0.04\%/K$ for several c-Si cells.

The temperature coefficient of fill factor depends mainly on β_{Voc}, but also on the series resistance, $\mathcal{R}_s$, of the cell, which can become significant if resistance is large.[36,37]

$$\beta_{FF} = (1 - 1.02FF_0)\left(\beta_{Voc} - \frac{1}{T}\right) - \frac{\mathcal{R}_S}{\frac{V_{oc}}{I_{sc}} - \mathcal{R}_S}\frac{1}{\mathcal{R}_S}\frac{d\mathcal{R}_S}{dT} \quad (1.13)$$

$$FF_0 = \frac{v_{oc} - ln(v_{oc} + 0.72)}{v_{oc} + 1} \quad (1.14)$$

$$v_{oc} = \frac{qV_{oc}}{mk_BT} \quad (1.15)$$

Here, FF_0 is an empirical function of the reduced open circuit voltage, v_{oc}, representing the fill factor of an ideal solar cell.[23] A typical value for the temperature coefficient of fill factor is $\beta_{FF} \approx 0.14\%/K$.[37]

It is clear from the discussion above that the temperature coefficient of efficiency, a key component in modeling photovoltaic module power output, depends not only on intrinsic properties of silicon, but also properties of the cell itself. Recently reported temperature coefficients for c-Si cells range from -0.48 %/K to -0.34 %/K.[37–39]

1.3. Cell and Module Design and Energy Budget

Commercial c-Si photovoltaic cells and modules are designed to absorb as much light as possible in the cell and convert it to current, using materials and processing techniques that are amenable to rapid manufacturing and low cost. However, not all of the useful light above the bandgap is collected, and not all of the energy in those photons is extracted from the module. Furthermore, significant waste heat is produced from light at all wavelengths, including sub-bandgap light which cannot be converted in the cell. The designs of the cell and module determine their optical properties, the amount of power and waste heat produced, and the limits to improvement possible by modification using a photonic structure.

1.3.1 Design of c-Si Photovoltaic Cells

Figure 1.5 shows a schematic cross section of a typical cell. Ideally, all sunlight that can be absorbed by the Si to promote an electron across the bandgap will be absorbed in the cell. However, Si is a poor absorber of light >900 nm in wavelength, meaning that light at those wavelengths may have to travel a distance greater than the cell thickness before absorption. Additionally, Si has a high refractive index $n \sim 3.5$,[40] with a polished surface reflecting ~30% of incident visible light. A key feature of c-Si photovoltaic cells is front

surface texturing, which increases the path length inside the cell and reduces reflection at the front surface.[41] A SiN_x anti-reflection coating is added to the front textured surface to further reduce reflection, and also passivate the front surface to reduce recombination and increase efficiency.[42] The front texture is formed by wet chemical etching with hydroxide, exposing {111}-type planes. As a result, the texture forms a random arrangement of pyramids several microns in height. The {111}-type planes in c-Si make a 54.74° angle with respect to the base ([100] plane), however in practice the etching produces pyramidal texture with a slightly lower slope angle 48°-52°.[43,44] Between the texture and the anti-reflection coating, >99% of incident light near 600 nm is transmitted into the cell. The cell itself is ~180 μm thick, to balance between optical absorption and material cost.

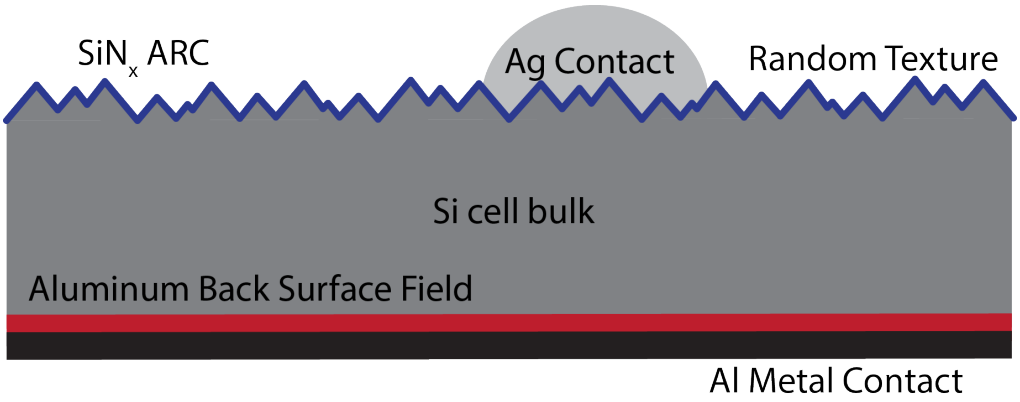

***Figure 1.5**: Schematic of a c-Si Al BSF cell. The random front pyramid texture and SiN_x ARC decrease reflection. The Ag front contact collects current and can reflect some light from the cell. The Al BSF at the cell rear absorbs some of the light which reaches it.*

The cell front and rear contacts are usually made with Ag (in the form of Ag paste) and Al, respectively. The front contacts form fingers on the cell front surface and, together with busbars, collect current. The fingers and busbars shade ~5% of the front cell area, and reflect some light away from the cell. The rear contact forms a back surface field (BSF) which passivates the rear and improves current density.[45] The rear surface is rough, and scatters incident light which further increases the path length within the cell. The back surface field contains a eutectic mixture of Al and Si which will absorb some light at all wavelengths, and is responsible for most parasitic absorption within the cell. The schematic in **Figure 1.3** shows a cell with a full area Al BSF. A more recent cell design, the passivated emitter rear contact (PERC) cell, uses dielectric passivation over most of the rear surface

area, which reduces parasitic absorption near and below the bandgap, and increases cell efficiency.[41,46]

1.3.2 Module Design

The module houses the cell to protect it mechanically, insulate it electrically, and shield it from weathering. Ideal module materials would be transparent from 300-1200 nm to allow all incident light into the cell. Commercial c-Si modules encapsulate the cell in ~400 μm of ethyl vinyl acetate (EVA) polymer placed behind a 3.2mm thick low-Fe glass sheet. **Figure 1.6** shows a picture of c-Si cell encapsulated behind glass and EVA. Iron impurities in the glass must be removed to prevent parasitic absorption above the bandgap.[47] Still, both the glass and EVA encapsulant will absorb UV light, and incident light <360 nm does not reach the cell. Over time, this leads to yellowing of the encapsulant and reduction in module power output.[48] Often, the glass will be coated with an anti-reflection coating to increase transmission into the module.

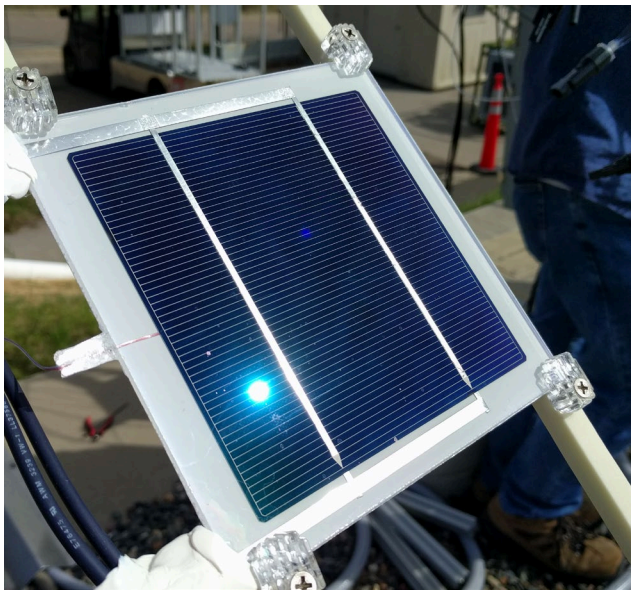

***Figure 1.6**: A single-cell module mounted outdoors. The cell is encapsulated behind 3.2 mm low-Fe glass and 400 μm EVA polymer. Photo taken by Michael Deceglie at NREL.*

In the sub-bandgap spectral range, the glass and EVA are not transparent. The EVA in particular is thick enough to absorb some or all incident light, depending on the wavelength.[49] These wavelengths could never be used to produce current, but the waste heat produced is still detrimental.

1.3.3 Energetic Pathways in c-Si Photovoltaic Modules

Proper modeling of module operation requires accounting for all pathways for energy in the module. Broadly speaking, sunlight incident on a photovoltaic module is either reflected or absorbed (although bifacial modules allow some transmission). However, only a fraction of the energy of the light absorbed is extracted from the module, the rest is wasted as heat. Useful energy is extracted as electrical current produced at the operating voltage of the module, which depends on the cell electrical properties. Polman and Atwater[50] provide an approximate expression for the open-circuit voltage, or the maximum possible chemical potential of an electron-hole pair.

$$qV_{oc} = E_g\left(1 - \frac{T}{T_{Sun}}\right) - k_B T\left[ln\left(\frac{\Omega_{emit}}{\Omega_{Sun}}\right) + ln\left(\frac{4n^2}{\xi}\right) - ln\left(\frac{\gamma_{rad}}{\gamma_{non-rad}+\gamma_{rad}}\right)\right] \quad (1.16)$$

The chemical potential of an electron hole pair is restricted by the bandgap of the semiconductor and the Carnot limit (the need of the device to shed entropy to the surroundings).[3] Further reductions in potential result from solid angle mismatch in the received radiation (Ω_{Sun}) compared to the thermal radiation emitted (Ω_{emit}), incomplete light trapping within the cell, with the concentration factor ξ at most equal to $4n^2$,[51,52] and the relative rates of radiative (γ_{rad}) and non-radiative ($\gamma_{non-rad}$) recombination.[53] The maximum power voltage will be even lower than the open-circuit voltage due to internal resistances. So, when a photon of energy E is absorbed, only energy equal to $qV_{mp} < E_g \leq E$ is extracted.

The remaining fraction of the photon's energy ends up as heat. Part of the excess energy is released when excited electrons relax (thermalize) to the conduction band edge, and the rest is lost to the entropic effects described in eq. 1.16 and electrical resistance.[3] Additionally, since the IQE of the cell is imperfect, energy is lost when electrons and holes recombine. Energy loss to thermalization and recombination, and the inability to use sub-bandgap light, are intrinsic to photovoltaic energy conversion. These losses are plotted as fractions of the AM1.5G spectrum in **Figure 1.7**. The area highlighted in green represents the possible output power operating at 600 mV, assuming the entire AM1.5G spectrum is absorbed in the cell. Thermalization and entropic losses dominate the spectrum above the bandgap.

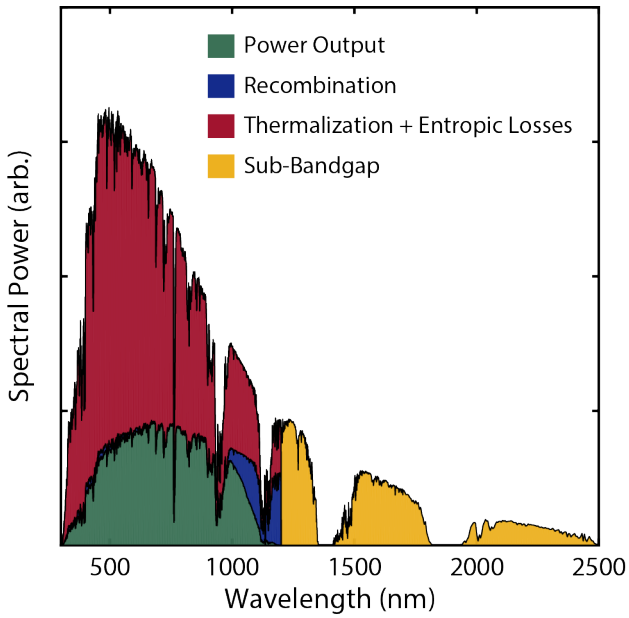

***Figure 1.7**: Spectral composition of output power and energy losses intrinsic to photovoltaic energy conversion, assuming a 600 mV operating voltage.*

Energy is also lost because of reflection form the module glass and cell, and parasitic absorption in the glass, encapsulant, or cell. Reflection losses are determined by the difference in refractive index between two materials. In the case of a photovoltaic module, some light reflects from the glass without transmitting to the interior. The reflection and transmission coefficients are defined by the Fresnel equations for *s*- and *p*-polarized light.[54]

$$R_s = |r_s|^2 = \left|\frac{n_1 \cos(\theta_i) - n_2 \cos(\theta_t)}{n_1 \cos(\theta_i) + n_2 \cos(\theta_t)}\right|^2 \tag{1.17}$$

$$R_p = |r_p|^2 = \left|\frac{n_1 \cos(\theta_t) - n_2 \cos(\theta_i)}{n_1 \cos(\theta_t) + n_2 \cos(\theta_i)}\right|^2 \tag{1.18}$$

$$T_s = \frac{n_2 \cos(\theta_t)}{n_1 \cos(\theta_i)} |t_s|^2 = \left|\frac{2n_1 \cos(\theta_i)}{n_1 \cos(\theta_i) + n_2 \cos(\theta_t)}\right|^2 \tag{1.19}$$

$$T_p = \frac{n_2 \cos(\theta_t)}{n_1 \cos(\theta_i)} |t_p|^2 = \left|\frac{2n_1 \cos(\theta_i)}{n_1 \cos(\theta_t) + n_2 \cos(\theta_i)}\right|^2 \tag{1.20}$$

The angles θ_i and θ_t are made by the incident and transmitted light, respectively, with the normal to the interface. The coefficients R and T describe the fractions of reflected and transmitted power relative to incident power, while r and t describe the relative electric field amplitudes of the reflected and transmitted waves, and are in general complex.

For glass, the reflection loss from the module is ~4% at all wavelengths at normal incidence. A thin-film anti-reflection coating reduces reflection from the glass, and can be

understood by considering the coherent sum of waves reflected from and transmitted through each material at the interface.[55] A similar coating reduces reflection from the cell at all but some blue wavelengths. Application of additional thin-film layers can further modify the reflection spectrum from a given interface.

Even when light does transmit into the module, not all of it will be absorbed into the bulk Si of the cell. Any light absorbed elsewhere, or any absorption that does not promote an electron across the bandgap is defined as parasitic absorption. The energy in the absorbed photon is immediately lost to heat. Typically, the glass and encapsulant will parasitically absorb UV light before it reaches the cell, but otherwise do not contribute to parasitic absorption above the bandgap. Near the bandgap, however, the cell is not thick enough for c-Si to absorb it fully in a single pass, even at an oblique angle. Most of this light reflects from the cell rear contact, however some is absorbed in the Al/Si or Al in the back surface field. Even with energy above the bandgap, photons absorbed here are wasted. Rear dielectric passivation, as in a PERC cell, reduces the area of Al/Si exposed to incident light, lessens the impact of this parasitic absorption, and improves the quantum efficiency as these photons can instead be absorbed in the bulk. Sub-bandgap light can only be absorbed parasitically, and can be absorbed in either the glass, encapsulant, or cell depending on the wavelength.[49] However, at some wavelengths, neither the glass, encapsulant, nor cell absorb light strongly. Although most light which enters the module is absorbed, it is possible for sub-bandgap light to enter the module and escape. As will be seen in later chapters, module reflection is much higher in the sub-bandgap spectral range compared to the visible.[56]

1.4. Photovoltaic Thermal Management

Lowering the operating temperature of a photovoltaic module would improve its conversion efficiency and output power. As previously shown, a decrease in temperature would primarily increase the operating voltage, as the various entropic losses in eq. 1.16 scale with $k_B T$. Thermal management for photovoltaics is a widely studied area,[57–59] and several different strategies have been developed. These strategies can be categorized as active cooling, where energy is expended to reduce the module temperature,[60] or passive cooling which requires no additional energy input.[61] The photonic mirrors which will be

developed and discussed in this thesis provide passive cooling. While many cooling methods are designed for concentrator photovoltaics (CPV),[58] here the photonic mirrors cool modules that are not receiving concentrated sunlight. The photonic mirrors function by selectively reflecting sub-bandgap light, preventing parasitic absorption and decreasing the amount of waste heat produced by the module. This is in contrast to other cooling methods, which seek to increase the rate at which the module transfers its heat to the surroundings.

1.4.1 Strategies for Module Temperature Reduction

To achieve thermal equilibrium, the module temperature increases until it can shed as much waste heat as it produces, which typically requires temperatures 20 – 30K above the ambient temperature, depending on weather conditions.[62,63] Many existing methods of module cooling, both active and passive, rely on increasing heat transfer from the module. These include cooling via forced convection,[64,65] phase change materials,[66,67] water immersion,[68] heat pipes,[69] and enhanced radiative heat transfer.[70,71] In general, active cooling methods can achieve larger temperature reductions than passive ones, but have the disadvantage of requiring external power to operate. Therefore, net energy gain is only possible if the absolute increase in module energy yield is greater than the energy needed to cool the module, or if the excess heat is used in a combined photovoltaic-thermal (PV-T) process.[72] Passive cooling methods do not rely on an external source, so any cooling they provide is a net gain to output power. However, some methods, such as heat pipes or fins, are less effective when ambient wind speed is low or if the wind is not blowing along a preferred direction. Other methods, such as water immersion, suffer from a trade-off between the cooling provided and the incident intensity blocked by the water. Or, in the case of phase-change materials, toxic compounds are used.[57]

Some authors have proposed improving mid-infrared emissivity as a way to reduce operating temperature.[73,74] This approach is similar to the one described in this thesis of spectrally-selective sub-bandgap reflection in that the enhanced emissivity is the result of a photonic design. The wavelengths of interest for emissivity are ~10 μm, the wavelengths of thermal radiation emitted by objects near the operating temperature of a cell or module. These wavelengths overlap with the atmospheric transmittance window from 8-13 μm,

allowing heat exchange with the upper atmosphere. This technique can allow maintenance of an equilibrium temperature below ambient during daytime.[75,76] For photovoltaics, though, the requirement to absorb sunlight precludes cooling below ambient. Still, Zhu *et al*. predict passive cooling of a Si cell by ~18K using a silica microphotonic design.[73] However, a photovoltaic module is covered by glass, which already has high mid-infrared emissivity. **Figure 1.8** plots the emissivity of sodalime glass[77] and the atmospheric transmittance near the transmittance window. To effectively cool a module radiatively, a photonic structure must improve the emissivity. Given the already high glass emissivity of module cover glass, its improvement to enhance radiative heat transfer is not a goal of the photonic designs in this work.

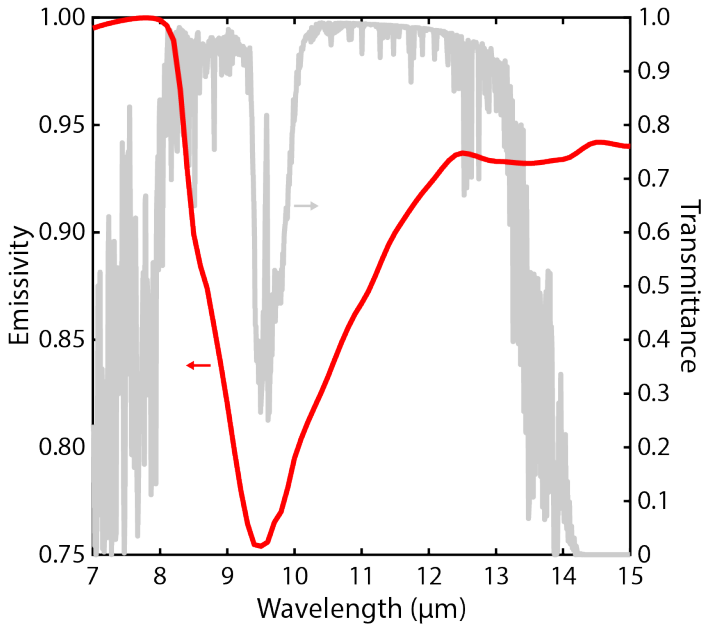

***Figure 1.8**: Hemispherical emissivity of sodalime glass (red, left axis) and transmittance of the atmosphere (gray, right axis) in the mid-infrared.*

1.4.2 Spectrally-Selective Reflection for Photovoltaic Thermal Management

Reflection of sub-bandgap light from a photovoltaic module is distinct from previously discussed thermal management strategies in that it reduces the total waste heat produced by the module, instead of increasing the heat transfer rate. For c-Si, ~19% of the incident solar spectrum is below the bandgap, most of which is parasitically absorbed in the module and could be prevented. Spectrally-selective reflection passively cools the module, without requiring an alternative cell or module design, and does not rely on

favorable wind or weather conditions to function. Literature reports of spectrally-selective cooling for photovoltaics typically focus on radiative cooling,[78] however some recent reports highlight the importance of sub-bandgap reflection as well.[8,9] Li *et al*.[8] show theoretical calculations of a module with a 45-layer coating on the glass which combines sub-bandgap reflection with mid-infrared emissivity to achieve 5-6K temperature reduction under 1000 Wm^{-2} AM1.5G radiation. Crucially, the coating improves transmission into the module over the useful portion of the spectrum, compared to the uncoated module. An *et al*.[9] design a combined photonic grating and 1-D coating to reflect sub-bandgap light and enhance radiative heat transfer from a thin-film Si solar cell, and demonstrate an opto-electro-thermal framework to model its effect. They calculate the performance of their photonic structure over a range of angles of incidence, and model the cooling and power conversion efficiency over the course of one day.

While spectrally-selective reflection has been shown to be effective for c-Si photovoltaic modules, the best method to design photonic structures achieving this reflection is unclear. The requirements on the structure are strict across the full solar spectrum. In addition to reflecting sub-bandgap light, the structure must not reflect light otherwise, or else it will block that light from reaching the cell and being converted. Furthermore, operating outdoors the structure receives direct and diffuse light from all possible incident angles. Proper spectral-selectivity must be maintained across all angles of incidence or else the structure will reduce power output during some times of the day or year. Periodic thin-film structures, known as Bragg stacks, possess high reflection over a tunable spectral range, but do not have simultaneously low reflection at other wavelengths, with a blue-shift in the reflection band at oblique incidence.[79] Aperiodic thin-film stacks are required to reduce reflection outside of the main band and mitigate the blue-shift of reflection at high angles. The works of Li *et al*.[8] and An *et al*.[9] include aperiodic thin-film photonic structures, but the method used to arrive at those designs is unclear.

Related to the design of spectrally-selective photonic mirrors is the modeling of their performance in a module installed outdoors. Realistic weather and irradiance conditions are often very different than the standard test conditions under which a module is rated. A module experiences a time-varying amount of direct and diffuse radiation over a broad range of angles of incidence, with illumination levels varying over the course of the day

and year, depending on the geographic location of the module. The cooling ability of a given photonic mirror design can be evaluated at standard test conditions, but it would be unrelated to longer-term average cooling, and the associated increase in cell efficiency and output power. Consideration of the optical modifications to the module made by a photonic mirror and its impact under realistic outdoor conditions is required.

Importantly, the primary goal of any thermal management technique is to increase the output power of a module. As this thesis will attempt to demonstrate, spectrally-selective photonic mirrors should be designed and evaluated according to this metric. Doing so will elucidate the most important characteristics of a photonic mirror in terms of its reflectivity and the relative importance of the sub-bandgap and above bandgap spectra, and will provide the greatest increase in energy yield under outdoor operation.

1.5. Thesis Summary

This thesis discusses the design, modeling, and characteristics of photonic structures used for thermal management in photovoltaic modules. Chapter 2 will introduce the modeling methods used to characterize modules with integrated photonic structures, and the optimization methods used to generate their designs. Chapter 3 will discuss properties of optimized photonic mirrors for the module glass, showing that consideration of mirror reflection at all angles of incidence is required for effective design. Chapter 4 will demonstrate the agreement between the simplified model used for optimization of photonic mirror design and combined multi-physics model used to gauge its effectiveness in increasing module energy yield. Chapter 5 will discuss photonic mirrors with relatively simple designs, intended to limit potential fabrication costs while increasing energy yield by enough to reduce the cost of energy. Chapter 6 will discuss the fabrication of two of these simple mirrors and their integration into photovoltaic modules. Then, results of an outdoor test to experimentally measure differences in power output and operating temperature relative to baseline modules will be presented. Chapter 7 discusses the efficacy of sub-bandgap reflection applied at interfaces interior to the module, such as at the cell surface or at the cell rear contact, as well as the temperature reductions possible for modules with PERC and Al BSF cells. Finally, Chapter 8 discusses the feasibility of using photonic

structures to scatter sub-bandgap light out of the module, and presents calculations necessary to characterize them.

Chapter 2 - Modeling and Optimization Methods

2.1. Introduction

Photovoltaic modules experience a wide variety of irradiance and ambient weather conditions over the course of the day and the year, which much of the time are not similar to the standard test conditions at which a module is characterized. Modules installed at fixed tilt outdoors, for example, receive varying amounts of direct and diffuse sunlight from all angles of incidence, and operate at temperatures that are determined both by ambient conditions and the amount of waste heat produced.[80] Evaluating and designing optical structures to maximize energy yield for modules therefore also requires methods for characterizing and predicting the resulting increase in efficiency and energy production under realistic conditions.

Many simple models exist to calculate the power or operating temperature of a photovoltaic module,[81–85] including those that model outdoor performance.[86–89] For example, Sun *et al.*,[70] Li *et al.*,[8] and Vaillon *et al.*[90] model the module temperature reduction from a given sub-bandgap reflective and mid-IR emissive coating on the module glass using a 1-D heat transfer equation[8] or a heat balance on the entire module[70,90]. The models used in this thesis inform the design of photonic structures, and are therefore tailored to accurately characterize the impact those structures have on module energy yield. Crucially, these models account for the weather and irradiance conditions typical for outdoor photovoltaic installations. These conditions include ambient temperature and irradiance, but also the expected angle of incidence of that irradiance on the module, which has a large impact on its interaction with the photonic structures. The inclusion of realistic weather data and its angular dependence allows common assumptions of normal incidence or of a fixed irradiance level to be avoided. Therefore, the full spectral and angular properties of the photonic structure are considered, and the relative importance of the reflective and anti-reflective aspects of its design are understood in terms of their impact on module energy yield.

Two models are presented, a combined opto-electro-thermal multi-physics model, and a time-independent matrix model. The multi-physics model combines optical ray-

tracing with finite-element simulation to predict outdoor performance of a photovoltaic module, including those modified by photonic structures, over the course of an entire year. The time-independent matrix model is a computationally much faster method to evaluate photonic structures within photovoltaic modules. The time-independent model is distilled to only return the improvement in energy yield offered by a photonic structure. Realistic irradiance levels and the expected angle of incidence on the module are included, but other weather effects such as ambient temperature are omitted from the time-independent model. Optimization of the energy yield improvement gives candidate designs for the photonic structures.

2.2. Thermal and Electrical Finite-Element Simulations

Outdoor simulation of photovoltaic modules based on real weather and irradiance data is a key component of the modeling done in this work. The full simulation is a combination of finite-element simultaneous thermal and electrical simulation (COMSOL Multiphysics ®),[91] with angle-resolved optical inputs determined by module optical ray-tracing (see Section 2.2.2). This model, named TOMCAT, was created primarily by collaborators to this work, and more information can be found in Silverman *et al*.[92] What follows is a brief description of the finite-element model properties, discussion of the required inputs, and the method of analysis of the model outputs.

2.2.1 TOMCAT

TOMCAT models the output power and operating temperature of a photovoltaic module installed outdoors facing south at fixed tilt. Radiative, conductive, and convective heat transfer are all included. To calculate temperatures and heat transfer rates, several inputs must be known, including ambient temperature, wind speed, irradiance incident in the plane-of-array (POAI), solar altitude, ground and sky temperature, thermal conductivities of all materials present in the simulation region, and the thermal emissivity of the external module materials. Tables of thermal conductivities and emissivities, the (2-D) simulation geometry, details of the view factor model used for radiative heat transfer,

and details of the (2-D) convective heat transfer model are found in Silverman *et al.*[92] Module electrical efficiency is also required; its calculation is discussed in Section 7.2.2.

2.2.2 Preparing TOMCAT Weather and Irradiance Inputs

Inputs pertaining to irradiance and weather conditions must be given by the user, and in this work are taken from the Typical Meteorological Year (TMY3) data set.[19] This data set compiles month-by-month historical weather data into a 'typical' year for locations across the United States. A description of the relevant data found in TMY3 data sets is given in **Table 2.1**. In addition, the corresponding latitude, longitude, and altitude are listed, and data are given at hourly intervals, both day and night.

Table 2.1: Description of Data Taken from TMY3 Data Sets

Parameter	Abbreviation	Description	Use
Direct Normal Irradiance	DNI	Terrestrial irradiance (Wm^{-2}) through a plane whose normal points at the Sun	Direct POAI
Diffuse Horizontal Irradiance	DHI	Terrestrial irradiance (Wm^{-2}) through a plane parallel to the ground, excluding radiation directly from the Sun.	Diffuse POAI
Global Horizontal Irradiance	GHI	Terrestrial irradiance (Wm^{-2}) through a plane parallel to the ground.	Clearness Index, Ground Temp.
Extraterrestrial Irradiance	ETR	Irradiance (Wm^{-2}) at the top of the Earth's atmosphere through a plane parallel to the ground	Clearness Index
Dry-bulb Temperature	$T_{Dry\text{-}bulb}$	Taken to be equal to the ambient temperature (°C)	Ambient, Sky, and Ground Temp. and Apparent Sun Elevation
Dew Point	T_{Dew}	Temperature below which atmospheric water begins to condense (°C)	Sky Temp.
Pressure	P	Atmospheric pressure (mbar)	Apparent Sun Elevation
Wind Speed	-	Given directly as input to TOMCAT (m/s), direction is ignored	-

Only wind speed and dry-bulb temperature are given to TOMCAT directly as inputs. Other inputs require additional calculation. The plane-of-array irradiance is the sum of the direct irradiance (arriving from the apparent direction of the Sun) and the diffuse irradiance (scattered anywhere in the atmosphere towards the module). It is assumed that ground reflected irradiance equal to 10% of the POAI is incident on the rear of the module. The direct irradiance in the plane-of-array is given by eq. 2.1, where θ_{Sun} is the angle between the module normal and the direction of the Sun. This angle depends on the position of the Sun in the sky, calculated by the NREL Solar Position Algorithm,[93] using the latitude, longitude, altitude, UTC time, and calendar year. The solar elevation (zenith angle) is corrected for atmospheric refraction using the ambient temperature and pressure; the calendar year is always 2017. The diffuse irradiance in the plane-of-array is given by the isotropic sky model,[94] which assumes equal intensity from all directions, shown in eq. 2.2. The diffuse irradiance only depends on the module tilt angle, θ_{Tilt}, and the diffuse horizontal irradiance.

$$POAI_{Direct}(t) = DNI(t) \cdot cos(\theta_{Sun}(t)) \tag{2.1}$$

$$POAI_{Diffuse}(t) = DHI(t) \frac{1+cos(\theta_{Tilt})}{2} \tag{2.2}$$

$$POAI(t) = POAI_{Direct}(t) + POAI_{Diffuse}(t) \tag{2.3}$$

In TOMCAT, the module can exchange heat with the sky and ground radiatively, at a rate which depends on their (absolute) temperatures. The ground temperature is correlated with global horizontal irradiance and dry-bulb temperature, and the sky temperature is correlated with the dew point, dry-bulb temperature, and clearness index (K). These correlations are required to run TOMCAT with TMY3 data sets, as listings of sky and ground temperature are absent. These correlations were developed for this purpose by using data from the NREL Solar Radiation Research Laboratory Baseline Measurement System (SRRL BMS).[18] Additional details are provided in the Appendix.

$$T_{Ground} = T_{Dry-bulb} - 1.362 + 0.01287 \cdot GHI + 273.15 \tag{2.4}$$

$$K = \frac{GHI}{ETR} \tag{2.5}$$

$$T_{Sky} = 76.56 + 10.59\, ln\left(\frac{P_w}{Pa}\right) - 4.557K + 0.4437 \cdot (T_{Dry-bulb} + 273.15) \tag{2.6}$$

In eq. 2.6, the water vapor pressure, P_w, is calculated in Pascal using the Tetens equation.[95,96]

2.2.3 Analysis of TOMCAT Results

TOMCAT simulations return time series module output power, $W(t)$, and cell temperature, $T(t)$, with one data point for every timestamp in the input data. If the input data is from TMY3 data sets, then there is one data point for each hour of the year. Analysis requires comparison of two simulations using the same TMY3 input data, where one simulation corresponds to the baseline module, and whose results are denoted by the 'Baseline' subscript. Temperature difference ΔT and power difference ΔW between the test module and the baseline are defined in eqs. 2.7 and 2.8, respectively.

$$\Delta T(t) = T(t) - T_{Baseline}(t) \tag{2.7}$$

$$\Delta W(t) = W(t) - W_{Baseline}(t) \tag{2.8}$$

The power increase due to temperature reduction ΔW_T (instantaneous thermal benefit) is calculated from the baseline power, temperature difference, and temperature coefficient of module efficiency, β, as shown in eq. 2.9. In this work, $\beta = -0.39\ \%/K$. The power due to increased current ΔW_O (instantaneous optical benefit) at any time is the difference between the total benefit at that time and the thermal benefit, given by eq. 2.10.

$$\Delta W_T(t) = \Delta T(t) \cdot \beta \cdot W_{Baseline}(t) \tag{2.9}$$

$$\Delta W_O(t) = \Delta W(t) - \Delta W_T(t) \tag{2.10}$$

Total simulated optical and thermal benefits are calculated as the sum over time of the individual benefits, normalized to the total power produced by the baseline module, shown in eqs. 2.11 and 2.12.

$$B_{Optical,Sim} = \frac{\sum_t \Delta W_O(t)}{\sum_t W_{Baseline}(t)} \cdot 100\% \tag{2.11}$$

$$B_{Thermal,Sim} = \frac{\sum_t \Delta W_T(t)}{\sum_t W_{Baseline}(t)} \cdot 100\% \tag{2.12}$$

Finally, the power-weighted average temperature difference, ΔT_{avg}, is the thermal benefit divided by the temperature coefficient of module efficiency, which is negated so that positive temperature differences represent module cooling.

$$\Delta T_{avg} = \frac{B_{Thermal,Sim}}{-\beta} \quad (2.13)$$

2.3. Module Ray Tracing

Module optical properties are modeled using the ray-tracing software SunSolve.[97] The software allows an entire module, including the top glass, encapsulant, cell, and backsheet, to be included in the ray-tracing domain. Incident light can span the range from 300-2500 nm, can be incident on either the front or rear side of the domain, and can be incident at any angle with respect to the ray-tracing domain, or with an isotropic angular distribution representing diffuse light. The wavelength-dependent complex refractive index of each material is known during ray-tracing, however adherence to the Kramers-Kronig relationship[98] is *not* enforced. If multiple material layers are present during ray-tracing, e.g. an entire module, the software will report absorption in each layer separately. Additionally, reflection from the top layer in the domain is reported, as well as the total fraction of light at each wavelength which exited the domain from the top surface, and similarly for the rear surface.

In modern commercial c-Si photovoltaic cells, the top surface is textured to admit and trap more light. The ray-tracing software can account for this texturing, and in this work the top surface of all cells has randomly arranged upright square pyramidal texture. Random arrangement allows adjacent pyramids to be displaced both vertically and horizontally with respect to each other. Furthermore, all interfaces between two material layers can support thin-films of tertiary materials, such as an antireflection coating on the glass or cell surface, or the thin-film mirrors which are a main subject of this work. The reflection, absorption, and transmission of these interfaces cannot be determined in the ray-optics limit. The ray-tracing software implements transfer-matrix calculations when a ray is incident on an interface with thin films to determine probabilities of reflection, absorption, or transmission. Absorption at interfaces is reported separately, alongside absorption in all other material layers.

In the domain of the ray-tracing software, all interfaces are perfectly flat, which would imply specular reflection or refraction in every instance. However, in a real device, especially at the front and rear surfaces of the cell, interfaces can be rough on a length scale comparable to the wavelength of light. To account for this roughness, the ray-tracing

software can optionally include scattering at an interface. The scattered light can either have a Lambertian distribution,[99] where intensity is equal in all directions, or a distribution following the Phong model,[100] where intensity is concentrated near the specular direction.

2.3.1 Ray Tracing for TOMCAT

Module optical properties are determined by ray-tracing as part of all TOMCAT simulations. Full details are provided in Silverman *et al*.[92] Briefly, ray-tracing results are obtained over wavelengths 300-2500 nm at 5 nm intervals, and incident angles 0 - 88° at 11° intervals. Each new module geometry, or each new thin-film mirror simulated, requires separate ray-tracing. Use of new TMY3 input data for the same module, however, does not require re-doing the ray-tracing. The incident spectrum is the AM1.5G solar spectrum, so that the solar power absorbed by the various layers within the module can be directly calculated. Therefore, all incident light, both direct and diffuse, is assumed to have spectral power proportional to the AM1.5G spectrum. The AM1.5G spectrum is intended to represent global irradiance, i.e. including both direct and diffuse components.[13,15] While the direct and diffuse spectra separately are different, taken together the AM1.5G spectrum is typical.

2.3.2 The Optical Model of c-Si Photovoltaic Modules

Two baseline module designs, one including an Al-BSF cell, and one including a PERC cell, are considered in this work. Schematics of both modules are shown in **Figures 2.1a-b**. Both cells were modeled as encapsulated behind 3.2 mm low-Fe (0.05 wt%) glass[101] and 0.4 mm of UV-absorbing EVA.[102] The cell front surface includes pyramidal texture with a slope angle of 50.1°, matching the peak slope measured via scanning probe microscopy (SPM), and with a front SiN_x ARC with 55 nm thickness, chosen as the best match to cell reflection over the visible spectrum. Additionally, Phong model scattering was applied to the front cell surface, which is intended to account for variation in pyramid slope angle and improve modeling of infrared light trapping in the cell.[44] The parameters within the Phong model were adjusted such that 95% of scattering occurs within 6° of the specular direction, roughly matching the distribution of pyramid slope angles measured by SPM. Details of the SPM measurement are given in the Appendix. The Al-BSF cell back

contact was Al, with a 30 nm thin film of Al/Si eutectic at the interface, with optical properties taken from Subedi *et al*.[56] The thickness of the Al/Si eutectic was varied to match experimental module reflection results. A comparison of modeled and experimental module reflection is given later in **Figure 7.1**. Upon reflection from the cell back contact, light was always scattered with a Lambertian distribution, to model roughness at the back interface.

The only optical difference between the PERC cell and the Al BSF cell is the back contact. At the back contact of the PERC cell, two regions are modeled: the local BSF (contact region) and the region between contacts. The local BSF includes a 1000 nm thick film of Al/Si eutectic.[56] Between contacts, there is a 10 nm film of Al_2O_3 and a 100 nm film of SiN_x. Both regions are set to scatter all light with a Lambertian distribution. A line pattern was used for the back contacts, with a contact width equal to half of the 2.5 mm pitch between lines. While the actual electrical contacts in PERC cells are thin with respect to the pitch, diffusion during firing of Al into Si extends beyond the narrow contact. This is visually apparent on the back of a PERC cell as it appears darker in a macroscopically-wide region around the contacts.[103] While in reality the diffusion of Al into Si extends into regions passivated by dielectrics, for purposes of optical modeling the contact area is extended to reproduce the amount of sub-bandgap absorption seen experimentally.

Both the Al-BSF and PERC cells are 180 μm thick. The optical properties are taken from Schinke *et al*.[40] and Herzinger *et al*.[104] with the index modified from 1100 nm – 2500 nm to account for free carrier absorption (FCA). Free carrier absorption was estimated using the FCA absorption model of Baker-Finch *et al*.[105,106] The doping profile assumed a background p-type doping at 10^{16} cm^{-3} and an n-type profile with a peak of 10^{20} cm^{-3} at the surface, decaying with a complementary error function profile with a characteristic length of 300 nm. In reality, the amount of FCA in Si will depend on position due to the non-uniform doping profile. However, for simplicity the Si index is kept uniform in space.

Finally, it is important to note that the optical model described above has evolved over the course of this work. Some results discussed are based on ray-tracing results of slightly different module geometries. Key differences are noted when presenting those results.

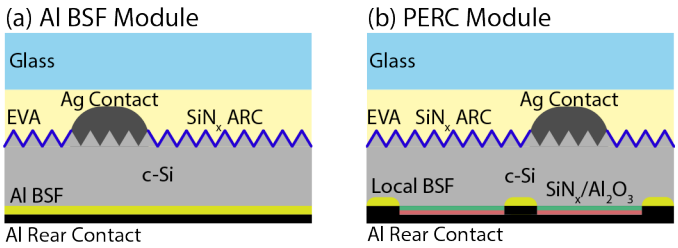

***Figure 2.1**: Schematic of (a) Al BSF module and (b) PERC module used in the ray tracing software. The Al BSF module contains a full area rear back surface field (BSF), while the PERC module contains local BSFs. The remaining rear area is passivated by SiN_x and Al_2O_3.*

2.4. The Time-Independent Matrix Model

The time-independent matrix model, described in this section, accounts for outdoor irradiance conditions and predicts the benefit from selective reflectors on the overall energy yield of a photovoltaic module. The model presented is unique as it combines the module wavelength- and angle-dependent optical response with real weather and irradiance data to calculate the benefit of a given spectrally selective mirror compared to a baseline case. It is especially important when considering spectrally selective coatings to include the current increase provided by antireflection and the influence that increased current has on operating temperature.

Figure 2.2 shows a schematic of the energy loss pathways considered in this model, along with the general module layout considered. Ideally, the current-generating layers inside the photovoltaic module will absorb all light with energy greater than the bandgap into the cell, and none of the sunlight with energy less than the bandgap. However, materials commonly used to construct photovoltaic modules such as low-iron glass and EVA absorb some sunlight above and below the Si bandgap, and especially in the near-UV spectral range, before it reaches the cell.[107,108] Fresnel reflection at every material interface also limits the amount of light that enters the cell, and varies as a function of wavelength and angle of incidence. Finally, ~80% of the energy entering the cell is still not converted to electricity, but is instead wasted as heat. Thermalization of carriers to the bandgap, carrier recombination, resistive losses, sub-bandgap absorption at the metallic cell back contact, and absorption outside of the cell in the encapsulant and cover glass all contribute

to heating the module. Each energetic pathway must be individually characterized, as all are affected by an optical modification such as addition of a 1-D spectrally-selective filter.

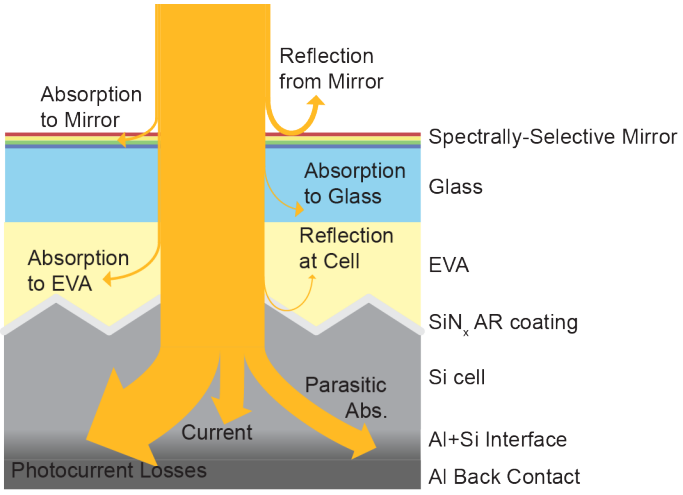

***Figure 2.2**: Schematic showing the heat losses considered in the model. Light is absorbed into the glass and encapsulant above the cell, or can be reflected at the air/glass interface or by the cell AR coating. Only a fraction of incident light is absorbed into the cell.*

In addition to detailed consideration of optical and electrical loss pathways, the time-independent matrix model also accounts for the real irradiance conditions experienced by the module. Operating outdoors, a photovoltaic module receives a time-dependent amount of radiation both directly from the sun and also as scattered diffuse radiation.[109] Sunlight arrives at all angles of incidence, thus making modules which can effectively collect radiation over a wide range of angles beneficial. To avoid simulations which require stepping through time-series irradiance data, module energy yield and change in operating temperature are calculated from the total amount of energy received as a function of incidence angle. The actual module operating temperature is additionally a function of ambient temperature and wind speed,[110] with correlations linking these variables.[111] This model, however, focuses on differences in module operating temperature arising from changes to module optical properties, and is designed to require minimal computing time. Therefore, the model does not attempt to calculate an actual absolute operating temperature and does not require ambient temperature data or wind speed data.

2.4.1 Model Preparation

In advance of model calculations, matrices corresponding to fractions of incident light absorbed in or reflected at each module layer must be known as a function of wavelength and incident angle. Furthermore, the relative incident solar power at each angle with respect to the module, termed the angle-weighting, is required. These matrices and the angle-weighting allow calculation of power absorbed throughout the module while accounting for realistic outdoor irradiance conditions. While the amount of light reaching a particular interface may change with the addition of a spectrally-selective mirror, these matrices do not change since the fraction is referenced to the light incident on that particular layer. To model spectrally-selective mirrors on glass, matrices for absorption in the glass, encapsulant, and cell are required, as well as for reflection at the cell surface. For the glass and encapsulant layers, a matrix of absorbance fractions A can be calculated via Beer's Law, shown below in eq. 2.14.

$$A(\lambda,\theta) = exp\left(-\frac{4\pi k(\lambda)d(\theta)}{\lambda}\right) \tag{2.14}$$

In the above equation, the absorbance is calculated as a function of the wavelength, λ, and free space angle of incidence, θ, where k is the wavelength-dependent imaginary index of refraction and d is the angle-dependent optical path length in the material. Real and imaginary indices n and k for glass and encapsulant are taken from the PV Lighthouse database[107] and Vogt et al.,[108] respectively. The geometric path length in the material, given by eq. 2.15, is calculated from the known thickness t, and angle θ_{Ref} at which the refracted beam travels through the material, given in eq. 2.16.

$$d = \frac{t}{cos(\theta_{Ref})} \tag{2.15}$$

$$\theta_{Ref} = sin^{-1}\left(\frac{sin(\theta)n_{Air}}{n(\lambda)}\right) \tag{2.16}$$

The thicknesses of glass and encapsulant are 3.2 mm and 0.4 mm, respectively. The angle of refraction is calculated using n_{Air} since the angle of incidence is the angle that the light, traveling in air, makes with the module normal. We take $n_{Air} = 1$ for all calculations. The refractive index of the glass and encapsulant are very similar, so there is little refraction at this interface. Furthermore, reflection at this interface is ignored as it is <0.2% for all

possible incidence angles and all wavelengths between 320 nm and 2500 nm. The glass[107] and encapsulant[108] indices are less closely matched in the spectral range <320 nm, however this light is completely absorbed by the glass or encapsulant before reaching the cell. Therefore, ignoring the 3-5% reflection at wavelengths <320 nm does not affect model results.

After traveling through the glass and encapsulant, light reaches the 75 nm SiN_x antireflection coating between the textured cell surface and the encapsulant. A matrix of reflection from the SiN_x ARC versus wavelength and angle of incidence (in air relative to the module normal) is estimated using transfer matrix calculations.[112] The calculations assume that the coating is conformally deposited onto C4-symmetric pyramidal surface texture with an angle of inclination of 54.74°. Total reflection is an average of reflection off of the four faces of the pyramid for a given angle of incidence (in air relative to a planar surface), and reflection is averaged over azimuth angle. This reflection matrix has the same dimensions as all absorption matrices. Details of this calculation and a comparison to ray-tracing results are given in the Appendix. Accounting for reflection from the cell SiN_x ARC is important for the model, however the reflection from the SiN_x ARC is small across the spectrum. The differences between the results of a first approximation described in the Appendix, or the results of ray-tracing calculations have a negligible effect on the improvement offered by a spectrally-selective mirror, the main model result. As discussed later in Chapter 7, much higher reflection from the cell surface is required in order for the modeling of that interface to make a significant impact on module operating temperature.

The absorption matrix for the cell cannot be obtained via Beer's Law, as the pyramidal cell surface texture necessitates the use of ray tracing software to calculate these matrices, which is the approach we implimented.[97] For each interface or module layer considered within the cell, the matrix value corresponds to the ratio of sunlight of a certain wavelength incident at a certain angle either reflected at that interface or absorbed by that module layer to the sunlight incident at that interface or at the top of that layer. Although a mirror may change the total light incident at some interfaces or module layers, these ratios stay constant. Therefore, the ray-tracing software only needs to be run for the baseline cell case to obtain its absorption, and does not need to be run for every new design. The Si cell is 150 μm thick with aperiodic pyramidal surface texture with an angle of inclination of

54.74°, and the refractive index is taken from Schinke *et al.*[113] and Herzinger *et al.*[114] The cell back interface is modelled as 103 nm of an Al-Si alloy, with the refractive index taken from Subedi *et al.*,[56] with a 0.02 mm thick Al back contact.[115] In the calculation of the cell absorption matrix, light is injected in the encapsulant material directly above the cell. Fractional absorption is calculated as the ratio of the reported absorption in the cell to the amount that entered the cell (total less reflection at the cell SiN_x ARC). Snell's Law is used to back calculate the angle of incidence in air. When this model is applied, absorption and reflection matrices for all materials and interfaces considered are calculated at wavelengths spaced 5 nm apart in the range 300 – 2500 nm and at angles spaced 1° apart between 0° and 89°.

Finally, the model requires an angle weighting of expected solar irradiance versus angle of incidence to determine mirror energy benefit. These angle weightings are determined using Direct Normal Irradiance (DNI) and Diffuse Horizontal Irradiance (DHI) from Typical Meteorological Year data[19] at various locations across the United States. Therefore, model results correspond to the estimated energy benefit of a module with a given mirror installed at a given tilt angle at the location where irradiance data was taken. All modules are assumed to face south. The angle weighting is calculated separately for the direct and diffuse components of the irradiance, and combined and normalized at the end. The direct component of irradiance, E_{Direct}, a time t is shown in eq. 2.17, which depends on the angle θ_{AOI} that direct light makes with the module surface normal, given in eq. 2.18.

$$E_{Direct}(t) = DNI(t) \cdot cos(\theta_{AOI}(t)) \tag{2.17}$$

$$cos(\theta_{AOI}(t)) = cos(\theta_z(t))\, cos(\theta_t) + sin(\theta_z(t))\, sin(\theta_t))\, cos(\theta_a - \theta_{am}) \tag{2.18}$$

In eq. 2.18, θ_z and θ_a are the solar zenith and azimuth angles, respectively, and are determined using the NREL Solar Position Algorithm.[3] The angle θ_t is the module tilt and θ_{am} is the module azimuth, which is always 180° (south-facing). The time series direct irradiance data is transformed into the direct component of the angle weighting eq. 2.19, where δ is the Kronecker delta function, θ ranges from 0 to 89 degrees, and θ_{AOI} is measured in degrees.

$$C_{Direct}(\theta) = \sum_t E_{Direct}(t)\delta(floor(\theta_{AOI}(t), \theta) \quad (2.19)$$

The diffuse component of the irradiance is given by the isotropic sky model,[94] shown in eq. 2.20.

$$E_{Diffuse}(t) = \frac{1+cos(\theta_t)}{2} \cdot DHI(t) \quad (2.20)$$

The diffuse component of the angle weighting is given in eq. 2.21, where θ is measured in degrees and the factor of $180/\pi$ is for normalization.

$$C_{Diffuse}(\theta) = \frac{sin(\theta)\,cos(\theta)}{180/\pi} \cdot \sum_t E_{Diffuse}(t) \quad (2.21)$$

The final angle weighting is the sum of direct and diffuse components, and is normalized such that its components sum to unity.

$$C(\theta) = \frac{C_{Direct}(\theta) + C_{Diffuse}(\theta)}{\sum_\varphi C_{Direct}(\varphi) + C_{Diffuse}(\varphi)} \quad (2.22)$$

One additional note is that the time-independent matrix model does not account for coherent optical effects such as multiple reflection between module layers. Therefore, in devices where coherent multiple reflections are important, such as in thin-film solar cells, the model would have to be amended to include these effects. Given the mm-scale thicknesses of the module layers, however, it is assumed here that only incoherent effects are present.

2.4.2 Model Calculation

Given a thin-film mirror at the air/glass interface in a c-Si solar module, the model estimates the increase in annual energy yield compared to a module without the thin-film mirror. The energy benefit, $B_{Total,Model}$, is calculated in two parts: the optical benefit due to increased current production, and the thermal benefit due to increased module efficiency at lower operating temperature.

$$B_{Total,Model} = B_{Optical,Model} + B_{Thermal,Model} \quad (2.23)$$

All calculations for the time-independent matrix model are performed on angle-weighted matrices based on the fraction of incident energy incident at each angle over the

course of a year at the location of interest; the spectrally-selective mirror reflection matrix and transmission matrix, as well as all absorption matrices (A_{Glass}, $A_{Encapsulant}$, and A_{Cell}) and the SiN_x ARC reflection matrix, are weighted similarly to the example shown in eq. 2.24. The calculation is shown for R_{Mirror}, the spectrally-selective mirror reflection matrix. The dot product with the angle weighting $C(\theta)$ yields $R_{w,Mirror}$, the weighted, spectrally-selective mirror reflection matrix. Similar calculations yield the weighted mirror transmission matrix, $T_{w,Mirror}$, the weighted absorption matrices, $A_{w,Glass}$, $A_{w,Encapsulant}$, and $A_{w,Cell}$, and the weighted SiN_x ARC reflection matrix, $R_{w,SiNx}$.

$$R_{w,Mirror}(\lambda) = \sum_{\theta} R_{Mirror}(\lambda, \theta) \cdot C(\theta) \tag{2.24}$$

Optical benefit is determined from the estimated carrier flux, $N_{Carrier}$, shown in eq. 2.25 where $\varphi_{AM1.5G}$ is the spectral photon flux in the AM1.5G spectrum (m^{-2} s^{-1} nm^{-1}) and IQE is the wavelength-dependent internal quantum efficiency of the Si cell,[116] and remains the same in both baseline and mirrored modules. In the model, the glass and encapsulant are index-matched. This interface has <0.2% reflection, which is neglected in eq. 2.25 and subsequent equations modeling light passing through the glass/encapsulant interface. $N_{Carrier}$ is expressed here as a flux of charge carriers; multiplication of eq. 2.25 by the elementary charge gives units of current density.

$$N_{Carrier} = \int_{300}^{2500} \varphi_{AM1.5G}(\lambda) \cdot T_{w,Mirror}(\lambda) \cdot \left(1 - A_{w,Glass}(\lambda)\right) \cdot \left(1 - A_{w,Encapsulant}(\lambda)\right) \cdot \left(1 - R_{w,SiNx}(\lambda)\right) \cdot A_{w,Cell}(\lambda) \cdot IQE(\lambda) d\lambda \tag{2.25}$$

While the limits of integration are 300 nm to 2500 nm, no carriers are generated beyond ~1100 nm as the IQE is zero at those wavelengths.

The optical benefit is calculated using eqs. 2.26 and 2.27, where $N_{Carrier,Baseline}$ is the result of eq. 2.25 for a module with no thin-film mirror. Eq. 2.25 counts the number of carriers collected per unit area; eq. 2.26 gives the percentage increase in the number of carriers collected ($B_{Current}$). The increase in the number of carriers is, however, not equal to the increase in energy yield due to the collection of these additional carriers. Additional carriers are also collected at slightly different energy (operating voltage) due to a change in operating temperature compared to the baseline case. This is captured in the temperature

coefficient of maximum power, β, (see eq. 2.28), but also included in the optical benefit as shown in in eq. 2.27.

$$B_{Current} = \left(\frac{N_{Carrier}}{N_{Carrier,Baseline}} - 1\right) \cdot 100\% \tag{2.26}$$

$$B_{Optical,Model} = B_{Current} + \left(\frac{N_{Carrier}}{N_{Carrier,Baseline}} - 1\right) \cdot B_{Thermal,Model} \tag{2.27}$$

The percent thermal benefit is given in eq. 2.28 and depends on the difference between the total waste heat flux, Φ_{Total} generated in the module and that of the baseline module without the thin-film mirror, $\Phi_{Total,Baseline}$. The individual waste heat fluxes that comprise Φ_{Total} are given in eqs. 2.29-2.34. Dividing the thermal benefit in eq. 2.28 by β gives an estimate of the average temperature difference between the baseline and mirrored modules.

$$B_{Thermal,model} = \frac{\left(\Phi_{Total} - \Phi_{Total,Baseline}\right) \cdot F_{Irradiance}}{30 \frac{W}{K\,m^2}} \cdot \beta \tag{2.28}$$

The AM1.5G spectrum used in this work contains ~1000 W m^{-2} in the range 300 – 2500 nm. The irradiance correction factor $F_{Irradiance}$ accounts for the fact that, on average, the solar module will not receive 1000 W m^{-2} irradiance in the plane-of-array. For design of thin-film mirrors in this paper, $F_{Irradiance}$ is 0.590, the value for Denver, CO at a module tilt of 20 degrees. We arrive at this factor by determining the contraharmonic mean of the POAI from time-series irradiance data, and correlating this number to the simulated thermal benefit, as discussed in section 4.3.2. Evaluations of the time-independent matrix model at other locations use other values of $F_{Irradiance}$ as discussed in Section 4.3.2. Additionally, assumed in eq. 2.28 is a 30 W/K-m^2 conversion factor between waste heat removal and operating temperature decrease, based on analysis of outdoor testing of c-Si modules at NREL.[117] The temperature coefficient of maximum power relates temperature difference to efficiency improvement and is taken to be 0.39%/K throughout this work.

The total waste heat flux Φ_{Total} (W m^{-2}) produced in the module is given by eq. 2.29 as the sum of terms corresponding to heat flux absorbed to the thin-film mirror on the glass, the glass itself, and the encapsulant, in addition to heat fluxes accounting for the excess energy of photons whose absorption led to carrier collection and parasitic absorption of light that did not lead to carrier collection. Eq. 2.30 gives the heat generated to absorption

in the thin-film mirror, $P_{AM1.5G}$ is the spectral power in the AM1.5G spectrum (W m^{-2} nm^{-1}).

$$\Phi_{Total} = \Phi_{Mirror} + \Phi_{Glass} + \Phi_{Encapsulant} + \Phi_{Photocurrent} + \Phi_{Parasitic} \quad (2.29)$$

$$\Phi_{Mirror} = \int_{300}^{2500} P_{AM1.5G}(\lambda) \cdot \left(1 - R_{w,Mirror}(\lambda) - T_{w,Mirror}(\lambda)\right) d\lambda \quad (2.30)$$

Eqs. 2.31 and 2.32 give the heat flux generated by absorption by the glass and encapsulant, respectively.

$$\Phi_{Glass} = \int_{300}^{2500} P_{AM1.5G}(\lambda) \cdot T_{w,Mirror}(\lambda) \cdot A_{w,Glass}(\lambda) d\lambda \quad (2.31)$$

$$\Phi_{Encapsulant} = \int_{300}^{2500} P_{AM1.5G}(\lambda) \cdot T_{w,Mirror}(\lambda) \cdot (1 - A_{w,Glass}(\lambda)) \cdot A_{w,Encapsulant}(\lambda) d\lambda \quad (2.32)$$

The light that passes through the mirror, glass, encapsulant, and SiN_x ARC can be absorbed by the cell. An absorbed photon can produce a charge carrier which is eventually extracted at the assumed operating voltage V_{mp}. Therefore, all of the photon's energy above qV_{mp} is lost to heat from thermalization of the carrier to the conduction band edge, entropic losses associated with the cell temperature, spontaneous emission from the semiconductor, imperfect light trapping, and recombination at crystal defects, and resistive heating.[50] These losses are calculated in eq. 2.33, where the fraction of the spectral power at wavelength λ lost before carrier collection is $\left(1 - \lambda \frac{qV_{mp}}{hc}\right)$. There are no losses from photocurrent production at wavelengths with zero IQE.

$$\Phi_{Photocurrent} = \int_{300}^{2500} P_{AM1.5G}(\lambda) \cdot \left(1 - \lambda \frac{qV_{mp}}{hc}\right) \cdot T_{w,Mirror} \cdot \left(1 - A_{w,Glass}(\lambda)\right) \cdot \left(1 - A_{w,Encapsulant}(\lambda)\right) \cdot \left(1 - R_{w,SiNx}(\lambda)\right) \cdot A_{w,Cell}(\lambda) \cdot IQE(\lambda) d\lambda \quad (2.33)$$

In this work, V_{mp} is taken as 528 mV for the purposes of the Time-Independent Matrix Model.[118] The above equation is the only place where V_{mp} appears and, as these photocurrent losses are a major waste heat source, affects the model result significantly. The value of 528 mV was chosen initially to roughly match the module efficiency in finite element calculations (see Section 2.2). This parameter is certainly not fixed, however, and can vary to match characteristics of another cell.

If light is absorbed into the cell and there is no corresponding carrier extracted, then all of the energy associated with absorption is wasted as heat. The waste heat flux due to this parasitic heat absorption in the cell is given in eq. 2.34, and is primarily the sum of the energies of recombined carriers and of sub-bandgap photons absorbed at the metallic back contact.

$$\Phi_{Parasitic} = \int_{300}^{2500} P_{AM1.5G}(\lambda) \cdot T_{w,Mirror}(\lambda) \cdot \left(1 - A_{w,Glass}(\lambda)\right) \cdot \left(1 - A_{w,Encapsulant}(\lambda)\right) \cdot \left(1 - R_{w,SiNx}(\lambda)\right) \cdot A_{w,Cell}(\lambda) \cdot \left(1 - IQE(\lambda)\right) d\lambda \quad (2.34)$$

The thermal aspect of the time-independent matrix model is simplified compared to ray-tracing. The heat fluxes calculated in eqs. 2.29-2.34 do not account for multiple reflections at the SiN_x ARC or reflections at the cell back contact that lead to absorption in the encapsulant, glass, or thin-film mirror (multiple reflection within the cell itself is accounted for in the A_{Cell} matrix). For the baseline module, we estimate a total of ~4.5 W m^{-2} out of ~1000 W m^{-2} incident that is absorbed parasitically after reflection off of the SiN_x coating or the cell back contact which is ignored. The thermal benefit in the model depends on the difference between waste heat generated in a module compared to the baseline, so the error in the waste heat difference introduced by ignoring absorption after reflection is not ~4.5 W m^{-2} of absorption after a first reflection in the baseline module, but is instead the difference in absorption after first reflection between the mirrored and baseline modules. By neglecting parasitic absorption after reflection, the model tends to under-predict thermal benefit, and it is estimated that the under-prediction is no more than 0.01% absolute.

Additionally, in both ray-tracing simulations and in the fractional absorption values in the A_{Cell} matrix the effects of free carrier absorption in the Si are not included. Free carrier absorption in a heavily doped n+ emitter layer would have a negligible effect on the absorption coefficient above the bandgap[113] and would not change the fractional absorption values in the A_{Cell} matrix at these wavelengths. Free carrier absorption would, however, increase the absorption coefficient for sub-bandgap wavelengths[119] which would increase the total parasitic absorption in the cell. Free carrier absorption could be incorporated into the model by including it during the ray-tracing used to calculate the A_{Cell} matrix. We estimate that free carrier absorption would increase the total waste heat flux generated by

the module ~2 W m^{-2} in the baseline module under 1000 W m^{-2} incidence.[120] A mirrored module would reflect some of this additional 2 W m^{-2} before it is absorbed by free carriers in the cell, thus increasing the difference in waste heat flux between the baseline and mirrored modules. We estimate that inclusion of free carrier absorption would increase the thermal benefits calculated by both the matrix model and the full opto-electro-thermal simulations by at most 0.02% absolute.

2.5. Optimization of Mirrors Using the Time-Independent Matrix Model

The Time-Independent Matrix Model presented above estimates the increase in annual energy yield for a photovoltaic module installed outdoors upon application of a spectrally-selective mirror. Therefore, a single execution of the model can evaluate a given mirror design. Finding a successful design, however, requires iteration of the model to optimize its result. A brief description of the optimization method is given here.

For optimization purposes, the mirror is defined by a sequence of materials with known refractive index, including the substrate and superstrate materials, and a corresponding sequence of thicknesses. During optimization, only the layer thicknesses are subject to change, the number of layers and the material of each layer are never changed. Therefore, optimization occurs in n-dimensional space, where n is the number of mirror layers. Layer thicknesses are optimized using the Nelder-Mead simplex algorithm.[121] A set (simplex) of $n + 1$ points are chosen in n-dimensional space such that the set of vectors connecting each point to the origin are linearly-independent. The function to be optimized is evaluated at each point. A new point is chosen by reflecting the least optimal point through the centroid of the remaining points, and afterwards discarding the least optimal point. Optimization is finished when all points in the simplex are within a predefined distance from one another.

Crucially, the simplex algorithm does not search for local minima using the gradient of the function being optimized. While in principle, there is nothing wrong with applying a gradient-descent algorithm to this problem, in practice such an algorithm fails to find a useful mirror design, since the origin is always a local minimum of the Time-Independent

Matrix Model with zero energy yield increase. If layer thicknesses in the initial structure fed into the optimization algorithm are chosen at random, or are set to have a particular reflection band as in a Bragg stack, then it is extremely likely that the initial energy benefit is negative. Subject to gradient descent, the origin is always a possible terminus. The simplex algorithm avoids this as long as a single point exists in the simplex at any step corresponding to a mirror design with an energy benefit.

The simplex algorithm only operates on the layer thicknesses of a mirror design. It does not decide the materials in each layer or the number of total layers. For this, a needle-insertion step[122] occurs after every optimization step. The needle insertion algorithm takes the optimized mirror design and attempts to insert a new layer (needle) of small thickness inside the existing stack. Each layer of the optimized design is a candidate for the host of a new layer, and the new material is selected from a library of possibilities provided by the user. The combination of material and needle location which results in the greatest improvement in evaluation of the function being optimized is selected after all possibilities have been tried. Applied to optimization of the Time-Independent Matrix Model, each attempt at needle insertion requires a full re-optimization of layer thicknesses, including the needle. It is possible to check the improvement of the needle by only considering the gradient of the energy yield increase, where the needle would effectively have differential thickness. However, a needle with a large gradient but small thickness after re-optimization would be chosen over a needle with a smaller gradient but much larger final thickness, providing possibly much larger improvement in energy yield. Checking each needle by re-optimization is necessary to consistently pick the best result.

With the combination of simplex algorithm optimization and needle insertion, a typical mirror design is optimized using an initial structure consisting of only a few layers. Each needle insertion increases the layer count by two, one for the needle, and one for the existing layer which it split into two parts. Design terminates after a pre-selected number of needle insertions. In the final design, layers which had substantial thickness in a previous optimization step may have near-zero thickness. These layers are deleted manually, and the energy yield increase predicted by the Time-Independent Matrix model is continuous with respect to these deletions.

Chapter 3 - Designing Effective Mirrors for Photovoltaic Thermal Management

3.1. Introduction

A typical c-Si photovoltaic module will operate 20-30K above ambient temperature, but only convert ~20% of the incident light into energy, with the remainder either reflected or wasted as heat.[70] In this thesis, a strategy to reduce the waste heat produced by photovoltaic modules by selectively reflecting sub-bandgap light is developed. For c-Si photovoltaic modules, ~19% of incident sunlight is below the bandgap, whose parasitic absorption can be prevented without interrupting module energy production. As a result, module operating temperature would decrease, with a corresponding increase in efficiency and energy yield. However, the design of photonic mirrors to achieve this spectrally-selective sub-bandgap reflection presents two main challenges. The mirror would interact not only with sub-bandgap light, but with the full solar spectrum, including sunlight above the bandgap which is converted in the cell. The ideal photonic mirror would not only reflect sub-bandgap radiation, but also transmit radiation at energies higher than the bandgap to maintain or improve energy production. Therefore, a 1-D photonic crystal, or Bragg stack, with a primary reflection band in the sub-bandgap range will not suffice for this application due to the additional reflection at wavelengths in the useful part of the spectrum.[7] For the sunlight with energy greater than the bandgap of the solar cell, the photonic mirror should instead provide an antireflective effect that allows more light into the cell compared to a reference module, improving energy output from the cell.

A second challenge of photonic mirror design is omnidirectionality. While an ideal photonic mirror would operate with perfect spectral selectivity at all angles of incidence, this is difficult to achieve in a practical photonic mirror design, and impossible in those based on layers of thin films. Real modules are of course installed in specific locations with varying direct and diffuse components of the incident radiation depending on mounting and system design, and so not all angles of incidence are equally represented. For example, in a latitude-tilt module in Golden, Colorado, 22.4% of the energy arrives to the module at

angles between 20° and 30° due to daily and seasonal variation in solar position. The peak occurs at 23°, equal to the tilt in Earth's axis. The photonic mirror therefore should not be designed for normal incidence, but to capture sunlight according to the actual angles of incidence present in a given application.

In this chapter constraints on photonic mirror design based on aperiodic, one-dimensional layers of thin films are identified. An early version of the time-independent matrix model described in Chapter 2 is used to design the photonic mirror, which includes the expected energy received by a fixed-tilt module as a function of its angle of incidence, details of the AM1.5G spectrum, and the c-Si cell internal quantum efficiency. After optimization, photonic reflector designs are simulated using TOMCAT under real weather and irradiance conditions derived either from measurement[18] or historical data.[19] Performance is relative to a baseline c-Si module, with EVA encapsulant, cover glass, and a standard SiN_x antireflection coating on top of the Si pyramidal texture.

Idealized photonic mirrors placed at different interfaces within the module are examined in terms of their relative benefit from antireflection (optical) and cooling (thermal). These mirrors are omnidirectional, and increase solar module performance optically and thermally regardless of the angle of incidence of radiation. The mirror must be created considering the full range of incident angles, but it does not have to perform equally well at all angles. Using this constraint, photonic mirrors achieving similar performance regardless of tilt angle or location (Golden, CO or Seattle, WA) are shown. Finally, this chapter demonstrates that it is possible to optimize photonic mirrors with fewer than ten layers and create designs which improve the baseline module, especially when optimizing for the air/glass interface. These photonic mirrors generally act as antireflection coatings with a small thermal benefit, but may be easier to fabricate than more complex designs. A discussion of one such photonic mirror is provided here, with further discussion in Chapter 5.

3.2. Benefits of Idealized Mirrors

Before discussing the design of realistic mirrors, we first consider idealized photonic mirrors, including antireflection coatings, ideal sub-bandgap reflectors (SBR), and various combinations. While these mirrors have properties that are not physically attainable, they

represent boundaries on the best possible performance offered by a photonic mirror at a particular module interface. These results offer insight into the interface(s) within the module where photonic mirrors are most effective. Still, an individual mirror does not have to accomplish all of the benefits simultaneously, as the mirrors at different interfaces could be designed cooperatively. Photonic mirrors could be placed on the outside of the glass (air/glass interface, or AG), within the module between the glass and the EVA encapsulant (glass/EVA interface, or GE), or between the encapsulant and the solar cell (EVA/solar cell interface, or ES). At the ES interface, the photonic mirror replaces the SiN_x antireflection layer in the baseline module. We have previously considered the performance of an ideal SBR, ideal ARC, and the combination of an ideal SBR and ideal ARC in these modules, but not the explicit design criteria for mirrors at each interface.[92]

As discussed in Chapter 2, the performance of a given photonic mirror is measured relative to a baseline case without the mirror. Therefore, the properties of the existing interfaces determine the potential for benefit of a photonic mirror. For example, at the air/glass interface, there is ~4% reflection at normal incident which could be eliminated by a photonic mirror. Indeed, commercial solar modules often use antireflection coatings on top of the glass to reduce this reflection.[123] In contrast, the glass/encapsulant interface in the interior of the module has <0.1% reflectivity across almost all wavelengths considered in this work, so no photonic mirror, idealized or otherwise, would be able to significantly reduce reflection.

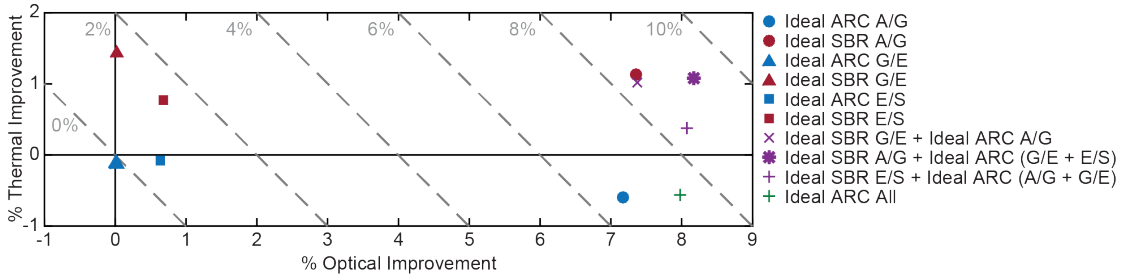

Figure 3.1*: Properties of ideal photonic mirrors at various interfaces within the module. An ideal ARC has no reflection at any wavelength. An ideal SBR reflects all sub-bandgap light, but otherwise has no reflection. A/G is the air/glass interface. G/E is the glass/EVA interface. E/S is the EVA/Si interface (with pyramid surface texture). A '+' in the legend indicates the presence of a second or third photonic mirror at another interface.*

Results of the ideal photonic mirror simulations are shown in **Figure 3.1**, showing the simulated relative percent optical improvement against the simulated percent thermal improvement. Simulations are based on a full year of weather and irradiance data typical for Golden, CO. Immediately, the data make apparent differences in performance depending on the interface and type of photonic mirror. At the air/glass interface, the antireflection provided by either and ideal SBR (red circle) or ideal ARC (blue circle) provides a >7% optical benefit. However, for the ideal ARC there is a thermal penalty of ~0.6%, indicating that the module with the ARC operated on average at higher temperature than the baseline. The thermal penalty arises from the additional transmission of light at all wavelengths provided by the ARC. For sub-bandgap wavelengths, this leads to parasitic absorption which directly heats the module above the baseline module temperature. At photon energies above the bandgap, the antireflection allows the creation of additional current, and gives an optical benefit. However, the extra waste heat from thermalization and carrier recombination contributes to the thermal penalty. Therefore, for any antireflection coatings, there will be some thermal penalty due to the additional current generated compared to baseline.

An ideal SBR, however, does offer a thermal benefit since it allows a given interface to reflect all sub-bandgap radiation. The greatest thermal benefit is possible at the glass/EVA interface (~1.4%, red triangle), because the glass and EVA are nearly index-matched, and the interface is very transmissive in the baseline module. Therefore, adding an ideal SBR at this interface gives a high thermal benefit from sub-bandgap reflection, which is not reduced by additional thermalization. However, the optical benefit is approximately zero at this interface. At the air/glass interface, the ideal SBR retains the optical benefit of the ideal ARC and offers a ~1.1% thermal benefit. Compared to baseline, this is a lower thermal benefit that that offered by the ideal SBR at the glass/EVA interface, as the optical benefit of the SBR on glass causes additional waste heat from thermalization and carrier recombination. But, comparing the difference in thermal benefits of the ideal ARC and ideal SBR applied to the air/glass and glass/EVA interfaces, the ideal SBR offers a greater increase in thermal benefit over the ideal ARC when applied to the glass (~2.1%) than between the glass and EVA (1.5%). This comparison suggests that, given perfect sub-

bandgap reflection, the air/glass interface is the best choice for the reflector in terms of thermal benefit.

The design and optimization of photonic mirrors for the interface between the EVA and the Si cell is discussed in a later chapter, however simulation results for an ideal ARC and ideal SBR at that interface are shown in **Figure 3.1**. For these simulations, the baseline module contains a 75 nm SiN_x anti-reflection layer on top of the pyramidal surface texture of the cell, both of which affect the results of the ideal case simulations. The 75 nm SiN_x layer is already very effective, with the ideal ARC (blue square) and ideal SBR (red square) providing only ~0.6-0.7% optical improvement, and the ideal SBR giving an ~0.8% thermal improvement. So while there is some improvement possible at this interface, any designs must consider the existing pyramid surface texture of the cell.

Finally, ideal photonic mirrors could be incorporated at multiple interfaces. In this approach, only a single SBR is beneficial, as the sub-bandgap light only need to be reflected once. But, incorporation of ARCs at other interfaces offers additional benefit. For example, a module with spectrally-selective photonic mirror at the glass/EVA interface would benefit from the addition of an antireflection coating at the air/glass interface. In the case of an ideal SBR at the glass/EVA interface and an ideal ARC at the air/glass interface (purple x-mark), simulation results indicate similar performance to an ideal SBR at the air/glass interface, with a slightly smaller thermal benefit from parasitic absorption in the glass. Similarly, placing the ideal SBR at the EVA/Si cell interface has a smaller thermal benefit due to absorption of sub-bandgap light in the upper layers of the module. Ideal ARCs at all interfaces yields the maximum possible optical benefit, with a thermal penalty of ~0.6% for reasons discussed above (green plus sign). The best possible module, however, would be in the case of an ideal SBR at the air/glass interface, and ideal ARCs at other interfaces (purple star). The ideal SBR at the air/glass interface reflects sub-bandgap light away before it reaches any other interfaces, and the module has a ~1.1% thermal improvement in addition to the ~8% optical improvement offered by antireflection.

3.3. Photonic Mirrors at the Air/Glass and Glass/EVA Interfaces

Photonic mirrors comprised of one dimensional layers of were constructed using an early version of the model described in Chapter 2. For the mirrors discussed in this chapter,

the results of optimization and the results of full year finite element opto-electro-thermal simulations are not in as good agreement as in later chapters. However, these mirrors still have realistic spectral and angular reflection properties, and demonstrate several qualities necessary for successful spectrally-selective photonic mirrors. Briefly, the early version of the optical benefit is given by eqs. 3.1 and 3.2.

$$I = \int_{300\ nm}^{1100\ nm} \left(1 - R_{w,Mirror}(\lambda)\right) \cdot IQE(\lambda) \cdot \varphi_{AM1.5G}(\lambda) d\lambda \tag{3.1}$$

$$B_{Optical} = 100\% \cdot \left(\frac{I}{I_{Baseline}} - 1\right) \tag{3.2}$$

The thermal benefit in this early model is given by eqs. 3.3 and 3.4.

$$P = \int_{1100\ nm}^{2500\ nm} R_{w,Mirror}(\lambda) \cdot P_{AM1.5G}(\lambda) d\lambda \tag{3.3}$$

$$B_{Thermal} = \frac{P - P_{Baseline}}{30\ W/K} \cdot 0.39\ \%/K \tag{3.4}$$

Mirrors were constructed for the air/glass interface (photonic mirror AG1) and the glass/EVA (photonic mirror GE1) interface. The initial structure for both AG1 and GE1 was five periods of a quarter-wave Bragg stack targeted for maximum reflection at 1250 nm. These photonic mirrors were optimized and simulated using weather and irradiance data assuming a latitude-tilt module in Golden, CO (39.742 N, 105.179 W). In addition, we simulated a commercial antireflection coating (glass ARC) both on its own at the air/glass interface, and in conjunction with photonic mirror GE1. The glass ARC is a 99 nm porous SiO_2 layer as described in section 3.2 of Vogt.[49]

Figures 3.2a-b show net reflection at all wavelengths and angles of incidence from photonic mirrors AG1 and GE1, respectively. Net reflection is the difference between the reflection of the particular interface with and without the photonic mirror. Blue-shaded areas are regions of reduced reflection, while red-shaded areas are regions where there is additional reflection compared to the bare interface. Note that for both AG1 and GE1, the center wavelength of the reflection band at normal incidence shifted from the initial design wavelength of 1250 nm to ~1400 nm for AG1 and ~1600 nm for GE1. This ensured that there are no angles of incidence for which light with energy greater than the bandgap is strongly reflected. Additional reflection at longer wavelengths in both structures is attributed to side lobes remaining from the reflection spectrum of the initial Bragg stack.

The reflection band at less than 400 nm in both structures is attributed to a harmonic of the main reflection band also present in the initial structure which was not completely suppressed by the aperiodicity introduced during structure optimization.

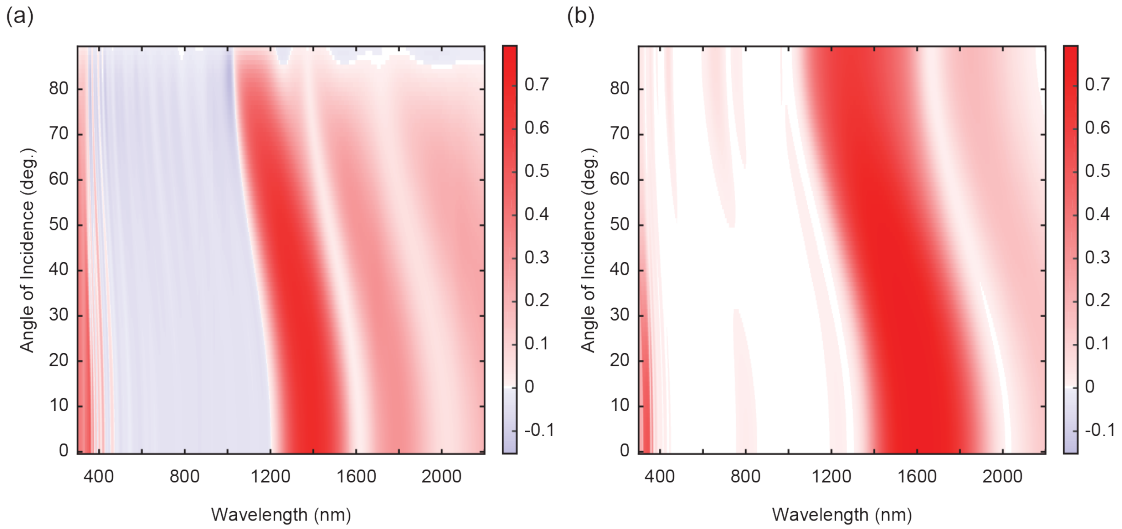

***Figure 3.2**: (a) Net reflection from photonic mirror AG1 at the air/glass interface. (b) Net reflection from photonic mirror GE1 at the glass/EVA interface. Blue shades indicate a reduction in reflection, the module with the photonic mirror reflects less light at that wavelength and angle than the module without. Red shades indicate increased reflection due to the photonic mirror.*

Aside from the harmonic reflection band, in the range 300 – 1100 nm reflection is very low at all angles in both structures. For AG1, reflection is low enough to provide antireflection at most useful wavelengths and most angles since the air/glass interface itself is reflective. However, even though reflection from GE1 is very low in the useful range, it is not low enough to provide substantial antireflection compared to the glass/EVA interface. Again, since the glass and EVA are nearly index-matched, reflection is less than 0.1% at normal incidence across all wavelengths, which limits the potential optical benefit of photonic mirrors at that interface and places a strict standard for breaking even in terms of optical benefit. While thermal benefit is still possible at the glass/EVA interface, it must outweigh the likely optical detriment to produce a net energy improvement. At normal incidence, integration of the reflection spectrum shows that AG1 reflects 41.8 W/m^2 sub-bandgap power while GE1 reflects 53.6 W/m^2, both out of 174 W/m^2 sub-bandgap power incident upon the structure.

Full year simulations were then run using these two photonic mirrors to find the optical improvement, thermal improvement, and overall energy output improvement. These results are also compared to the estimates of the optical improvement and thermal improvement obtained from the objective function calculation alone (**Figure 3.3**). Due to the antireflection provided by AG1, both the objective function (red empty circle) and the simulation (red filled circle) give a large optical benefit and a small thermal benefit (3.44% and 0.2% for the simulation), although these are both considerably smaller than the ideal case (7.36% and 1.13%, respectively, from simulation). For GE1, however, both the objective function (empty red triangle) and simulation (red filled triangle) give a small optical detriment (-0.29% from simulation) since the photonic mirror is still slightly more reflective than the glass/EVA interface in the region from 300 – 1100 nm. For the glass ARC simulation (blue filled square), there is an optical improvement of ~2% and a thermal penalty of -0.3% (compared to 7.17% and -0.6% for the ideal ARC). When acting in tandem with GE1 (purple filled square), the glass ARC provides the optical benefit (slightly reduced by the presence of GE1) and GE1 provides the thermal benefit. The largest thermal benefit is found for the GE1 case, the largest overall benefit is found for the AG1 case due to the antireflection improvement, and GE1 with a glass ARC provides a compromise.

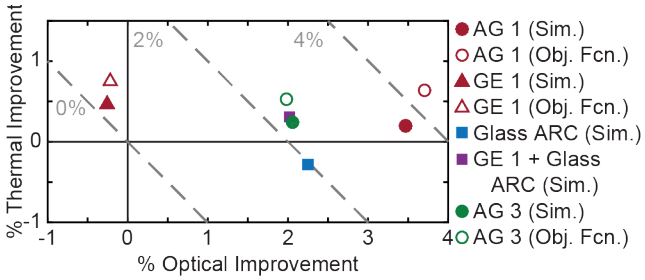

***Figure 3.3**: Objective function (Obj. Fcn.) values and simulation (Sim.) results for mirrors AG 1, GE 1, and AG 3. The Glass ARC is a 99 nm porous SiO2 antireflection coating and is placed at the Air/Glass interface. 'GE 1 + Glass ARC' is a simulation with both GE1 at the Glass/EVA interface and the Glass ARC at the Air/Glass interface.*

The objective function used to design the mirrors here is an earlier form of the time-independent matrix model described in Chapter 2, which only depends on changes in reflection at the interface containing the mirror. While this allows design of effective mirrors, there is some disagreement between the objective function results and simulations results. For AG1, there is a disagreement of ~0.4% absolute, and ~0.3% absolute for GE1.

In subsequent mirror optimizations, these disagreements were resolved by developing the time-independent matrix model to calculate absorption throughout the module. This earlier version tends to overestimate optical and thermal benefit because of two assumptions implicit when only considering reflection at the mirror interface: first, that all light above the bandgap transmitting through the mirror is absorbed in the cell, and second, that sub-bandgap light reflected from the mirror has its absorption prevented. The first assumption ignores ultraviolet absorption in the glass and encapsulant and reflection from the cell. Not all light passing through the mirror reaches the cell, and since the mirror reduces the interface reflection at most wavelengths above the bandgap, the optical benefit is generally overestimated. The second assumption ignores the possibility of light escaping from the module without being absorbed. In the sub-bandgap spectral range, it is possible for light to reflect from the metallic cell rear contact without being absorbed, pass again through the cell, encapsulant, and glass, and leave the module entirely. Then, the waste heat prevented by the mirror is not equal to the sub-bandgap power reflected at the mirror interface, but in reality (and simulation) is reduced by the portion of light which escaped the module without being absorbed.

3.4. Effect of Changing Module Tilt Angle and Geographic Location

Next, we consider the omnidirectionality of the mirror. The main challenge in creating photonic mirrors based on one-dimensional layers is the changing reflectivity with angle of incidence, as the reflection values will significantly increase and blue shift at oblique angles. However, not all angles are represented equally in the spectrum. **Figure 3.4** shows the fraction of total energy received at each angle by a module in Golden, CO at latitude tilt, a tilt angle of 30°, and a tilt angle of 20°. Lower than latitude tilt angles are typically used in large solar arrays or in areas where space is constrained to prevent one module from shading another.[124] At latitude tilt, the angle of incidence of beam radiation with the module is lowest near the equinoxes. At lower tilts, the beam radiation comes at the lowest angles in the winter and higher angles in other seasons. The peak angle is no longer 23°, but instead shifts to higher angles: 32° at 30° tilt and 42° at 20° tilt. Secondary peaks show up at lower angles as well: 13° at 30° tilt and 3° at 20° tilt in Golden, CO.

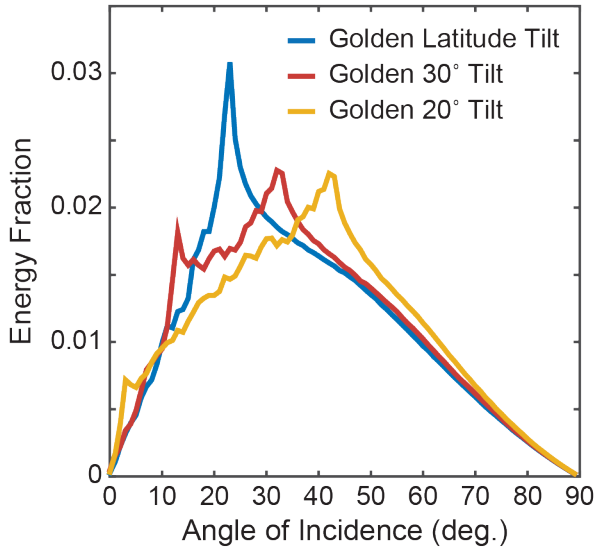

***Figure 3.4**: Comparison of the fraction of expected energy on a module in Golden, CO at latitude tilt, 30 degree tilt, and 20 degree tilt.*

The importance of considering these incident angles during mirror design can be revealed by comparing two mirror structures. First, AG1, which was constructed considering the relative amounts of energy incident at all angles, and photonic mirror AG2, which is an intentionally sub-optimal structure constructed considering reflection only at 23°, beginning with the same initial structure as AG1. **Figure 3.5a** shows the objective function values for photonic mirrors AG1 and AG2 considering only one angle at a time. For photonic mirror AG1, peak performance occurs under illumination at 60°, and there are no angles where AG1 is detrimental. However, for photonic mirror AG2, peak performance occurs near 23° incidence, the only angle for which reflection was considered during optimization. For angles closer to normal incidence, the performance of AG2 remains beneficial, but at angles higher than 23° the performance decreases, becoming detrimental under illumination at angles greater than 50°. A net reflection plot for photonic mirror AG2, given in **Figure 3.5b**, shows that its reflection band is red-shifted compared to that of AG1 such that the reflection band edge is at 1100 nm at 23°. The poor objective function value is entirely due to reflection of light at wavelengths shorter than 1100 nm for angles greater than 23°.

Given that AG1 is a more omnidirectional mirror, it performs well as the tilt angle is lowered. A change in module tilt angle changes the peak angles at which radiation is received. **Table 3.1** shows the results from the full simulation, which indicate that the

optical improvement is slightly enhanced as the module tilt is lowered for 20° tilt. The thermal benefit declines slightly at all conditions other than the optimization condition, and is slightly worse at 30° tilt than at 20° tilt.

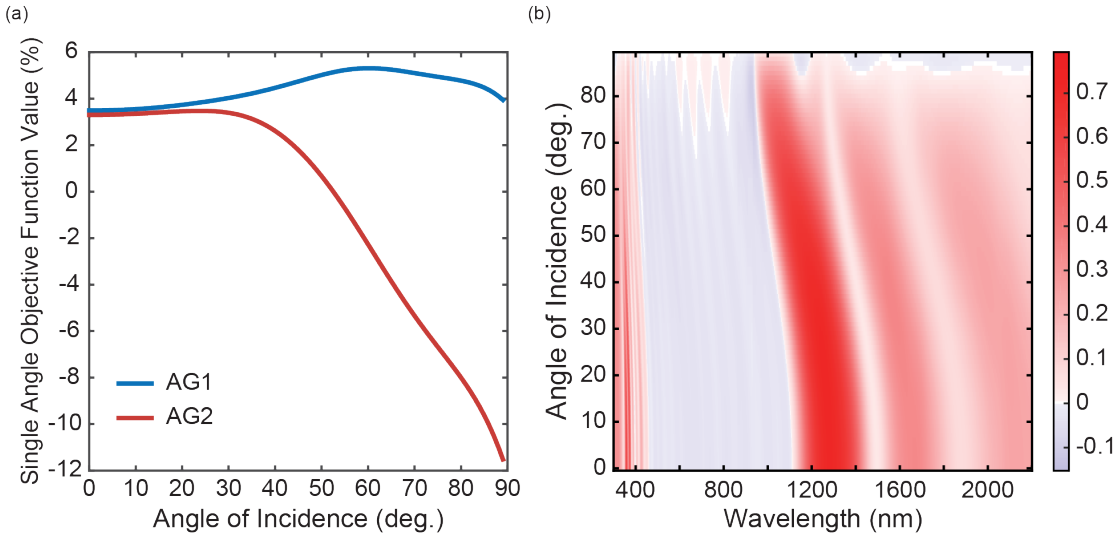

***Figure 3.5**: (a) The objective function values of photonic mirrors AG1 and AG2 evaluated separately at each angle. (b) The net reflection of AG2. Net reflection is defined as the difference in reflection of the interface with and without the mirror. Blue-shaded regions correspond to reduced reflection, while red-shaded regions correspond to increased reflection.*

These results indicate that, despite the presence of peaks in the radiation at specific angles, a one-dimensional photonic mirror based on layers of thin films should not be designed for the peak angle. For these mirrors, the blue shift of reflection features with increasing angle of incidence means that if a reflection band in a structure is placed to reflect the most sub-bandgap light at 23° incidence (as in the latitude tilt case) while not reflecting light with energy greater than the bandgap, blue shift of the reflection band will decrease module performance for light incident at higher angles. A substantial portion of the spectrum is incident at higher angles. For the air/glass interface, the baseline reflection increases from ~4% at normal incidence to over 20% at higher angles, and so the antireflective behavior of the photonic mirror at high angles can also lead to better performance. The harmonic reflection band is also blue-shifted at steep angles, which reduces reflection in the wavelength range from 300 to 400 nm and improves antireflection.

To better understand the role of radiation from all angles, we study the performance of the mirror under diffuse light and beam light separately. **Figure 3.6** shows scatter plots

of the time series simulation results for photonic mirrors AG1 and AG2 in Golden, CO at latitude tilt, in parts (a) and (b), respectively. Each dot represents a single 5-minute timestep in the simulation; only daytime data are shown, excluding twilight periods. The scatter plots show the total advantage, the sum of the simulated optical and thermal advantages at that time point, against the beam angle of incidence for that time. Each dot is colored by the fraction of plane of array irradiance received by the module at that time point attributable to beam radiation. Blue colored dots correspond to times with nearly zero beam radiation, or nearly 100% diffuse radiation, while yellow colored dots correspond to times with nearly 100% beam radiation. A beam angle of greater than 90° indicates that the beam radiation is located behind the module. This condition dictates that 100% of the incident light is diffuse.

Table 3.1: Simulation Results at Varying Location and Module Tilt Angle

Photonic Mirror	**AG1**				**AG2**
Optimization Location/Tilt Angle	Golden, CO Latitude	Golden, CO Latitude	Golden, CO Latitude	Golden, CO Latitude	Golden, CO Latitude
Simulation Location/Tilt Angle	Golden, CO Latitude	Golden, CO 20 deg.	Golden, CO 30 deg.	Seattle, WA Latitude	Golden, CO Latitude
% Optical Improvement	3.44	3.55	3.42	3.43	2.03
% Thermal Improvement	0.20	0.15	0.13	0.12	0.22
% Total Improvement	3.64	3.70	3.55	3.55	2.25

A difference in performance under beam and diffuse light is apparent. When the beam fraction is low and most of the plane of array irradiance is diffuse, the module performance is always the same, regardless of the beam angle of incidence. Diffuse radiation is incident with at least some energy at each angle of incidence, so the performance under diffuse radiation depends on reflectivity at all angles of incidence. Under beam radiation, however, the module performance increase due to the photonic

mirror depends on the beam angle of incidence. As was predicted by the objective function calculations shown in **Figure 3.5a**, better performance for AG1 is achieved under high angles of incidence than low angles of incidence, even though AG1 was constructed with a peak in energy received at 23°.

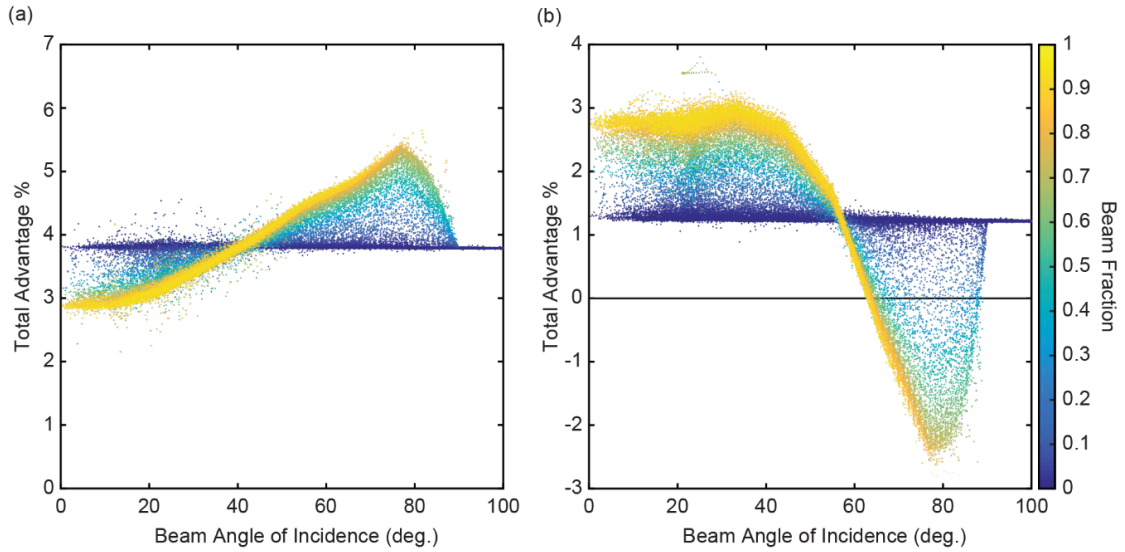

***Figure 3.6**: Scatter plot of simulated percentage power increase relative to baseline versus the beam angle of incidence for (a) AG 1 and (b) AG 2. Each dot represents a 5-minute daytime interval in the simulation, excluding twilight periods. The dots are colored according to the fraction of the plane of array irradiance coming from the solar beam. Blue colors signify nearly 100% diffuse light, yellow colors signify nearly 100% beam light. When the beam angle of incidence is greater than 90°, the Sun does not shine on the front of the module, and all incident light is diffuse. About 28% of the points have a beam fraction greater than 0.8 and about 43% have a beam fraction less than 0.2.*

A similar analysis applies to AG2 as well, and demonstrates the poor performance at high angles of incidence. As with AG1, the performance under diffuse light is constant regardless of the beam angle of incidence and the performance under beam light depends on its angle of incidence. However, AG2 performs worse under beam illumination at more oblique angles than it does at near normal angles, again due to reflection of light with energies above the bandgap at high angles. And, because of this detrimental reflection, performance under diffuse light is reduced for AG2 relative to AG1. Full simulation results, shown in **Table 3.1**, indicate that a module with photonic mirror AG2 produces 1.5% less energy than a module with photonic mirror AG1.

To further examine the omnidirectionality of optimized photonic mirrors, we consider a change in the physical location of the module. Photonic mirror AG1 was originally optimized for and simulated in a latitude-tilt module in Golden, CO. However, irradiance conditions vary from location to location. Seattle, WA, for example, has many more cloudy days than Golden (mean annual clearness index 0.462 for Seattle vs. 0.618 for Golden),[125] and receives a greater fraction of its sunlight as diffuse radiation rather than beam radiation.

In terms of the percent benefit offered by a mirror, a change in geographic location while maintaining the module at latitude tilt results primarily in a change in the fraction of total light received that is diffuse. **Figure 3.7** shows the fraction of energy received at each angle for a latitude tilt module in Golden and Seattle. The fraction of diffuse light increases from 32.7% in Golden to 38.7% in Seattle. Photonic mirror AG1 was simulated using weather and irradiance data corresponding to a latitude-tilt module in Seattle, with the result in **Table 3.1**. The optical improvement for AG1 in Seattle is reduced only 0.01% compared to Golden, and the thermal improvement is reduced by 0.08%. The optical performance is essentially identical between Golden and Seattle. Thermally, the reduction is most likely due to a drop in total irradiance going from Golden to Seattle.

An optimal photonic mirror will be omnidirectional in the sense that it will provide a net benefit for incident light at every angle. The photonic mirror does not have to be equally beneficial at all angles, nor most beneficial at peak angles of incidence. Since the photonic mirror performs differently at each angle of incidence, changing the location (the amount of diffuse light received) or the tilt angle (angles of peak energy) will only slightly change the overall performance benefit. Even if the module were placed in a location with very little diffuse light, consideration of more oblique angles of incidence is still necessary for beam radiation, as ~20% of the beam energy is incident at angles greater than 50°.

One motivation for designing a photonic mirror considering only one angle of incidence, as in the case of AG2, is that it may be possible at that angle to achieve significantly higher performance than for a mirror like AG1 which considers all angles. Our results, however, suggest that this is not the best strategy. In both objective function calculations (**Figure 3.5a**) and simulation results for high beam fraction conditions (**Figure 3.6**), photonic mirrors AG1 and AG2 perform similarly at low angle, until diverging around

23 degrees where performance of AG2 begins to decrease. Despite only taking into account 23 degree incidence, AG2 does not have better performance at that angle than does AG1. This suggests that there is no compromise between achieving excellent low angle and high angle performance simultaneously.

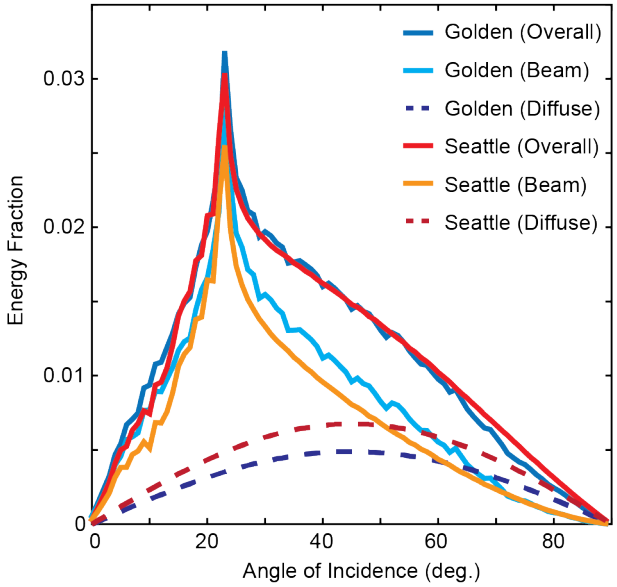

***Figure 3.7**: Plots of the energy fraction received versus angle of incidence for Golden, CO and Seattle, WA. The energy fraction is broken up into the component from beam radiation and diffuse radiation.*

3.5. Performance of Photonic Mirrors with Few Layers

In photonic mirrors AG1 and GE1, the initial condition for optimization was a Bragg stack, which required several 2-layer periods to create a reflection band. However, for photonic mirror AG1, its primary effect was antireflection of light in the 300 – 1100 nm range. The possibility is considered, then, of creating photonic mirrors with only a few layers without a reflection band, but still with excellent antireflection between 300 and 1100 nm. We optimized a new photonic mirror at the air/glass interface for Golden, CO at latitude tilt. Photonic mirror AG3 was constructed with an initial condition of just 2 layers, one Al_2O_3 layer on top of one Si_3N_4 layer and both with the same optical thickness as the layers in the initial condition of AG1. Layer thickness optimization and needle insertion were performed and a 10-layer structure was created. Since AG3 is not built based on a

Bragg stack, the thermal benefit of the structure was given additional weighting in the objective function to ensure that some thermal benefit is achieved.

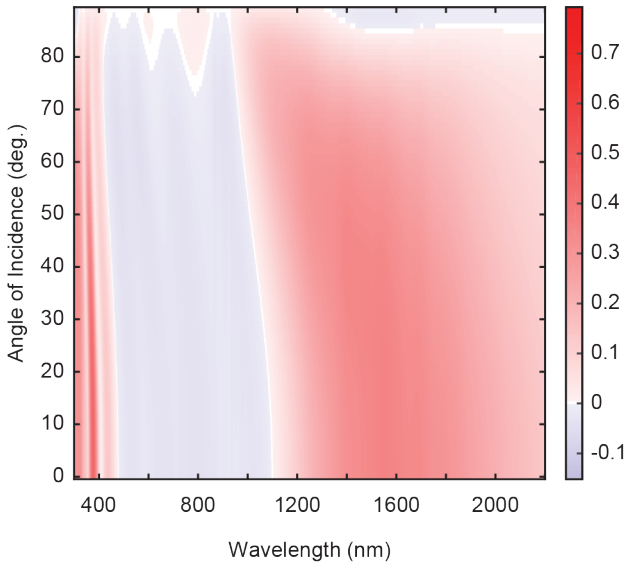

***Figure 3.8**: Net reflection from the photonic mirror AG 3 at the air/glass interface. Blue shades indicate a reduction in reflectance: the module with the photonic mirror reflects less light at that wavelength and angle than the module without. Red shades indicate increased reflection due to the photonic mirror.*

Figure 3.8 shows the net reflection from photonic mirror AG3 and **Figure 3.3** shows results of a simulation of a latitude-tilt module with photonic mirror AG3 in Golden (green circles). The net reflection plot shows that while there is not a reflection band as in the Bragg stack based structures, there is still significant sub-bandgap reflection. At normal incidence, 40.6 W/m^2 is reflected at wavelengths longer than the bandgap. At higher angles, photonic mirror AG3 begins to reflect useful radiation between 1000 and 1100 nm, which was avoided in the more complex structures. While the 2% optical benefit of photonic mirror AG3 is slightly less than the optical benefit of the glass ARC, AG3 provides a thermal benefit that the glass ARC does not, meaning that both antireflection and module temperature reduction are achieved. In fact, the ARC causes a thermal detriment to energy yield, which is turned into a benefit with AG3, a more sophisticated design accounting for sub-bandgap radiation. While photonic mirror AG3 does not perform as well as photonic mirror AG1, its advantage lies in the relatively simple structure and potential ease of fabrication. Further consideration is given to the performance of mirrors with few layers in Chapter 5.

3.6. Conclusion

This chapter examines the design of aperiodic photonic reflectors for integration into solar modules. These coatings act to reflect radiation with energies too low to be useful for photocurrent generation, preventing parasitic absorption of that radiation, cooling the module, and extending its service life.[92] At the top interface between air and glass, there is the possibility for antireflection of useful shortwave light, while maintaining or improving reflection of sub-bandgap light. Photonic mirrors between the glass and encapsulant still have the potential to reflect sub-bandgap light, but will likely not offer any antireflection, since the reflection at that interface is already extremely low. The photonic mirror presented in this chapter at the air/glass interface is able to provide antireflection and a small thermal benefit, increasing module energy by 3.7% compared to the baseline with no photonic mirror. By providing both increased photocurrent and module temperature reduction, our photonic mirrors are also an improvement over traditional ARCs, which increase module temperature and potentially decrease module lifetime. Enhanced performance is possible at the interface between the glass and encapsulant, however the thermal benefit must outweigh any penalty due to increased reflection of useful light. Our photonic mirror at that interface offers an 0.18% increase in energy, however in conjunction with a traditional antireflection photonic mirror at the top interface this performance could be improved further. While the results shown here are specific to crystalline Si modules, the general findings for mirror design criteria (omnidirectionality and placement within the laminate) are applicable to other materials systems.

Excellent photonic mirror performance is achieved when reflection at all angles of incidence is taken into account during construction of the mirror. The resulting mirror is omnidirectional in that it provides a net benefit under illumination at all angles. By following this guideline, a change in tilt angle or location does not significantly impact the performance of our photonic mirror. Finally, while this chapter was primarily centered around photonic mirrors based off of an initial starting Bragg stack structure, it is possible to start with much simpler initial conditions and achieve successful photonic mirrors with a relatively low layer count. Such photonic mirrors are worth considering for their ease of fabrication.

Chapter 4 Modeling the Effects of Spectrally-Selective Mirrors on Photovoltaic Module Energy Yield, Parasitic Absorption, and Waste Heat

4.1. Introduction

This chapter contains results and discussion of the time-independent matrix model described in section 2.4. Chapter 3 gives results of an initial and successful attempt to optimize the design of spectrally-selective thin-film mirrors for photovoltaic modules. However, the modeled and simulated energy yield improvements of Chapter 3 disagreed with the initial objective function used to design mirrors, tending to overestimate the energy yield increase found upon TOMCAT simulation. In contrast, the time-independent matrix model quickly and accurately assesses the energy yield increases from spectrally-selective mirrors, and offers insight into how both the antireflective and reflective aspects of the mirror affect waste heat and current production. The model computes ~1000 times faster than finite element simulation (<0.4s compared to ~400 seconds for a full-year simulation with one-hour time steps). To test the agreement of the model with existing simulation, two spectrally-selective mirrors for the outer module glass are designed by optimizing the model result. The optical and thermal benefits of each spectrally-selective mirror, as quoted by the time-independent matrix model at the end of optimization, should match the benefits given from the full opto-electro-thermal simulation of the same mirror designs. This chapter discusses why model agreement with simulation is achieved as well as limits to the agreement, and then studies how the introduction of spectrally-selective mirrors modifies the different loss pathways within the module.

4.2. Spectrally-Selective Mirrors

The time-independent matrix model was used to numerically optimize the design of two thin-film mirrors which increase the annual energy yield of a south-facing photovoltaic module installed at a tilt angle of 20° in Denver, CO (39.833° N, 104.65° W, 1650 m altitude). These mirrors are designed for the outer air/glass interface to reflect sub-bandgap

light and transmit light above the bandgap, replacing a single layer ARC. Mirror A has 13 layers and includes the materials SiO_2, SiN_x, and TiO_2, while mirror B has 20 layers and includes MgF_2 and Al_2O_3 in addition to the three materials in mirror A. The Appendix lists the materials and layer thicknesses for both mirrors. The initial condition for mirror A (13 layers) was a 5-layer structure consisting of three layers of SiO_2 and two layers of TiO_2, with each layer having 400 nm optical thickness, mimicking a Bragg stack although with very few periods. For mirror B (20 layers), the initial condition was a 7-layer structure with four layers of SiO_2 and three of TiO_2, each with 400 nm optical thickness. With these optical thicknesses, the initial structure has a reflection band centered around 1600 nm, but does not act as an anti-reflection coating from 300-1100 nm. Optimization of the initial structure maintains the reflection band while adding anti-reflection to improve current production.

Figure 4.1 shows the net reflection and net transmission from both of these mirrors as a function of wavelength and angle of incidence. Net reflection or net transmission refer to the difference between the reflectivity or transmissivity of the air/glass interface with and without the mirror. The plot is shaded such that blue colors refer to regions of decreased reflection (or transmission) while red colors refer to regions of increased reflection (or transmission). Since model calculations compare the mirrors to bare glass, the net reflection and transmission plots offer insight into how, and how well, the mirrors function. Plots of net reflection and net transmission for mirrors A and B compared to a 99 nm low-index porous SiO_2 single layer ARC (as described in Vogt[126]) are shown in the Appendix. As shown in **Figure 4.1a-b**, for both mirrors A and B, light at wavelengths in the sub-bandgap region (λ > ~1100 nm) is reflected much more strongly than for glass. For mirror A, there is a 52% absolute increase in reflectivity at the peak wavelengths around 1600 nm, while for mirror B the increase is 73%. Note, however, that the onset of reflection in the sub-bandgap region blue-shifts with increasing angle of incidence.[112] This blue-shift means that mirrors which begin to reflect near the bandgap wavelength under normal incidence will reflect useful light at higher angles of incidence. Optimized designs avoid reflecting useful light at any angle of incidence as it blocks that light from being converted to current, and reduces annual energy yield.

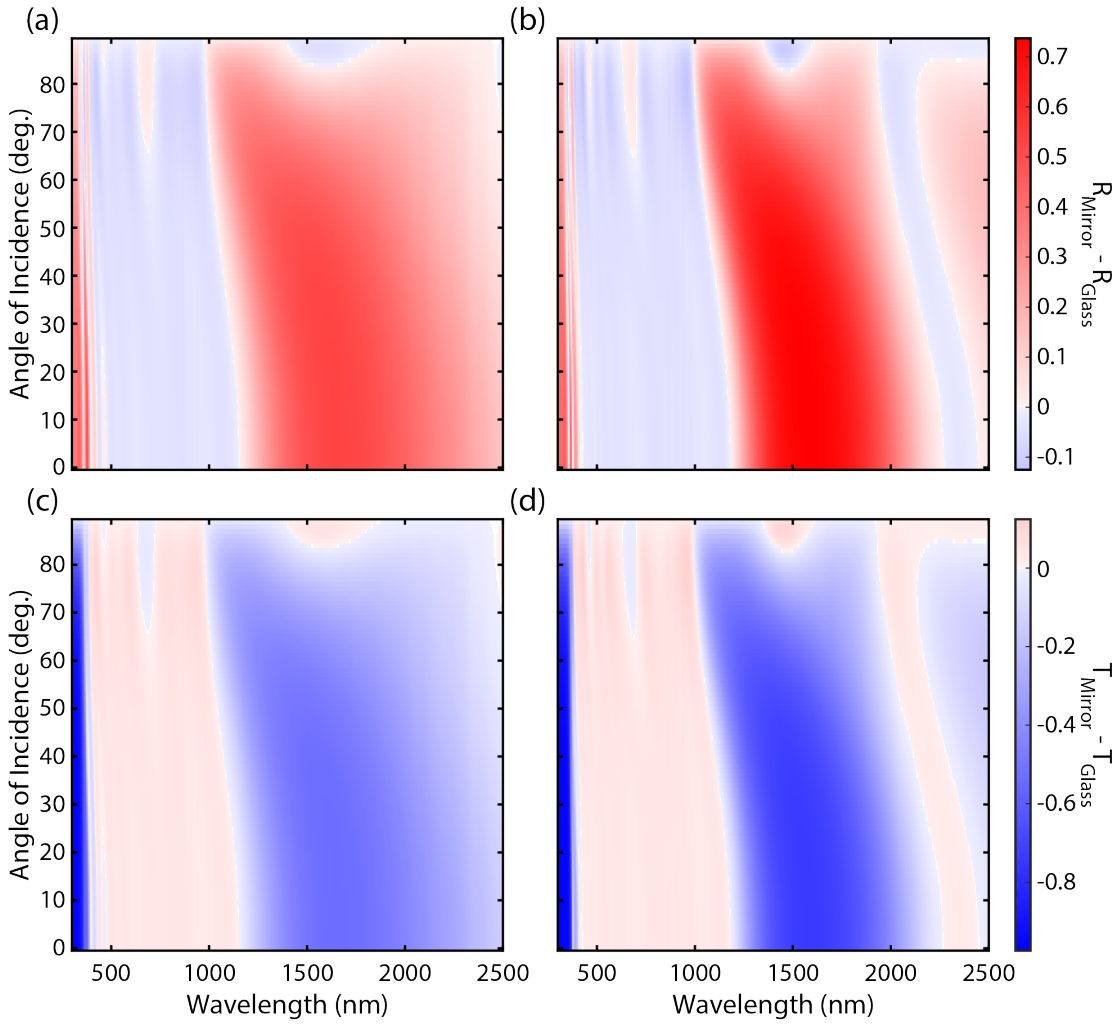

***Figure 4.1**: Net reflection ((a) and (b)) and net transmission ((c) and (d)) for mirrors A ((a) and (c)) and B ((b) and (d)). Net reflection (transmission) is the reflection (transmission) of the mirror less the reflection (transmission) of the bare glass. Blue shades indicate that the mirror is less reflective or transmissive, while red shades indicate greater reflectivity or transmissivity. Calculations are done via the transfer matrix method.*

The sub-bandgap reflection of mirror A is less than that of mirror B in terms of its peak magnitude, but its reflection bandwidth is larger compared to the bandwidth of mirror B. These differences are likely due to the different initial conditions for optimization. However, as both mirrors provide a 3-4% increase in energy yield compared to bare glass (see **Figure 4.2**, also discussed later in this chapter), the exact profile of the sub-bandgap reflection is not critical. Using the time-independent matrix model to optimize mirror design prevents reflection bands from interfering with photocurrent generation and

incentivizes having peaks in reflection at relatively shorter wavelengths in the sub-bandgap region where there is more AM1.5G spectral power.

Net transmission for mirrors A and B, shown in **Figure 4.1c-d**, again reveal that both mirrors transmit more useful light into the module regardless of angle of incidence, and transmit less light in the sub-bandgap region. Both mirror A and mirror B transmit an additional 3-4% absolute of the light in the visible range near normal angles of incidence compared to bare glass. For comparison, a conventional glass antireflection coating transmits only an additional 2-2.5% in the visible range. At glancing incidence, the transmittance increase for both mirrors is as high as 10% absolute. For these mirrors, it is also possible to absorb light as both TiO_2 and MgF_2 have an imaginary part of the refractive index. For both mirrors A and B, the TiO_2 layers absorb light at wavelengths less than 400 nm, reducing the transmission. For mirror B, MgF_2 weakly absorbs some light at all wavelengths (absorption of ~0.1% or less), slightly reducing transmission. Both mirrors A and B still increase transmission through the glass, but the changes to module current and waste heat are dependent on mirror absorption.

4.3. Comparison of TOMCAT and Time-Independent Matrix Model Results

4.3.1 Effect of Geographic Location and Module Tilt Angle

To verify that the time-independent matrix model predicts the same energy yield improvements as the full opto-electro-thermal simulation, we performed calculations of energy yield improvement for modules with both mirrors across a variety of locations and at module tilt angles of 20° and 30°. A module installed at one geographic location and tilt angle receives a different total amount of radiation and sees that radiation distributed over different angles of incidence than a module installed at a different location or tilt angle.[109,127] A change in the irradiance conditions to which a module is subject affects the energy yield benefit offered by a mirror, even if the mirror design itself does not change.

A comparison of the energy yield improvement of the time-independent matrix model and the full opto-electro-thermal simulation is shown in **Figure 4.2**. **Figure 4.2a** shows a scatter plot of the predicted total benefit from the model versus the simulated

values under the same conditions; **Figures 4.2b and c** show the results for the isolated optical and thermal components of the energy yield, respectively. The figures include data from simulations at 50 different locations, 48 corresponding to the continental United States and one each for a location in Alaska and Hawaii, and tilt angles of 20° and 30° for both mirrors. The black dashed line in all three panels of **Figure 4.2** is the y=x line, the line on which all data would fall if the model and simulations agreed perfectly.

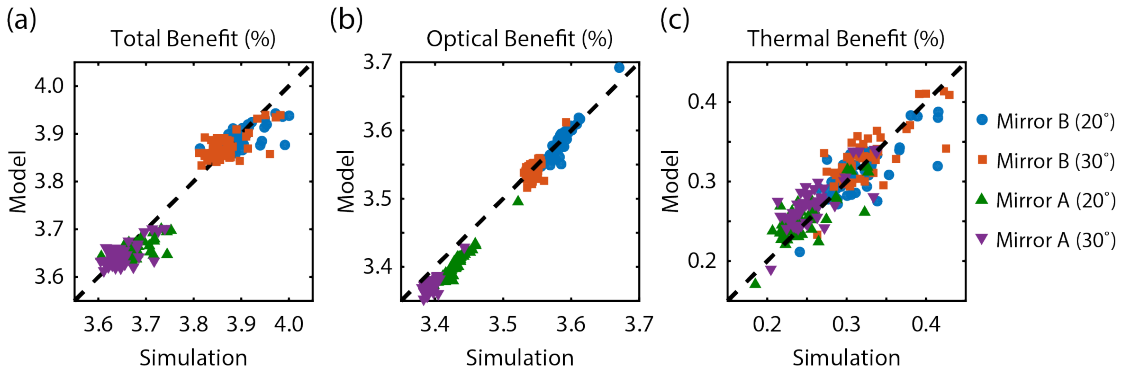

***Figure 4.2**: Comparison of total benefit (a), optical benefit (b), and thermal benefit (c) between the model and finite-element simulations. Plots include data for both mirrors A and B, simulated at 50 locations across the United States, and simulated at module tilt angles of 20 degrees and 30 degrees. The optical benefit is due to increased current produced by the module, while the thermal benefit is the increase in power due to an increase in the temperature-dependent cell efficiency.*

From **Figure 4.2a**, it can be seen that for 49 of the 50 locations, the simulated total benefit and the prediction given from the time-independent matrix model are the same to within 0.1% absolute. The exception, and the reason for the 0.1% confidence interval, is due primarily to wind speed and will be discussed in Section 4.3.3. From **Figure 4.2b**, it is seen that the optical benefit is in very good agreement with simulation: all are within 0.05% absolute of the simulated value. The optical benefit of mirror B is greater than that of mirror A, as the reflection decrease above the bandgap is better by up to 0.5% absolute for mirror B. The thermal benefits of mirrors A and B varies between ~0.2% and ~0.4%. These thermal benefits correspond to temperature reductions of ~0.5 – 1 K.

4.3.2 Irradiance Correction Factor

The thermal benefit is calculated using the difference in waste heat produced by the modules with and without the mirror, and thus depends directly on the magnitude of the

irradiance reaching the module. The model parameter $F_{irradiance}$ is included in the thermal benefit calculation to account for variation in average irradiance with module tilt and geographic location. The thermal benefits shown in **Figure 4.2c** are calculated using a value for $F_{irradiance}$ which varies with location and tilt angle between 0.38 and 0.71. A fixed value of $F_{irradiance}$ of ~0.6 can give thermal benefit prediction with agreement to 0.1% absolute across many locations and tilt angles. However, for modeling locations with exceptionally high or low total annual irradiance, or for arriving at a more accurate result in general, the correlation is useful. The thermal benefit of mirror B is higher than for mirror A at all locations as mirror B does have more sub-bandgap reflection.

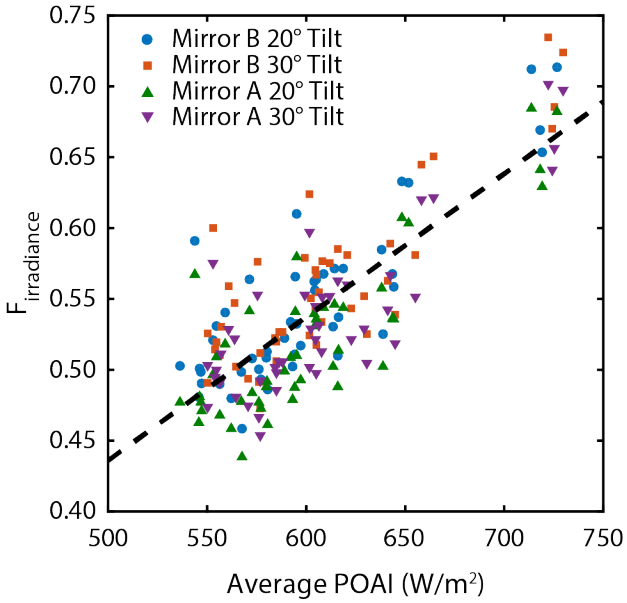

***Figure 4.3**: Data used to generate the correlation (dashed line) between $F_{irradiance}$ and average POAI. The raw data correspond to the value of $F_{irradiance}$ required to make the model and simulation agree exactly on thermal benefit. Simulations of both mirrors A and B, at module tilts of 20° and 30° were used.*

Figure 4.3 shows the data used to determine the correlation for $F_{irradiance}$. Each dot corresponds to a simulation in one of the 50 TMY3 locations for either mirror A or B, at a module tilt of 20° or 30°, the same simulations used in **Figure 4.2**. The x-coordinate is the contraharmonic mean of the time-series POAI determined from TMY3 data, which depends on both location and module tilt. The y-coordinate is the value of $F_{irradiance}$ required for the thermal benefits from the time-independent matrix model and TOMCAT simulations to agree exactly. The dashed line is a linear correlation (R^2 = 0.659), with the equation given by eq. 4.2.

$$\langle POAI \rangle = \frac{\sum_t POAI^2(t)}{\sum_t POAI(t)} \quad (4.1)$$

$$F_{irradiance} = 1.012\ x\ 10^{-3}\ \frac{m^2}{W} \cdot \langle POAI \rangle - 0.0700 \quad (4.2)$$

4.3.3 Effect of Wind Speed

Unlike the full simulations, the time-independent matrix model does not account for the effects of wind speed. However, wind speed greatly affects module temperature via convective heat transfer. The thermal benefits calculated using the time-independent matrix model and TMY3 data corresponding to one location, Roseburg, OR, were much lower than the simulated thermal benefits due to unusually low wind speed on average. At low wind speeds, the rate of convective heat transfer is reduced, and the module temperature must rise to maintain thermal equilibrium. The temperature difference between two modules increases when wind speed is low, even if the difference in total waste heat produced by those modules is constant. Therefore, low wind speed increases the thermal benefit from the mirror, which is captured in simulations but not in the model. To demonstrate the role of wind speed, the solid lines in **Figure 4.4** show the simulated thermal benefits for mirrors A and B in one location (Denver, CO) at module tilt angles of 20 and 30 degrees. The wind speed is changed to be *constant at all times* and equal to the value given on the x-axis. Dashed lines of the same color are the corresponding simulated thermal benefits from the unmodified simulation. Over the range of POAI-weighted average wind speeds present in simulations at any location (~2.6 m s^{-1} to 6.5 m s^{-1}) the thermal benefit varies by ~0.1%. Since the time-independent matrix model is ignorant of wind speed, agreement with simulation can only be within 0.1% absolute.

It may also be possible to correlate wind speed to thermal benefit in a similar manner to the total irradiance via a factor similar to $F_{irradiance}$. However, this is not done for two reasons. The first is that the finite-element simulations are 2-dimensional and use a one-parameter correlation to model convective heat transfer, following equations from Incropera and Dewitt (6^{th} Ed.).[128] Therefore, while in this paper we have matched a model prediction to simulated values, in terms of the effect of wind speed on thermal benefit, the results of the simulation are also uncertain as the correlation for 2-D geometries may not capture effects in a real 3-D system. Secondly, as shown in **Figure 4.4**, at low wind speeds

the thermal benefit is very strongly dependent on wind speed (within the convective heat transfer model used). Since wind speed can change drastically over short time periods, times with low wind may have a disproportionate effect on both simulated and possible experimental results. While there are other strategies to model convective heat transfer in photovoltaic arrays,[129,130] this model agrees with simulation within uncertainty due to wind.

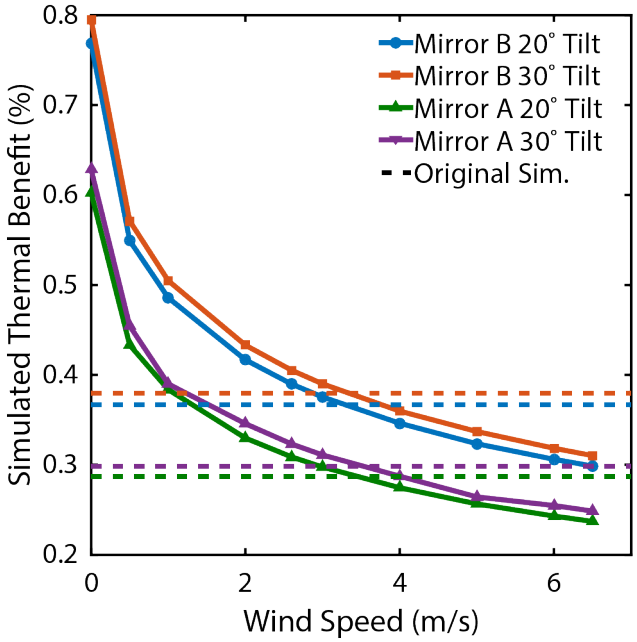

***Figure 4.4**: Thermal benefits for mirrors A and B in Denver, CO at module tilts of 20° and 30° based on full opto-electro-thermal simulations. The wind speeds in the simulations have been altered to be constant at the values shown on the x-axis (solid lines). The dashed lines of a given color are a reference for the corresponding simulation result with the actual time varying wind speeds. Thermal benefit decreases with increasing wind speed due to improved convective heat transfer.*

4.4. Effect of Spectrally-Selective Mirrors on Waste Heat Production

The time-independent matrix model also offers insight into the effect of the mirror on the various waste heat fluxes of the module. The optimum energy yield requires transmission of additional sunlight to increase current, balanced by the increased heat generated by these extra photons. By increasing reflection in the infrared, the thermal component of the mirror counteracts the elevated temperature gain from the improved antireflection.

Figure 4.5 shows the waste heat generated under 1000 W m^{-2} of AM1.5G radiation, with contribution from all angles of incidence, weighted to correspond to a module in Denver at a tilt of 20° facing south. All pathways for waste heat considered in the time-independent matrix model (absorption in the thin-film mirror, glass, and encapsulant, thermalization to the maximum power potential, and parasitic absorption) are shown. The output power is taken as the current produced multiplied by an operating voltage of 528 mV, assumed by the time-independent matrix model. Data are presented for five different cases: baseline, mirrors A and B, an ideal ARC, and an ideal sub-bandgap reflector (SBR). The ideal ARC has no reflection regardless of wavelength or angle of incidence, and the ideal SBR has no reflection above the bandgap and 100% reflection below the bandgap.

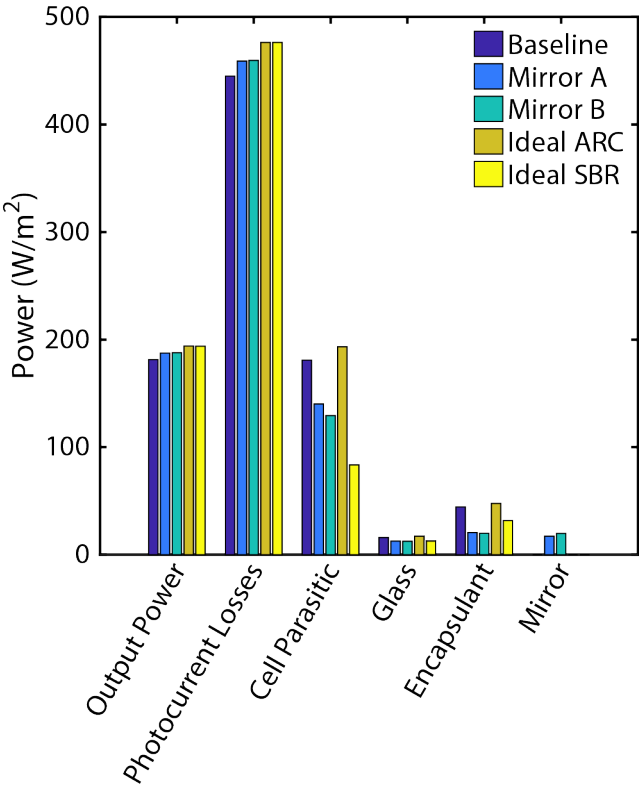

***Figure 4.5**: Module power and waste heat production for each possible pathway considered in the time-independent matrix model. The ideal antireflection coating (ARC) has no reflection at any wavelength regardless of angle of incidence. The ideal SBR has no reflection above the bandgap and 100% reflection below the bandgap. Photocurrent losses include the energy lost as carriers relax to the operating voltage equivalent energy of 528 meV. The output power term is equal to the current term calculated in the model, multiplied by the operating voltage of 528 mV.*

The thermal benefit of both spectrally-selective mirrors arises from a reduction in parasitic absorption throughout the module. In the baseline case, ~181 W m^{-2} of the incident 1000 W m^{-2} is absorbed parasitically in the Si cell, primarily in the back contact, which is reduced to ~140 W m^{-2} and ~130 W m^{-2} for mirrors A and B, respectively. The mirror additionally reduces parasitic absorption in the other module layers. For both mirrors A and B, the sum of heat absorbed in total by the spectrally-selective mirror, glass, and encapsulant drops by ~9 W m^{-2} and ~7 W m^{-2}, respectively, compared to baseline absorption in the glass and encapsulant. These reductions can be understood by referencing **Figure 4.1**. Mirrors A and B both reduce parasitic absorption by reflecting sub-bandgap light. While mirror B has 20 layers versus 13 in mirror A, the higher sub-bandgap reflection of mirror B allows it to reduce parasitic absorption slightly more than mirror A. Both mirrors also reflect some light in the range from 300-400 nm. These wavelengths are typically fully absorbed by the glass, encapsulant, or mirror itself before reaching the cell, so they cannot be usefully converted to energy in any module considered here. Therefore the mirror reflection from 300-400 nm is beneficial, as it prevents some light at those wavelengths from being absorbed at all, which reduces the total absorption outside of the cell compared to the baseline case.

For mirrors A and B and for the ideal ARC and ideal SBR, the optical benefit provided by increased current is slightly offset by an increase in waste heat from photocurrent production (~14 W m^{-2} for mirror A and ~15 W m^{-2} for mirror B). As more light is transmitted into the cell and more current produced, more heat is generated as those additional carriers lose energy before collection. In the case of mirrors A and B and the ideal SBR, the waste heat increase from photocurrent production is more than compensated for by reductions in parasitic absorption, leading to a thermal benefit for each mirror which is captured by the model. While a conventional ARC (or in an extreme case the ideal ARC) may provide an optical benefit, it comes with a thermal penalty from increased waste heat production. To provide a thermal benefit, the spectrally-selective mirror must reduce the parasitic absorption by more than the increase in waste heat from photocurrent. However, even if the mirror does not decrease temperature compared to a baseline case with no ARC, it may be providing an overall benefit by keeping the temperature increase to a lower value.

The ideal ARC and SBR are shown as examples of the effects of limiting cases on waste heat production. Both the ideal ARC and SBR allow all photons above the bandgap into the module, producing the largest possible current. However, the ideal ARC does not have any sub-bandgap reflection to reduce the parasitic absorption, and actually produces more waste heat than the baseline module. The ideal SBR, on the other hand, represents an upper limit for a spectrally-selective mirror. The perfect sub-bandgap reflection reduces parasitic absorption to the lowest value possible, and counteracts the effect of increased thermalization. Both the ideal ARC and ideal SBR have 6.9% optical benefits, however the ideal SBR has a thermal benefit of 0.68% (temperature reduction of 1.7 K) while the ideal ARC has a thermal benefit of -0.39% (temperature increase of 1 K); over 1% more energy is gained with perfect sub-bandgap reflection. Parasitic absorption is still not zero for the ideal SBR since, especially at wavelengths close to, but above, the bandgap the Si cell IQE is not perfect, meaning that some absorbed photons do not produce carriers which are eventually collected. Calculating the thermal benefit and therefore the total increase in energy yield requires including all waste heat pathways in **Figure 4.5**, since the antireflective aspect of the mirror affects the magnitude of the benefit achieved by the reflection.

4.5. Conclusion

This chapter discusses a time-independent matrix model to calculate the change in annual energy yield provided by a spectrally selective layer integrated into a solar module. The benefit of spectrally selective mirrors is primarily from increased transmission of current-generating photons. The thermal benefit from reduced operating temperature is expected to increase cell efficiency and extend module service life. The model accounts for both the direct and diffuse light present when operating outdoors at fixed-tilt, does not require time-dependent calculations, and computes in well under 1 second, a factor of 1000 faster than the full simulation. A 13-layer mirror and a 20-layer mirror were designed via optimization of the model result. The 13-layer design has increase annual energy yield by 3.6-3.8% compared to baseline. The 20-layer design has both lower reflection above the bandgap and higher sub-bandgap reflection than the 13-layer design, giving it higher optical and thermal benefits. The 20-layer design increases annual energy yield by 3.8-

4.0% compared to baseline. Comparison of the time-independent matrix model and finite-element simulation results demonstrates agreement within 0.1% absolute. Even though the model does not include weather effects beyond irradiance that are present in simulations, agreement with simulation is maintained even if the geographic location and tilt angle, and therefore the weather conditions, change. Furthermore, by accounting for the effects of antireflection and increased thermalization on total waste heat production, a detailed understanding of the thermal benefit is obtained. The variability of real weather conditions, in particular wind speed and the related convective heat transfer, does limit the accuracy in determining the exact energy benefit from lowering module operating temperature. However, it does not prevent the model from being used to design and optimize photonic structures for sub-bandgap reflection. With slight modification to model equations, designs could also be found at other module interfaces, including at the cell level, discussed in Chapter 7.

Chapter 5 Low-Complexity Mirror Designs

5.1. Introduction

Many of the photonic mirrors shown previously were optimized using a Bragg stack as an initial condition. As a result, these mirrors all possess strong sub-bandgap reflection bands and significant thermal benefits. However, the Bragg stack alone requires many layers to realize this reflection band, and the final mirror designs include additional layers inserted during optimization which primarily improve antireflection from 300-1200 nm, giving the mirrors an optical benefit. Furthermore, the main energy benefit of each mirror is optical as opposed to thermal. The antireflection is the greatest contribution to improving module energy output. In this chapter, the possibility of creating photonic mirrors with only a few layers is considered. These mirrors may not have strong sub-bandgap reflection, but do have excellent antireflection. Such designs sacrifice the sub-bandgap reflection for simplicity and cost of fabrication. Should the energy benefit be high enough, it could offset the cost of applying the mirror to the module, lowering the overall cost of producing energy.[131–133]

The mirrors in this chapter have as few as two layers, which limits the magnitude of reflection increase possible between sub-bandgap and visible wavelengths. Nonetheless, these mirrors are optimized to maximize module energy yield considering the full solar spectrum. They mainly act as "thermally-aware" anti-reflection coatings, offering improved anti-reflection over single-layer ARCs from 300-1200 nm, but with a small thermal benefit, thereby avoiding a thermal penalty that would arise without any increase in sub-bandgap reflection. The following chapter provides results and discussion of optimization of a series of mirrors with increasing complexity, showing the evolution of the design from providing primarily anti-reflection, to the addition of sub-bandgap reflection with a large enough layer count. Here, the goal is to determine the possible benefit of mirrors with a limited number of layers, and to find a balance between mirror complexity and the improvement it offers. However, as demonstrated even two-layer designs can increase module energy yield by up to ~0.8%, if low-index dielectrics are used in the design, without increasing operating temperature.

5.2. Mirror Benefit with Increasing Complexity

This section probes the trade-off between limiting complexity in spectrally-selective mirror designs and improving mirror performance both optically and thermally. Starting from a very simple design with just two layers, successive layer thickness optimization and needle insertion generates optimized mirrors designs with an increasing number of layers. While each stage is an improvement on the previous design, a point of diminishing returns exists where additional layers do not add significantly to the mirror total benefit. This series of mirrors is optimized with an objective function corresponding to the early version of the time-independent matrix model, shown in Chapter 3, and the energy yield improvements are determined with TOMCAT simulation as described in Chapter 2. Mirrors are compared as a function of their number of layers and the magnitude of their total benefit. One mirror determined to strike a balance between complexity and performance is simulated it using weather and irradiance conditions characteristic of dozens of locations across the continental United States to map how its performance changes over geographic location.

5.2.1 Successive Mirror Optimizations

Optimization began with an initial condition of a MgF_2 layer[134] on a SiO_2 layer on a glass substrate, with each layer having approximately quarter-wave optical thickness at 1600 nm. Repeated steps of layer thickness optimization followed by needle insertion were completed until sixteen different mirrors were designed, one for each layer thickness optimization step. The mirrors are numerically labelled according to the number of needle insertion steps that were performed to reach their layer structure. The first mirror is the optimized MgF_2/SiO_2 structure, labelled "0" since there are no needle insertion steps required to reach this structure. In total, 15 needle insertion steps were completed to give the sixteen different mirrors. Estimated benefits of optimized mirrors were tracked for each mirror, based on the early version of the time-independent matrix model, with the results shown in **Figure 5.1**. The layer count of each mirror is given in **Table 5.1**. While these mirrors represent optimal designs according to the early version of the model given the available library of materials, if different materials are used, then the designs will change and the resulting mirrors will differ.

Table 5.1: Layer Counts for Successively Optimized Mirrors

Mirror No.	**0**	**1**	**2**	**3**	**4**	**5**	**6**	**7**
No. of Layers	2	4	5	6	8	9	11	12
Mirror No.	**8**	**9**	**10**	**11**	**12**	**13**	**14**	**15**
No. of Layers	14	16	17	17	20	19	21	21

In general, needle insertion adds two layers to the mirror, one for the needle itself and one more because the needle splits a previously existing layer in two. However, after layer thickness optimization, some layers may end at near-zero thickness, thus sometimes only one layer is added to the mirror between optimization steps. Between steps 11 and 12, three layers are added, since a layer which earlier had near-zero thickness ended with appreciable thickness after step 12. Between steps 10 and 11 and steps 14 and 15, the layer count did not increase since two additional layers had near-zero thickness after optimization. These steps amount to a change in the materials or the material order of the mirror. Importantly, if needle insertion and layer thickness optimization are applied to mirror 15, the resulting mirror has the same materials in the same order, with only slightly different thicknesses and a very similar objective function value. Therefore, we chose not to continue needle insertion after mirror 15.

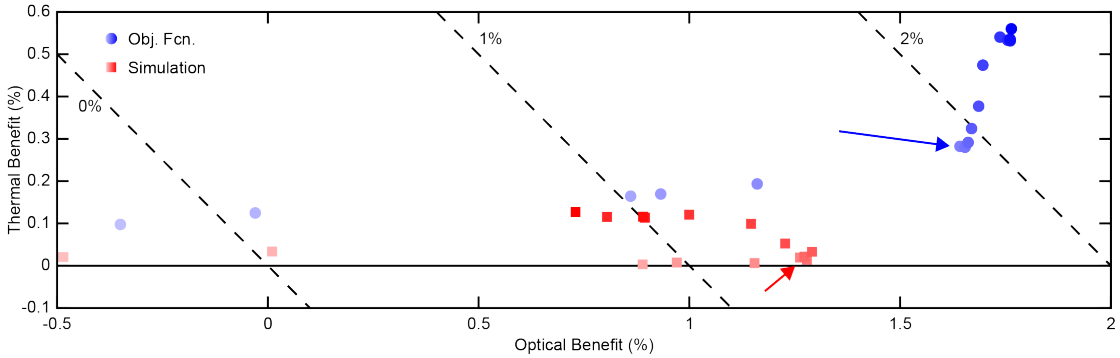

***Figure 5.1**: Objective function values (blue circles) and TOMCAT simulation results (red squares) of mirrors 0-15. The opacity of the color indicates the iteration number; deeper colors are later iterations. The total benefit is the sum of the thermal and optical benefits. Lines of equal total benefit are plotted as dotted lines. For both the objective function and simulations, results are percentage improvements over a module with the glass ARC. The arrows denote the 5th iteration of the mirror.*

Although the optimization is performed relative to a baseline solar module with uncoated front glass, the relative improvements in **Figure 5.1** are shown compared to a

module with a conventional glass ARC (99 nm porous SiO_2, index data given by Vogt[126]), as representative of what a multilayer mirror would likely replace on the front interface.

From the optimization objective function values in **Figure 5.1** (blue circles), all mirrors act primarily as antireflection coatings. However, only from mirror 6 onwards does the thermal benefit increase substantially, while the optical benefit stays mostly the same. We offer two reasons for this trend during optimization. The first is that, without using gradient index or moth-eye effects,[135] the double layer coating of mirror 0 cannot provide antireflection over the entire band from 300 – 1100 nm, while the four, five, six, eight, or nine layer structures of mirrors 1-5, respectively can increase the bandwidth of effective antireflection. Second, from previous simulations on ideal ARCs at the air/glass interface (see Chapter 3), a >7% optical benefit is possible if all light is transmitted, while only a slightly greater than 1% thermal benefit is possible if all sub-bandgap light is reflected. Furthermore, the optical penalty for increasing reflection above the bandgap is severe. Therefore, if a mirror is not sufficiently complex to offer spectral-selectivity, it is better that it be an antireflection coating versus a sub-bandgap reflector. Only a handful of layers, however, are required to achieve nearly the same optical benefit as much more complex designs.

5.2.2 Performance of Successively Optimized Mirrors

The performance of the same mirrors was then calculated using the opto-electro-thermal simulation method. Mirrors 0-15 were simulated using TMY data for Denver International Airport.[19] The module tilt angle was 20°. Simulation results are shown as red squares in **Figure 5.1** and, like the objective function values, are shown as percentage improvements compared to a module with a conventional glass ARC.

The early version of the time-independent matrix model used here assumes that all light transmitted above the bandgap through the interface at which the mirror is placed reaches the cell and is absorbed in the cell, and that all transmitted sub-bandgap light is absorbed parasitically. These assumptions neglect the presence of other layers and interfaces in the module, and in particular ignore the possibilities of absorption in the encapsulant, and escape of sub-bandgap light from the module without absorption. Furthermore, with increased module current, more heat is generated via electronic losses,

which is not accounted for in the early model version. The effect of these is that the simulations of mirrors are consistently less beneficial thermally than predicted by the objective function.

Table 5.2: Details of Mirror 5

Layer No.	Material	Thickness (nm)
1	MgF_2	117.8
2	ZrO_2	20.8
3	Al_2O_3	23.2
4	ZrO_2	116.9
5	Al_2O_3	20.3
6	SiN_x	37.9
7	SiO_2	41.8
8	SiN_x	12.0
9	SiO_2	207.1

The optical model predictions and optical simulation result do not closely agree starting at mirror 5 and continuing to mirror 15. The more complex mirrors all have 4% expected optical improvement, while they simulated at no better than ~3.6% optical improvement. The discrepancy arises due to the more complex mirrors reducing reflection in the region <360 nm. While according to the early version of the objective function this increases the optical benefit, the glass and encapsulant used in the module simulations does not transmit any of this light to the cell. Therefore, in the simulation, mirror transmission <350 nm is not beneficial. The time-independent matrix model as described in Chapter 2 considers absorption in all module layers, and waste heat intrinsic to carrier extraction, both crucial to model accuracy.

Despite the over-prediction of the benefit when optimizing these mirrors, all mirrors except mirror 0 have a higher optical and thermal benefit than the conventional glass ARC. These mirrors therefore allow their modules to produce more power and operate at lower temperatures than a module with a conventional ARC. Based on these results, mirror 5 was designated as the best overall mirror in terms of achieving the highest total benefit with a relatively small number of layers in the structure. **Table 5.2** shows the materials and layer thicknesses of mirror 5; layer 1 is adjacent to air and layer 9 is adjacent to the cover glass. The net reflection of mirror 5 with respect to glass coated with a single-layer ARC is given

in **Figure 5.2**. Blue colors correspond to wavelengths and angles of incidence where the mirror is antireflective, red colors correspond to regions where reflection is increased. As shown, the mirror is almost entirely antireflective in the region 300 – 1100 nm, except at low angles and wavelengths near 300 nm, and at high angles near 1100 nm. The mirror exhibits the required spectral selectivity at all angles of incidence. Since these mirrors are not based on Bragg-stack designs, they do not possess a well-defined reflection band with a sharp turn-on between transmission and reflection. A Bragg-stack-like design would have greater reflection in the sub-bandgap region, especially at shorter wavelengths where there is more incident spectral power. But, such a design would require dozens of layers, and may not be simple to fabricate.

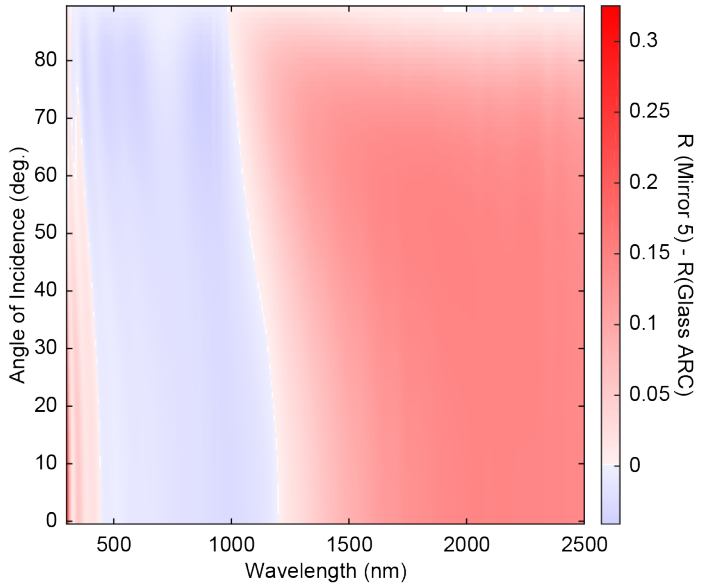

***Figure 5.2**: Net reflection of mirror 5 versus wavelength and angle of incidence, compared to the air/glass ARC interface. Blue shades indicate that mirror 5 reflects less light than the bare air/glass ARC interface for a given wavelength and angle of incidence; red shades indicate that mirror 5 reflects more light than the air/glass ARC interface.*

5.2.3 Simulations Across the Continental United States

Additional TOMCAT simulations of both mirror 5 and the glass ARC were performed at 47 additional locations over the continental United States. The module tilt at all locations was 20 degrees. Results are given in **Figure 5.3** in two different forms. In the top panel, the plot displays the relative increase in energy produced by the module with

mirror 5 compared to the module with the glass ARC. In the bottom panel, the plot shows the irradiance-weighted, time-averaged temperature difference between the modules.

Regardless of the location, the module with mirror 5 produces between 1.24% and 1.32% more energy than the one with the conventional glass ARC. Despite differences in irradiance, solar position, and the fraction of diffuse light compared to direct, the relative performance of the module does not exhibit significant variation, less than 0.1% absolute. **Figure 5.3** shows that the cloudy, high-latitude areas generally show better relative performance for mirror 5, while sunny, low-latitude areas show worse relative performance. The major factor affecting optical module performance as geographic location changes is changing angle- of-incidence distribution, which, in turn, is affected by the module tilt and the amount of diffuse light. The lower the module tilt as compared to the latitude and the greater the fraction of diffuse light, the greater the fraction of sunlight incident between 40-60 degrees away from normal incidence (see section 3.4). At these angles, these mirrors typically have better antireflection and closer alignment of the reflection turn-on with the bandgap, as can be seen for mirror 5 in **Figure 5.2**. The result is slightly higher overall performance compared to a location where more light is incident at near-normal incidence. It must be emphasized that this trend holds only for mirrors designed to operate at all angles of incidence. As seen in Section 3.4 mirrors designed to work at near normal incidence may not perform as well under more oblique angle radiation.

In terms of irradiance-weighted temperature difference, the module with mirror 5 operated at between 0.03°C and 0.06°C colder than the module with the conventional glass ARC. This is a small decrease, but notable given that the module with mirror 5 simultaneously produced ~1.28% more power. If the 1.28% power increase came without any thermal management, we expect that the module temperature would increase by ~0.29°C. One expects that in high irradiance areas, the temperature difference would rise, while in low irradiance areas the temperature difference would fall. This trend which is borne out in **Figure 5.3**, and illustrates the importance of spectrally selective sub-bandgap reflectors for solar module performance in high-irradiance areas.

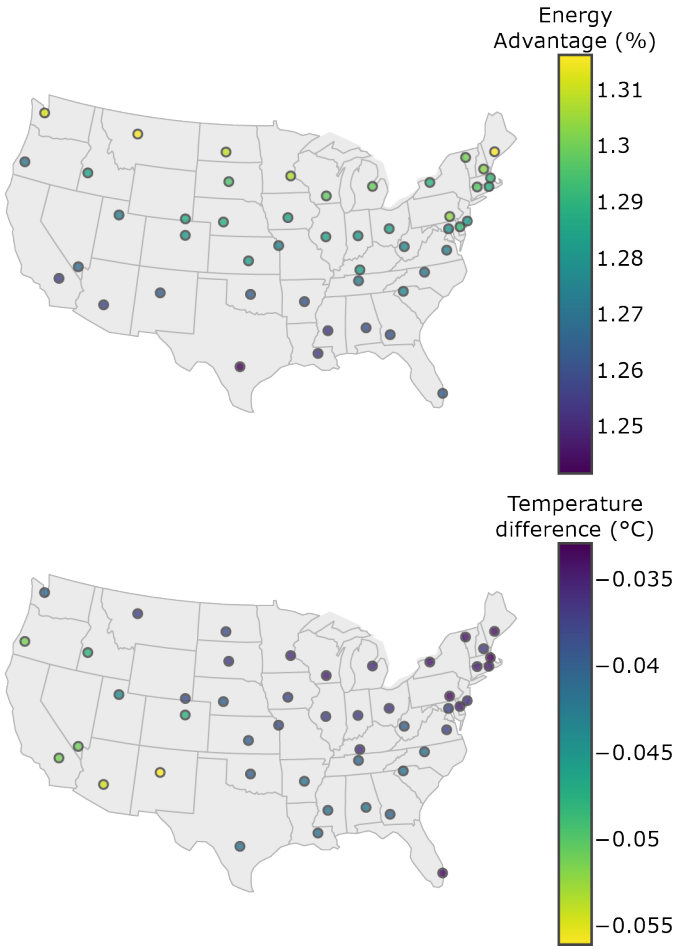

***Figure 5.3**: (Top) Plot of relative increase in energy output for a module with mirror 5 compared to a module with a conventional glass ARC. (Bottom) Plot of irradiance weighted temperature difference between a module with mirror 5 and a module with a conventional glass ARC. Each dot represents a full-year simulation at that location.*

5.3. Two-Layer Designs

In the previous section, it was shown that with a high enough layer count, a spectrally-selective mirror could replace a single-layer glass ARC while also providing sub-bandgap reflection. Simpler designs improved on the single-layer glass ARC and limited the module temperature increase with the sub-bandgap reflection they could provide. In this section, two-layer glass coatings are considered, the simplest possible design while still allowing spectral selectivity. Certainly, two-layer designs fall into the category of "thermally-aware" anti-reflection coatings, and are useful in their capacity to increase module energy yield without increasing module temperature. These designs would

be the easiest and cheapest to fabricate, and the following discusses the possible energy yield increases.

5.3.1 Optimized Two-Layer Designs

The dielectrics MgF_2, TiO_2, SiO_2, SiN_x, and Al_2O_3 were each candidates for use in a two-layer design. All possible two-material combinations were optimized via the early version of the time-independent matrix model described in Chapter 3. The initial condition for optimization was that each layer had an optical thickness of ~400 nm. However, for any choice of materials, there is a local minimum in the model result where all layer thicknesses are set to zero (i.e. there is no mirror). Since the primary benefit offered by a two-layer design is anti-reflection of light in the range 300 – 1200 nm, one of the two layers should have an index between that of air (n=1) and that of the module cover glass. Only two materials, MgF_2 and SiO_2 satisfy this requirement. Therefore, the best design for mirrors that did not include either of these materials was the zero-thickness case. Results for mirrors that do not include MgF_2 or SiO_2 are not presented here. Additionally, if the first layer (adjacent to air) of the two-layer structure is not the lower index material (MgF_2 or SiO_2), then the best design has the first layer thickness set to zero, giving a single-layer structure. For completeness, results are shown for the optimum thickness of MgF_2 and SiO_2 in single-layer structures.

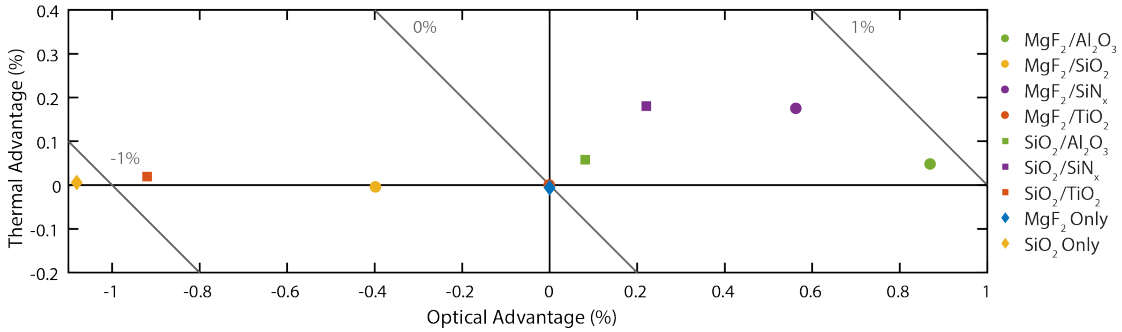

***Figure 5.4**: Objective function values for the optimized mirrors relative to a module with a 99 nm glass ARC. Circles correspond to the mirrors with a top layer of MgF_2, squares correspond to the mirrors with a top layer of SiO_2, and diamonds correspond to single-layer structures. All points are color-coded according to the material in the bottom layer. Grey lines mark contours of equal total advantage.*

All optimized mirrors that provide an energy yield increase compared to the no-mirror case have their optimized model results reported in **Figure 5.4**. These values are

reported as increases over a module with a single-layer glass ARC, which is itself an improvement over the no-mirror case. Mirrors are designated by their materials, with the first material corresponding to the top layer and the second to the bottom layer, so the SiO_2/TiO_2 mirror has SiO_2 as the layer adjacent to air while TiO_2 is adjacent to glass. The SiO_2/MgF_2 mirror has an optimum design which is a single-layer of MgF_2, so its model result is not plotted in favor of the single-layer MgF_2 structure. **Table 5.3** gives the layer optimized layer thicknesses for each mirror in **Figure 5.4**.

Table 5.3: Two-Layer Mirror Designs

Mirror	Layer Thicknesses (nm)		Mirror	Layer Thicknesses (nm)	
	Top	Bottom		Top	Bottom
MgF_2/Al_2O_3	128.9	200.9	SiO_2/Al_2O_3	121.9	192.3
MgF_2/SiO_2	131.4	379.6	SiO_2/SiN_x	119.4	176.0
MgF_2/SiN_x	126.6	180.5	SiO_2/TiO_2	153.5	4.6
MgF_2/TiO_2	150.2	3.2	SiO_2 Only	-	117.4
MgF_2 Only	-	127.5	-	-	-

Every mirror except the single-layer SiO_2, the SiO_2/TiO_2, and the MgF_2/SiO_2 structure is the same as or better than the single-layer glass ARC according to the optimization model. The improvement that the two-layer structures offer over the glass ARC is mostly optical. The single layer of MgF_2 provides the same improvement as the glass ARC (within <0.01%), despite having a higher refractive index than the glass ARC material. Typically, a material with an index closer to $\sqrt{n_1 n_2}$, where n_1 and n_2 are the indices of the superstrate and substrate, will reduce reflection the most with only a single layer. Therefore, since the index of MgF_2 is lower than that of SiO_2 and higher than that of the glass ARC, we expect the single layer of MgF_2 to provide more benefit than the single layer of SiO_2 and less benefit than the glass ARC. However, despite the glass ARC having an index closer to $\sqrt{n_1 n_2}$, both it and the single layer of MgF_2 have the same energy yield improvement because the 99 nm thickness of the glass ARC is not optimized according to our method, and is instead taken from Vogt.[126]

5.3.2 Characterization of Two-Layer Mirrors

As discussed in the previous section, the early version of time-independent matrix model is a rough estimate of module performance with a given mirror on the front glass. A better estimate is obtained via the full-year opto-electro-thermal simulations. We take all mirrors with objective function values better than the glass ARC and simulate them, using TMY3 data corresponding to Denver, CO at a fixed tilt of 20 degrees.[19] The results for each mirror are shown in **Figure 5.5**.

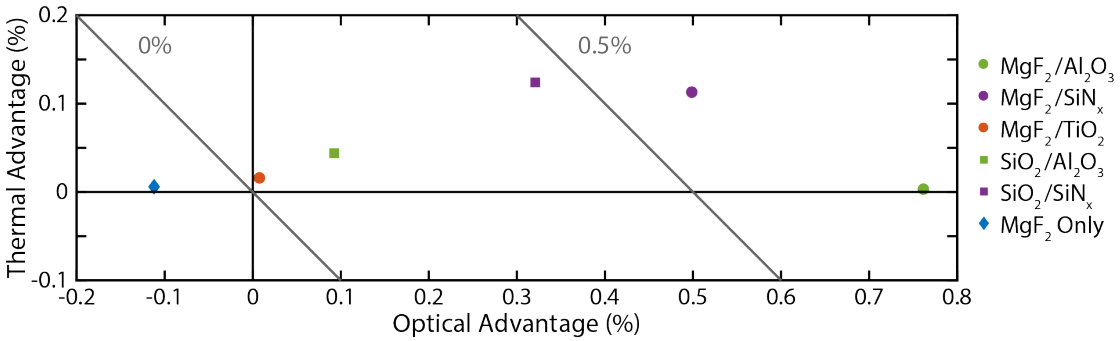

***Figure 5.5**: Simulation results for optimized mirrors relative to a module with a 99 nm glass ARC. Circles correspond to the mirrors with a top layer of MgF_2, squares correspond to the mirrors with a top layer of SiO_2, and diamonds correspond to single-layer structures. All points are color-coded according to the material in the bottom layer. Grey lines mark contours of equal total advantage.*

In general, mirrors with MgF_2 as the top layer outperform their counterparts with SiO_2 on top instead. This is expected since the lower refractive index of MgF_2 compared to SiO_2 results in lower Fresnel reflection across all wavelengths at the air/MgF_2 interface compared to an air/SiO_2 interface, allowing more light into the thin film layers and ultimately into the module. The best performing mirror, a structure of MgF_2 on Al_2O_3 gives almost no thermal benefit but gives an ~0.8% optical benefit compared to the glass ARC. The highest thermal benefit offered comes from the SiO_2/SiN_x mirror at 0.1%, but the MgF_2/SiN_x mirror is nearly as good thermally and offers a higher optical benefit as well. This thermal benefit, given the temperature coefficient of 0.39%/K, corresponds to an operating temperature reduction of ~0.29K on average over the year compared to a module with the glass ARC.

To further investigate the performance of the best two mirrors (MgF_2/Al_2O_3 and MgF_2/SiN_x), we plot their net reflection compared to the glass ARC versus wavelength and

angle in **Figures 5.6a-b**. Both mirrors offer reduced reflection over most of the range from 300 – 1200 nm, but fail at short wavelengths from 300 nm to ~500 nm. The failure is likely because, with only two layers, the bandwidth of the high transmission region is limited. As seen in Chapter 3 and Chapter 4, structures with one to three dozen layers reduced reflection over a wider range within 300 – 1200 nm. Both mirrors also reflect more light in the sub-bandgap region than glass ARC. The MgF_2/SiN_x mirror in **Figure 5.6b** has more reflectivity in the sub-bandgap region than does the MgF_2/Al_2O_3 mirror in **Figure 5.6a**, given by the deeper red colors. The additional sub-bandgap reflection of the MgF_2/SiN_x mirror is the primary reason for its larger thermal benefit.

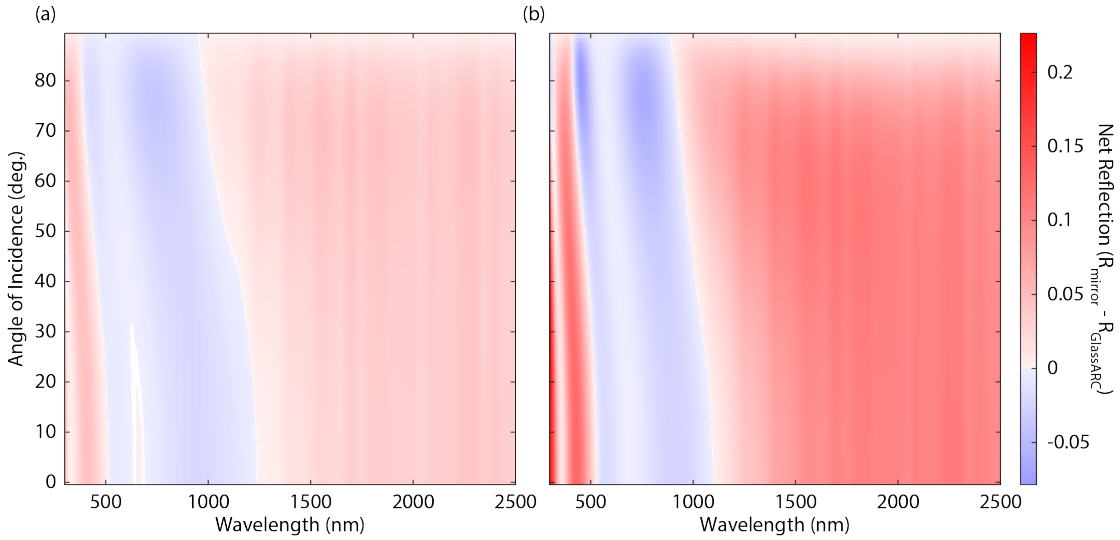

***Figure 5.6**: Net reflection for (a) the MgF_2/Al_2O_3 mirror and (b) the MgF_2/SiN_x mirror. Blue shades correspond to regions where the mirror reflects less light than the glass ARC; red shades corresponds to regions where the mirror reflects more than the glass ARC.*

Examining **Figure 5.6** versus angle of incidence, one notices that at every angle the reflection increase begins at longer wavelengths for the MgF_2 mirror than for the MgF_2/SiN_x mirror. For any mirror design, reflection in the part of the spectrum just higher than the bandgap energy should be avoided, as the current penalty for reflecting useful light is severe. Therefore, in the optimized designs of both the MgF_2/Al_2O_3 mirror and the MgF_2/SiN_x mirror, the low-angle sub-bandgap reflection begins around 1200 nm, so that at more oblique angles only a small amount of useful light is reflected at wavelengths shorter than 1200 nm. The MgF_2/SiN_x mirror, while it reflects more sub-bandgap light in

general, also reflects more useful light at oblique angles near 1200 nm than does the MgF_2/Al_2O_3 mirror, which reduces its optical benefit in comparison.

As discussed in the previous section, the early version of the time-independent matrix model tends to overestimate the thermal benefit of a given mirror. The objective function is a preliminary estimate of the performance of the mirror and does not take into account effect such as the additional electronic losses caused by transmitting more light to the cell, which would tend to heat the module and reduce the thermal benefit. The MgF_2/Al_2O_3 mirror does increase sub-bandgap reflection compared to the glass ARC, but TOMCAT simulation indicates no thermal benefit since the reduction in parasitic absorption is cancelled by the increase in heat due to the additional current from the optical benefit.

5.4. Conclusion

Low-complexity spectrally-selective mirror designs can be effective for module energy yield improvement. They take advantage of the large optical benefit available for mirrors applied to glass, and compensate for the operating temperature increase inherent to anti-reflection coatings with modest sub-bandgap reflection. For the particular series of mirrors optimized here, about nine layers were required before the mirror was able to provide a thermal benefit, indicating a transition between mirrors that act as improved anti-reflection coatings, and mirrors that have significant sub-bandgap reflection. For mirrors with such few layers, a sharp contrast between reflection in two bands above and below the bandgap wavelength is impossible, so optimization following even the early version of the model used here focuses on anti-reflection. While not every two-layer mirror can decrease reflection compared to a single-layer glass ARC, some can with the right choice of materials. In the general case, only a handful of layers are required for significantly improved anti-reflection compared to a single-layer ARC, as we shall see in the next chapter with a four-layer design.

However, the necessity of considering all module layers when optimizing mirror design has also been shown in this chapter. The energy yield increase was overestimated in both the optical and thermal components for most mirror designs. The simpler optimization model used in this chapter fails to account for absorption in glass and encapsulant, waste heat generated during carrier collection, and imperfect sub-bandgap

absorption in the cell. As shown in Chapter 4, optimization considering the mirror impact on the entire module, not just the glass interface, is required for agreement with full multi-physics simulation results.

While low-complexity designs are not as beneficial thermally as designs based on Bragg stacks, they are promising for practical application. The low layer count lends itself to easy fabrication and opens up the possibility of reducing the cost of electricity produced by the module. In the next chapter, two such mirrors are fabricated and tested to demonstrate the effect of spectrally-selective reflection.

Chapter 6 Fabrication and Outdoor Testing of Spectrally-Selective Mirrors Integrated into Photovoltaic Modules

6.1. Introduction

Outdoor testing of photovoltaic modules provides data under realistic field conditions over both the short term (e.g. hour-by-hour or day-to-day energy production) and long term (e.g. seasonal variation in power output or module degradation over months or years). Standard test conditions[136] of one-sun irradiance, normal incidence, and 25° C operating temperature are not typically achieved outdoors,[137] making field testing the best method of validating photovoltaic module performance models.[138–142] Discussion in this work until now has focused on simulation and modeling of c-Si photovoltaic modules installed outdoors, and optimizing the design of spectrally-selective mirrors based on these models. In this chapter, spectrally-selective mirrors are integrated into photovoltaic modules to increase power output and reduce operating temperature. The wavelength-dependent refractive indices of the dielectric materials available for mirror design are determined and integrated into the calculations of the time-independent matrix model. Two mirrors, one with four layers representing a cost-effective design, and one with twelve layers designed to have high thermal benefit, are fabricated and integrated into test modules. Reflection measurements of fabricated mirrors confirm spectrally-selective reflection. Each module is installed at the NREL Outdoor Test Facility and compared against a baseline module without a mirror and a module with a single-layer glass ARC. Analysis of the test results is similar to analysis of TOMCAT results described in Section 2.2.3. The predictions of the time-independent matrix model are compared against the results of the outdoor test.

6.2. Thin-Film Refractive Indices

The reflection spectrum of a stack of thin films, including any of the spectrally-selective mirrors discussed in this work, is strongly dependent on the refractive index of

each thin-film material.[112] Agreement between mirror reflection predicted by the time-independent matrix model and experimentally measured reflection requires that the material properties assumed in the model accurately reflect reality. Therefore, the refractive indices of several dielectrics used for mirror design were determined experimentally for the purpose of importing the results into the time-independent matrix model. These materials included SiO_2, SiN_x, Al_2O_3, TiO_2, and ZrO_2. The refractive indices determined by this experiment were used not only to design mirrors for fabrication, but to design all mirrors in this work.

Thin films of each of these materials were prepared on cleaned single-side polished Si substrates, one film per substrate. All deposition was carried out at the Minnesota Nano Center cleanroom facility. Films of SiO_2 and SiN_x were deposited by plasma-enhanced chemical vapor deposition (PECVD). For SiO_2, precursor gases were 200 sccm 2% SiH_4/98% He and 450 sccm N_2O and the deposition temperature was 250 °C. For SiN_x, precursor gases were 200 sccm 2% SiH_4/98% He, 740 sccm N_2, and 2.0 sccm NH_3 and the deposition temperature was 340 °C. For both SiO_2 and SiN_x, RF power was 20 W and the total chamber pressure was 900 mTorr. Al_2O_3 and ZrO_2 were deposited by atomic layer deposition (ALD). For Al_2O_3, precursors were trimethylaluminum and water vapor, and the deposition temperature was 180°C. For ZrO_2, precursors were tetrakis-(dimethylamino)zirconium and water vapor, and the deposition temperature was 250°C. TiO_2 was sputtered from a target of the same material. Sputtering occurred at a RF power of 250 W in a chamber of 5 mTorr of Ar. The substrate sat on a plate which rotated during sputtering.

The refractive index of each material is determined using spectroscopic ellipsometry. A full description of the theory behind ellipsometry is beyond the scope of this work, however detailed information may be found elsewhere.[143,144] Briefly, the optical properties of a material are determined from the amplitude and polarization of reflected light. Measurements are typically cast in terms of two angles, Ψ and Δ. As shown in eq. 6.1, $\tan\Psi$ is the ratio of the amplitudes of reflection under *s*- and *p*-polarized light, and Δ is the phase difference. The angles Ψ and Δ are functions of the incident wavelength, the thicknesses of any films that contribute to reflection, their refractive indices, and the refractive index of the substrate. With just one film present, and known substrate refractive

index, the refractive index of the thin film (and its thickness) can be determined from this measurement. With Ψ and Δ measurements made over a range of wavelengths, the refractive index can be found over that same range.

$$\frac{r_s}{r_p} = \tan\Psi \cdot exp(i\Delta) \tag{6.1}$$

Spectroscopic ellipsometry was performed using a JA Woolam Vase Ellipsometer on thin films of Al_2O_3 SiO_2, SiN_x, TiO_2, and ZrO_2. Measurements were taken at angles of 65°, 70°, and 75° and at wavelengths 300 – 1100 nm at 20 nm intervals (10 nm intervals for TiO_2). The refractive index of each thin film is determined first by assuming its functional form versus wavelength or frequency, and then fitting constants in that functional form to reproduce experimental measurements. For SiO_2, SiN_x, Al_2O_3, and ZrO_2, the real part of the refractive index is fit to Cauchy's equation (eq. 6.2), where A, B, and C are fitting parameters.[145] This equation is not consistent with Kramers-Kronig relations,[98] but is a good approximation when there are no resonant absorption peaks (due to e.g. an electronic transition) near the wavelengths considered.

$$n(\lambda) = A + \frac{B}{\lambda^2} + \frac{C}{\lambda^4} \tag{6.2}$$

The Cauchy equation assumes no absorption or light, so the refractive index is purely real. However, for ZrO_2, better agreement to ellipsometric measurements was obtained by including an Urbach absorption tail[146] following eq. 6.3, where α is the absorption coefficient (cm^{-1}), h is the Planck constant, ν is the frequency, and A, g, and ν_0 are fitting parameters corresponding to the strength of absorption, absorption bandwidth, and absorption edge, respectively. The absorption coefficient contributes only to the imaginary part of the refractive index, and its combination with the Cauchy equation is not Kramers-Kronig consistent.

$$\alpha(\nu) = Aexp\big(g(h\nu - h\nu_0)\big) \tag{6.3}$$

For TiO_2, the above models are inadequate due to absorption of near-UV light.[147,148] To model the refractive index of TiO_2, the imaginary part of the *permittivity*, ε_2, takes a

Gaussian form (eq. 6.4). The fitting parameters are the center photon energy, E_c, the amplitude A, and the width σ.

$$\varepsilon_2(E) = A\, exp\left(-\left(\frac{E-E_c}{\sigma}\right)^2\right) - A\, exp\left(-\left(\frac{E+E_c}{\sigma}\right)^2\right) \tag{6.4}$$

The real permittivity ε_1 is found by the Kramers-Kronig relation,[98] and includes contribution from pole terms, valid when the pole energies E_p are outside of the fitting range, and a high-frequency offset, ε_∞.[149]

$$\varepsilon_1(E) = \varepsilon_\infty + \frac{2}{\pi} P \int_0^\infty \frac{s\varepsilon_2(s)}{s^2-E^2}\, ds + \sum_n \frac{B_n}{E_{p,n}^2 - E^2} \tag{6.5}$$

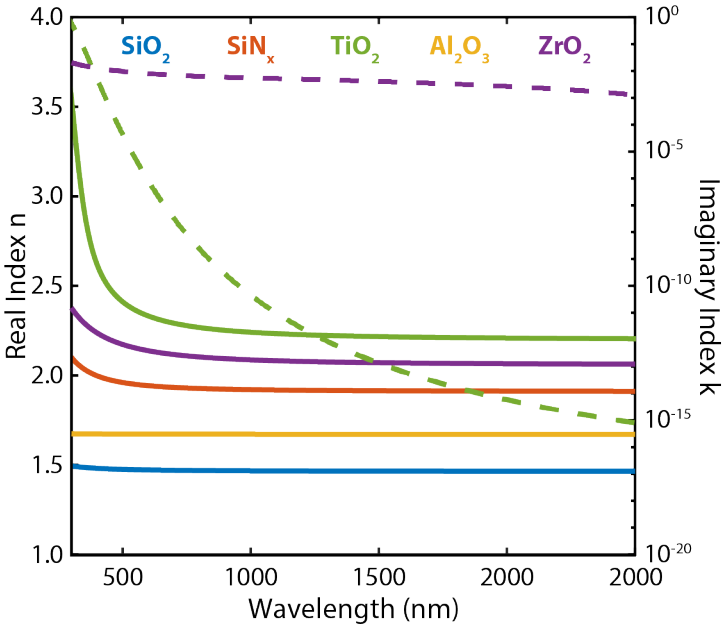

***Figure 6.1**: Real (solid lines) and imaginary (dashed lines) refractive indices for SiO_2, SiN_x, TiO_2, Al_2O_3, and ZrO_2. The refractive indices were determined by spectroscopic ellipsometry on thin-film samples deposited on polished Si. The indices are based on measurement from 300-1100 nm, and fits are shown extended to 2500 nm.*

The refractive indices of SiO_2, SiN_x, Al_2O_3, TiO_2, and ZrO_2 are given in **Figure 6.1**. Ellipsometric measurements were made over the range 300-1100 nm. However, modeling requires data until 2500 nm. The fitting parameters found for each material were used to extrapolate the refractive index between 1100 and 2500 nm. While these refractive index models may not be valid in the extrapolated region, the largest deviations between the extrapolated index and the actual index occur at the longest wavelengths. Since model

results are weighted by the AM1.5G spectrum, where longer wavelengths tend to have less spectral power, and since direct measurement of the refractive index was unavailable beyond 1100 nm, errors introduced by the extrapolation were deemed acceptable.

6.3. Fabrication and Characterization of Spectrally-Selective Mirrors

6.3.1 Design and Layer Deposition

Two thin-film mirrors were designed using the time-independent matrix model as described in Chapter 2. One mirror had four layers, and another had twelve. The optimization assumed that the mirror would be mounted in Denver, CO at a 20° tilt angle facing due south. The initial condition for optimization for the four-layer mirror was one layer of SiO_2 on top of a layer of SiN_x, both with 100 nm thickness. The initial condition for optimization of the twelve-layer mirror was a five-layer stack of alternating layers of SiO_2 and TiO_2 each with 400 nm optical thickness. Final mirror designs included only the materials SiO_2, SiN_x, and TiO_2. Mirrors were fabricated on 6 in. x 6 in. low-iron float glass with a thickness of 3.2 mm. Neither side of the glass was textured.

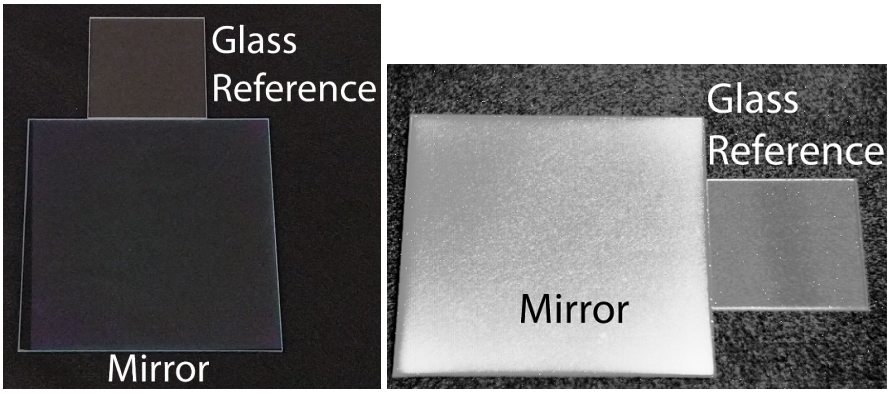

***Figure 6.2**: Photographs of the fabricated twelve-layer mirror in the (left) visible spectrum and (right) short-wave infrared spectrum compared to a bare glass reference.*

Each material was deposited as described in the previous section. During deposition, an additional piece of polished Si was included adjacent to the glass as a witness. Ellipsometric measurements on the witness gave the deposited thickness, and it was assumed that the thickness deposited on the glass was the same. Deposition on witness Si substrates was not possible for TiO_2, as the chamber was too small to hold both the glass and the witness slide. **Table 6.1** and **6.2** give the design of the four-layer and twelve-layer

mirrors and the realized layer thicknesses from witness Si substrates, respectively. **Figure 6.2** shows photographs in the visible and short-wave infrared taken of the fabricated twelve-layer mirror compared to a bare glass reference. In the infrared, the mirror is much more reflective than the glass, while in the visible it is not.

Table 6.1: Four-layer Mirror Design and Fabrication Thicknesses

Material	Design Thickness (nm)	Deposited Thickness (nm)
SiO_2	104.7	107.1
SiN_x	49.3	49.4
TiO_2	99.3	-
SiN_x	74.9	71.0

Table 6.2: Twelve-layer Mirror Design and Fabrication Thicknesses

Material	Design Thickness (nm)	Deposited Thickness (nm)
SiO_2	116.0	108.8
TiO_2	24.2	-
SiO_2	11.6	11.4
TiO_2	100.5	-
SiO_2	27.5	25.5
TiO_2	18.8	-
SiO_2	218.2	219.2
SiN_x	70.0	69.6
TiO_2	114.8	-
SiO_2	21.5	22.8
SiN_x	44.2	45.5
SiO_2	229.8	236.3

6.3.2 Reflection and Transmission Measurements

Specular reflection and transmission measurements were made on finished mirrors and bare glass samples using a Cary 7000 UV-VIS-NIR spectrophotometer with a Universal Measurement Accessory (UMA) attachment. Measurements were taken at wavelengths between 300 nm and 2500 nm at 1 nm intervals, and at angles of 6° to 84° at 3° intervals. A baseline 100% scan was performed with no sample in the beam path. A baseline 0% scan was performed with the beam blocked from reaching the detector. Measurements of diffuse reflectance and transmission of both bare glass and mirrors fabricated on glass were performed from 300 nm to 2500 nm with light incident at 3°20'.

Diffuse reflectance and transmittance was indistinguishable from the instrument noise floor for both the bare glass and fabricated mirrors. Therefore, measurements of specular reflection fully describe the mirror. These reflectance results will be discussed in the next section alongside the outdoor test results.

6.4. Module Lamination and Outdoor Testing

6.4.1 Module Lamination and Installation

Single-cell modules were fabricated using glass from each of the mirrors, a bare glass piece, and glass coated with a commercial PV ARC, for a total of four modules. The module fabricated with bare glass is referred to as the baseline module throughout this work. The modules each utilized a single five-inch, two-bus-bar polycrystalline Si cell with approximately 14% efficiency. The cells used in this test were within 0.4% relative efficiency of one another. Cells were encapsulated behind the glass using UV-absorbing EVA with nominal 0.4 mm thickness. An additional layer of EVA was placed on the cell back along with a poly-vinyl-fluoride-based backsheet. Lamination was performed with a vacuum laminator at 145°C in accordance with the recommendations of the EVA manufacturer. A thermocouple was included between the cell and backside EVA to allow for cell temperature measurements. All cells had an area of 159.4 cm^2 ± 0.1%, therefore we directly compare the currents measured from each module.

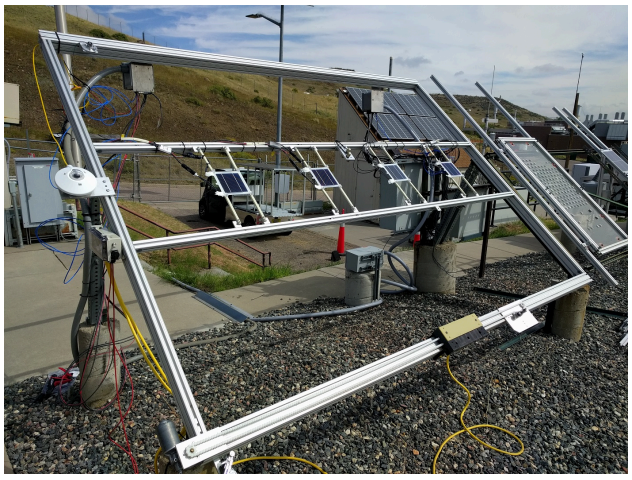

***Figure 6.3**: All four test modules as installed outdoors at NREL.*

All modules were mounted at the National Renewable Energy Laboratory (NREL, 39.744 °N, 105.151 °W) at a 40° tilt angle facing south (see **Figure 6.3**). Modules were mounted using fiberglass composite supports to avoid conduction to the rack. I-V curves were measured from each module automatically every five minutes. Cell temperature, ambient temperature, and broadband plane-of-array irradiance measurements were collected with each I-V curve. Data were recorded beginning at sunrise on Sep. 7, 2018 and ending at sunset on Oct. 4, 2018; no data were taken overnight.

6.4.2 Data Analysis

The maximum power of each module was determined using the I-V curves as the largest product of an I,V-pair on the curve. The maximum power determined from I-V curves was used for comparison of one module to another. Optical and thermal benefits were determined from the maximum power and cell temperature of each module compared to the baseline module. The thermal benefit was determined by first calculating the output-power-weighted average temperature difference, ΔT_{avg}, between a test module and the baseline, as shown in eq. 6.6.

$$\Delta T_{avg} = \frac{\sum_t P_{baseline}(t) \cdot (T_{baseline,cell}(t) - T_{cell}(t))}{\sum_t P_{baseline}(t)} \tag{6.6}$$

In (1), $P_{baseline}$ is the baseline maximum power at time t, $T_{baseline,cell}$ is the baseline cell temperature and T_{cell} is the cell temperature of the module being analyzed. The thermal benefit, $B_{thermal}$ is the weighted average temperature difference multiplied by the temperature coefficient of cell efficiency, β, as shown in eq. 6.7.

$$B_{thermal} = \Delta T_{avg} \cdot \beta \tag{6.7}$$

The optical benefit, $B_{optical}$, of a module was determined by comparison of its maximum power, P_{cell}, with that of the baseline module and subtracting the portion of the power difference due to thermal benefit, as shown in eq. 6.8. Total benefit, B_{total}, is shown in eq. 6.9.

$$B_{optical} = \left(\frac{\sum_t P_{cell}(t)}{\sum_t P_{baseline}(t)} - 1\right) - B_{thermal} \tag{6.8}$$

$$B_{total} = \left(\frac{\sum_t P_{cell}(t)}{\sum_t P_{baseline}(t)} - 1\right) \quad (6.9)$$

Optical and thermal benefits were determined using β equal to -0.39%/K.

6.4.3 Comparison of Time-Independent Model and Outdoor Test

During optimization of the mirror designs, the time-independent model assumed irradiance conditions typical for a module installed at 20° tilt in Denver, CO. However, to compare the model's predictions to the outdoor test results, the measured irradiance must be used in the model. As described in Section 2.2.2, the required data is the irradiance as a function of angle of incidence on the tilted module. Plane-of-array irradiance was recorded during the test, however this was not enough information alone to determine the distribution of that irradiance versus angle. Instead, DHI and DNI were taken from the NREL Solar Radiation Research Laboratory (SRRL) Baseline Measurement System (BMS)[18] over the time interval corresponding to the outdoor test. The NREL SRRL BMS is very close to the location of the outdoor test, so the curve of irradiance versus angle of incidence extracted from SRRL BMS data should match that experienced by module during the outdoor test closely. The DHI and DNI data were used to calculate irradiance as a function of angle of incidence as described in Section 2.2.2.

6.4.4 Outdoor Test Results

The total, optical, and thermal benefits for the modules coated with the standard ARC, four-layer mirror, and twelve-layer mirror were calculated with the results shown in **Table 6.3**. The modules including both mirrors operated on average cooler than the baseline module, with the module containing the twelve-layer mirror operating 1.5 K cooler than baseline. However, neither mirror caused its module to produce more power than the baseline module, instead suffering penalties of 6.1% for the four-layer mirror and 4.8% for the twelve-layer mirror. The module with the ordinary ARC produced 1.2% more power than baseline, however it also operated 0.49 K hotter due to the waste heat generated from the additional light transmitted to the cell.

Figure 6.4 shows the measured reflection and transmission spectra, compared to a bare piece of glass, for both the four-layer and twelve-layer mirrors. **Figures 6.4a** and **c**

show the difference in experimental reflection measurements between the spectrally-selective mirror on glass and bare glass. The twelve-layer mirror exhibits significantly more reflection below the bandgap, which is consistent with the reduced operating temperature observed experimentally.

Table 6.3: Energy Yield Benefits of Modules Installed Outdoors

Module	B_{total}	$B_{optical}$	$B_{thermal}$	ΔT_{avg}
Standard ARC	1.2%	1.4%	-0.19%	-0.49K
Four-Layer	-6.1%	-6.1%	0.06%	0.16K
Twelve-Layer	-4.8%	-5.4%	0.58%	1.5K

One possible reason for the decreased performance in the modules with mirrors is increased reflection of above-bandgap light, preventing this light from reaching the cell. However, in the spectral range from 300 – 1200 nm, both mirrors exhibit decreased reflection of useful light (shaded blue on the figures). Therefore, the decreased performance is not the result of too much reflection above the bandgap, and the mirror reflection is functioning as designed.

Figures 6.4b and **d** show differences in measured transmission of the four-layer and twelve-layer mirrors, respectively, compared to bare glass. These figures reveal that neither mirror increases transmission of above bandgap light, especially at near-normal angles of incidence. For most wavelengths 300-1100 nm, and at angles of less than ~30°, the transmission is lower for the mirrors than for bare glass. This indicates that some light is absorbed in the mirror itself, rather than being transmitted into the module. The energy from the light absorbed in the mirror, instead of being (partially) converted to electricity by the cell, is instead converted to waste heat. The thermal benefits and temperature decreases provided by the modules containing spectrally-selective mirrors, however, are still a demonstration of the ability of sub-bandgap reflective mirrors to passively cool photovoltaic modules installed outdoors. The four-layer mirror reflects up to 22% additional light in the sub-bandgap spectral range, while the twelve-layer mirror reflects up to 44% additional light. Both modules with spectrally-selective mirrors reflect less useful light than the baseline module.

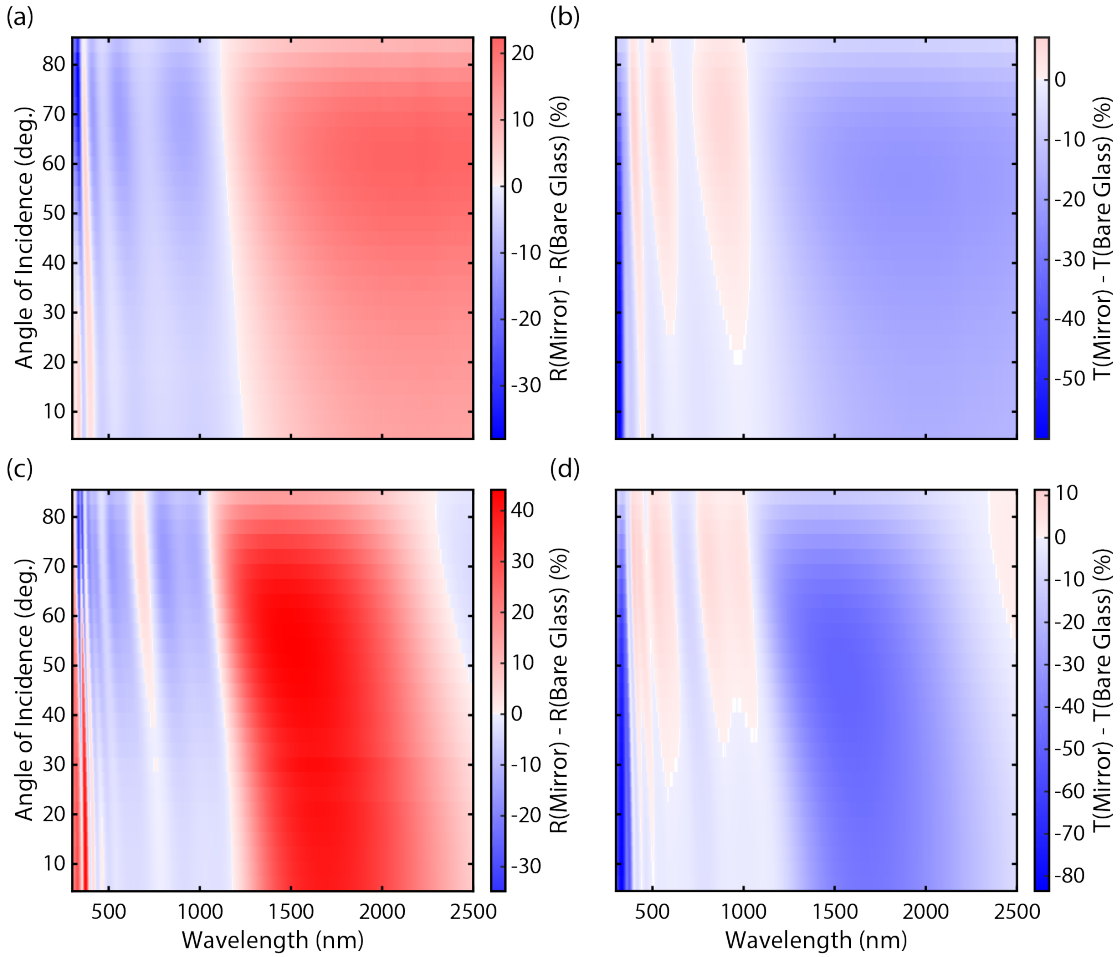

***Figure 6.4**: Experimentally measured reflection difference between the four-layer mirror on glass and bare glass (a) and transmission difference (b). Experimentally measured reflection difference between the twelve-layer mirror and on glass and bare glass (c) and transmission difference (d). The plots are shaded so that increased reflection/transmission appears red while decreased reflection/transmission appears blue.*

The modules with spectrally-selective mirrors showed reduced operating temperatures because their increase in sub-bandgap reflection was greater than their parasitic absorption above the bandgap. From experimental reflection and transmission measurements in **Figure 6.4**, under 1000 W/m^2 AM1.5G irradiance and compared to bare glass, the four-layer mirror would absorb an additional ~50 W/m^2 before that light could reach the cell. Each cell is ~14% efficient, so assuming a flat cell quantum efficiency, the mirror absorption prevented 7 W/m^2 of electricity generation and instead increased waste heat by the same amount. For the 12-layer mirror, the same calculations give ~40 W/m^2 additional absorption and 6 W/m^2 additional waste heat and reduced electricity output.

However, the mirrors reduce total waste heat via sub-bandgap reflection. For the four-layer mirror 18 W/m^2 of sub-bandgap light are reflected, with 44 W/m^2 reflected for the twelve-layer mirror. The mirror absorption reduces module power output both by blocking light from reaching the cell and by converting the absorbed light into heat. However, due to the strong sub-bandgap reflection of both the four-layer and twelve-layer mirrors, the modules with those mirrors reduce total waste heat generation by 11 W/m^2 and 38 W/m^2, respectively.

The observed temperature differences between the baseline module and the modules with spectrally-selective mirrors could also arise from shifting the location of waste heat generation from the cell to the mirror. Steady-state, 1-D heat transfer calculations using glass, encapsulant, cell, and backsheet conductivities and thicknesses from Silverman *et al.*[92] show that redistributing 40-50 W/m^2 heat generation from the cell to a thin layer at the front of the glass, without changing total waste heat generation, would reduce the cell temperature by 0.1 K. For the module including the four-layer mirror, redistribution of waste heat could account for most of the 0.16 K decrease in temperature with respect to the baseline module, with sub-bandgap reflection contributing in smaller proportion. The 1.5 K temperature reduction in the module including the twelve-layer mirror cannot be fully explained by shifting waste heat generation away from the cell. The reduction in total waste heat generation from sub-bandgap reflection contributed to over 90% of the temperature decrease.

6.4.5 Explanation of Absorption via the Time-Independent Model

A comparison of outdoor test results with results of the time-independent matrix model allows for further investigation into the performance of the mirrors and a possible explanation of their absorption. With the exception of TiO_2 at wavelengths <400 nm, none of the materials in either mirror absorb light between 300 nm and 2500 nm, as verified with spectroscopic ellipsometry. The time-independent matrix model does not predict the negative optical benefit observed in the outdoor test. It is plausible, however, that during mirror fabrication an absorbing material was formed at the interface between two layers. Both the four-layer mirror and the twelve-layer mirror have exactly one layer of SiN_x which sits atop a layer of TiO_2. During deposition of SiN_x via PECVD, a thin layer of TiN_x could

unintentionally form in both mirrors at the interface. TiN_x absorbs strongly at all visible and near-IR wavelengths.

Using refractive index data from Pflüger *et al.*,[150] a thin layer of parasitic TiN_x was inserted at the interface between the TiO_2 and SiN_x layers. The thickness was varied between 0 nm and 4 nm, and the time-independent matrix model was used to evaluate the mirror benefit with the inserted TiN_x layer. **Figure 6.5** shows the resulting optical benefits (solid lines) and thermal benefits (dashed lines) as a function of TiN_x thickness for both the four-layer and twelve-layer mirror. A thickness of 0 nm corresponds to the unmodified mirror design.

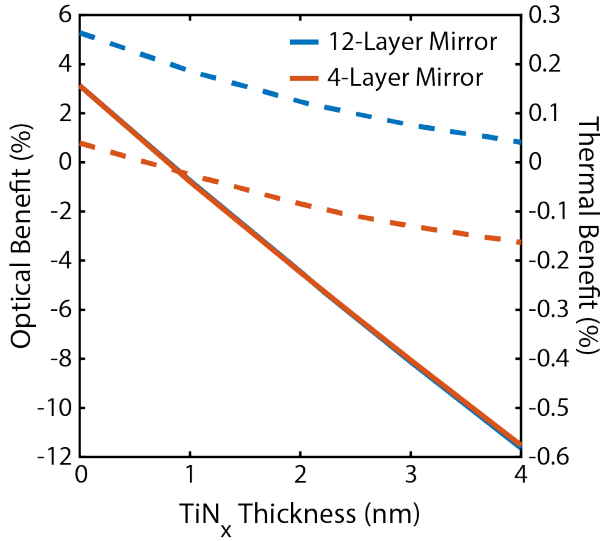

***Figure 6.5**: Variation of optical benefit (solid lines) and thermal benefit (dashed lines) of the twelve-layer and four-layer mirrors as a function of the thickness of a parasitic layer of TiN_x between the TiO_2 and SiN_x layers. Benefits are taken from the time-independent matrix model.*

The thickness of TiN_x required to have the time-independent matrix model reproduce the optical benefits from the outdoor test is 2.5 nm for the 4-layer mirror and 2.2 nm for the 12-layer mirror. While this does not prove that TiN_x caused the mirrors to absorb light, it is consistent with the presence of an interfacial layer of TiN_x in both mirrors. Without any TiN_x the model predicts an optical benefit of 3.1% for both mirrors.

A final note about the comparison between the time-independent matrix model and outdoor test results is that the model uses the design thicknesses of the mirror instead of the estimated thicknesses in the fabricated mirrors, since the TiO_2 thicknesses are unavailable. The differences between the fabrication and design of up to several nm in

every layer will change the mirror reflection away from the optimized design. Still, as seen in the reflection results in **Figure 6.4**, even with fabrication errors and possible TiN_x formation, the realized mirrors still had both anti-reflection for most of 300-1200 nm and sub-bandgap reflection. The fabrication errors led to, for example, an increase in reflection compared to bare glass for the twelve-layer mirror at ~750 nm at incident angles >45°. In addition to TiN_x absorption, this will decrease the optical benefit. However most of the decrease in fabricated mirror transmission compared to bare glass, or compared to the mirror design, is not associated with increases in reflection from layer thickness errors, and must be due to absorption.

6.5. Conclusion

Two spectrally-selective mirrors on glass, of four and twelve layers, were designed using SiO_2, TiO_2, and SiN_x. For the design, the optical properties of each material were consistent with those experimentally determined on thin-film samples. These mirrors were fabricated on pieces of 6 in. x 6 in. glass, integrated into single-cell test modules, and installed at the NREL Outdoor Test Facility. As fabricated, both mirrors decreased reflection on glass above the bandgap, while increasing sub-bandgap reflection. Such mirrors would replace existing ARCs on module cover glass, and cool the module while simultaneously increasing its output power. When operated outdoors, modules made using the four-layer mirror and twelve-layer mirror operated 0.16 K and 1.5 K cooler than a baseline module with bare outer glass, respectively. In contrast, a module with an ordinary ARC operated 0.49 K hotter than baseline. While the modules containing spectrally-selective mirrors did not produce as much energy as the baseline module, this was likely due to unintentional absorption in the mirror introduced during fabrication.

Chapter 7 Performance of Spectrally-Selective Mirrors in PERC Modules and at Interior Module Interfaces

7.1. Introduction

Previously, 1 D aperiodic mirrors have been designed for the module glass to selectively reflect sub-bandgap light before it enters the module. Using these designs, the annual average operating temperature can decrease by ~1K and energy yield can increase by up to 4.0% compared to a module with bare glass, depending on the mirror design, module tilt angle, and geographic location. However, these models and mirror designs apply to the outer surface of the glass in c-Si modules. Reflectors located within the module offer advantages, including protection from scratches or erosion from exposure to weathering. Such a mirror could be located on the cell surface, replacing the existing SiN_x ARC. The refractive index contrast between the EVA encapsulant (n = 1.48) and the silicon (n = 3.5) is greater than that between the air (n = 1) and the module glass (n = 1.5), potentially making it easier to achieve high sub-bandgap reflection from the already reflective cell interface. However, c-Si cells are designed with the goal of admitting as much light as possible into the cell via SiN_x ARCs and pyramidal texturing, and such a mirror must be compatible with these requirements.[52,151–153] Alternatively, the mirror could be located at the rear of the module, which removes the requirement of spectral selectivity.

This chapter covers a comprehensive analysis of passive PV thermal management by assessing the temperature reduction for both aluminum back surface field (Al-BSF) modules and passivated emitter rear contact (PERC) modules containing idealized reflectors on the front glass, on the textured cell front surface, or on the cell rear contact. We investigate idealized structures to determine the limits of waste heat and operating temperature reduction, using TOMCAT simulations to determine operating temperature and energy yield.

It is shown that, with high enough reflection, spectrally selective mirrors at the cell surface can effectively lower the module operating temperature, multiple reflections from

the cell texture limit the performance of these mirrors. In comparison, spectrally-selective mirrors on glass are the only ones capable of preventing parasitic absorption in the encapsulant materials, and offer the greatest cooling. Cell rear reflectors are the least effective at module temperature reduction, however improvements in cell rear reflection are commonly inseparable from improvements in rear passivation quality and cell efficiency.[26,154–156] Provided that proper passivation is maintained, increasing cell rear reflection can provide additional thermal benefit.

7.2. Methods

7.2.1 Reflection Measurements

The reflection of bare or encapsulated c-Si cells was measured using a Cary 7000 (Al-BSF) or Cary 5000 (PERC) UV-VIS-NIR Spectrophotometer with a Diffuse Reflectance Accessory (DRA) attached. Baseline 100% reflection measurements were made with a diffuse reflectance standard at the back port of the integrating sphere in the DRA. Baseline 0% reflection measurements were made with the incident beam blocked prior to entering the DRA. Total reflectance, including diffuse and specular components, was measured between 300 nm and 2500 nm with the sample pinned against the back port of the integrating sphere such that no busbars were exposed. The incident angle of the beam was 3°.

7.2.2 TOMCAT Simulation of Al BSF and PERC Modules

The optical properties of Al BSF and PERC modules required for TOMCAT simulation are determined from ray-tracing following the optical models described in Section 4.3.2. Additionally, the thermal conductivities of all module components are assumed to be the same for both Al BSF and PERC modules. However, the electrical efficiency of the Al BSF and PERC modules are different. Module efficiencies are calculated using data from Gatz *et al.*[26], who report IQE, fill factor (FF), and bare cell efficiency, $\eta_{STC,cell}$, for both Al BSF and PERC cells. To convert from cell efficiency to module efficiency, we first assume that the bare cell short circuit current density, $J_{sc,cell}$, is

related to the bare cell absorption, $A_{Si,cell}$, returned by ray-tracing simulation *without encapsulant materials*, as shown in eq. 7.1.

$$J_{sc,cell} = q \int \varphi_{AM1.5G}(\lambda) \cdot A_{Si,cell}(\lambda) \cdot IQE(\lambda) d\lambda \tag{7.1}$$

The integration region is 300 – 2500 nm, q is the elementary charge and $\varphi_{AM1.5G}$ is the photon flux in the AM1.5G spectrum. Following from the definitions of $\eta_{STC,cell}$ and fill factor, and the Shockley diode equation for solar cells with ideality factor N,[157] the system of equations 7.2 - 7.6 has a unique solution for the unknown open circuit voltage $V_{oc,cell}$, maximum power voltage $V_{mp,cell}$ and current density $J_{mp,cell}$, ideality factor N, and dark current density J_0.

$$\eta_{STC,cell} = \frac{V_{mp,cell} \cdot J_{mp,cell}}{\int P_{AM1.5G}(\lambda) d\lambda} \tag{7.2}$$

$$FF = \frac{V_{mp,cell} \cdot J_{mp,cell}}{V_{oc,cell} \cdot J_{sc,cell}} \tag{7.3}$$

$$J_{sc,cell} = J_0 \left(exp\left(\frac{qV_{oc,cell}}{Nk_BT} \right) - 1 \right) \tag{7.4}$$

$$J_{mp,cell} = J_{sc,cell} - J_0 \left(exp\left(\frac{qV_{oc,cell}}{Nk_BT} \right) - 1 \right) \tag{7.5}$$

$$V_{oc,cell} = V_{mp,cell} + \frac{Nk_BT}{q} ln\left(\frac{qV_{mp,cell}}{Nk_BT} + 1 \right) \tag{7.6}$$

Once parameters from the bare cell IV-curve are known, a module efficiency is determined by starting again with short-circuit current density, $J_{sc,module}$, determined via ray-tracing simulation *with encapsulant materials*, as shown in eq. 7.7.

$$J_{sc,module} = q \int \Phi_{AM1.5G}(\lambda) \cdot A_{Si,module}(\lambda) \cdot IQE(\lambda) d\lambda \tag{7.7}$$

Note that the relevant absorption, $A_{Si,module}$, is the cell absorption within the module, which is reported separately from encapsulant absorption by the ray-tracing software. Current density as a function of voltage for the module is fully determined by $J_{sc,module}$, with N and J_0 kept from the solution to eqs. 7.2 - 7.6. The maximum power, $P_{mp,module}$, is extracted from the IV-curve and inserted into eq. 7.8 to calculate the module efficiency.

$$\eta_{STC,module} = \frac{P_{mp,module}}{\int P_{AM1.5G}(\lambda) d\lambda} \tag{7.8}$$

Table 7.1 lists the IV-curve parameters for both the Al BSF and PERC cells from eqs. 3-4, with cell efficiencies and fill factors from Gatz *et al.*[26]

Table 7.1: Efficiencies and IV-curve parameters for Al BSF and PERC cells and modules

Cell	Efficiency (%)[26]	FF (%)	J_{sc} (mA cm^{-2})	V_{oc} (V)	N	J_0 (mA cm^{-2})
Al BSF	18.7	79.8	38.2	0.609	1.27	3.12 x 10^{-7}
PERC	19.5	77.2	39.8	0.630	1.57	6.32 x 10^{-6}
Module	**Efficiency (%)**	**FF (%)**	**J_{sc} (mA cm^{-2})**	**V_{oc} (V)**	**N**	**J_0 (mA cm^{-2})**
Al BSF	17.8	79.8	36.4	0.608	1.27	3.12 x 10^{-7}
PERC	18.7	77.2	38.2	0.628	1.57	6.32 x 10^{-6}

7.2.3 Optimization of Spectrally-Selective Mirrors for the Textured Cell Surface

Mirrors for the cell surface are optimized following the time-independent matrix model as described in Section 4.4. In this case, the mirror changes the reflection from the cell surface, instead of the outer glass. Reflection from the existing SiN_x ARC is small at all wavelengths, and the influence of this reflection on subsequent absorption in the module could be ignored. However, when sub-bandgap reflection is present at the cell surface, a significant portion may be absorbed elsewhere in the module. Therefore, while the basic idea of the time-independent matrix model remains the same, the method of obtaining absorption within each module layer must change.

The fraction of incident light absorbed in each module layer is instead determined by referencing ray-tracing results. A series of ray-tracing simulations are run for the Al BSF module, where the reflection from the cell surface is kept constant. Results, in terms of the absorption within the module, are collected as a function of wavelength (300 - 2500 nm), angle of incidence on the module (0° - 90°), and cell surface reflection (0% - 100%). The thin-film layers of the mirror are assumed to follow the cell surface texture conformally. The reflectance of the mirror is calculated versus wavelength, and the values of module absorption are interpolated from ray-tracing results and used in the time-independent matrix model.

The mirror reflectance is calculated using the transfer matrix method, considering only the first reflection from the mirror. Up to four different pyramid faces are exposed to the incident light for the first reflection, each making a different angle with respect to that

light. The average reflection, weighted by $\cos(\alpha_i)$, where α_i is the angle of incidence for pyramid face i, is used for interpolation. The angles α_i are calculated in eq. 7.9, where $\widehat{\boldsymbol{k}}_{\boldsymbol{in}}$ is the incident unit wavevector and $\widehat{\boldsymbol{n}}_i$ is the pyramid face unit normal vector. The incident wavevector is a function of the angle of incidence on the module.

$$cos(\alpha_i) = \widehat{\boldsymbol{k}}_{\boldsymbol{in}} \cdot \widehat{\boldsymbol{n}}_i \tag{7.9}$$

This optimization method allows inclusion of cell surface mirrors, without requiring repeated ray-tracing. Ray-tracing results only have to be collected once to form a database which is sampled during optimization. However, the ray-tracing uses constant reflectance from the cell surface, when a real mirror will have reflectance as a function of incident angle. Therefore, the same level of agreement between the time-independent matrix model and TOMCAT simulations is not expected for cell surface mirrors. But, this method is still useful for arriving at candidate mirror designs for the cell surface.

7.2.4 Deposition and Imaging on Al BSF Cells

Deposition on bare cells was done by either atomic layer deposition (ALD), to deposit Al_2O_3 and TiO_2, or by plasma enhanced chemical vapor deposition (PECVD), to deposit SiO_2 and SiN_x as described in Section 6.3.1.

Cross-sectional SEM images were taken with a FEI Helios G4 UX microscope, with both an electron and Gallium ion beam in the chamber. Images were prepared by first finding a suitable location on the sample, away from contact wires, busbars, and marks from saw damage. A protective layer of Pt was deposited over the pyramid chosen for imaging, and its cross section was exposed via milling by the ion beam. The sample was rotated such that the cross section was parallel to one side of the pyramid base. Therefore, the plane of the cross section would contain the normal to two of the pyramid faces, and the lengths measured in cross-sectional images would be the thicknesses of each layer. Once prepared, secondary electron images of the cross-section were taken at a working distance of ~4 mm using an accelerating voltage of ~2 kV. In the chamber the electron and ion beams make an angle of ~52° with respect to each other, and the electron beam views the cross-section at an angle of ~38°. The image plane, therefore, is never parallel or co-planar with the cross section. At high magnification, due to limited focal depth, the entire

image cannot be simultaneously in focus. We made effort to achieve sharp focus and eliminate astigmatism, however residual astigmatism, rotational misalignment, and the non-conductivity of the dielectric layers all contribute to poorer image quality and more uncertainty in thickness measurements.

7.3. Comparison of Modeled and Experimental Module Reflection

7.3.1 Optical Model of Al BSF and PERC Modules

The experimental reflection measurements of Al BSF and PERC modules are compared to the optical model developed in Section 2.3.2. **Figure 7.1** shows the reflection from separate models constructed for Al BSF and PERC modules along with experimental reflection measurements. The models and experiments agree across the solar spectrum for both types of modules. With this agreement, ray-tracing simulations with or without optical modifications, and subsequent calculations of operating temperature, can be taken as representative of a typical Al BSF or PERC module.

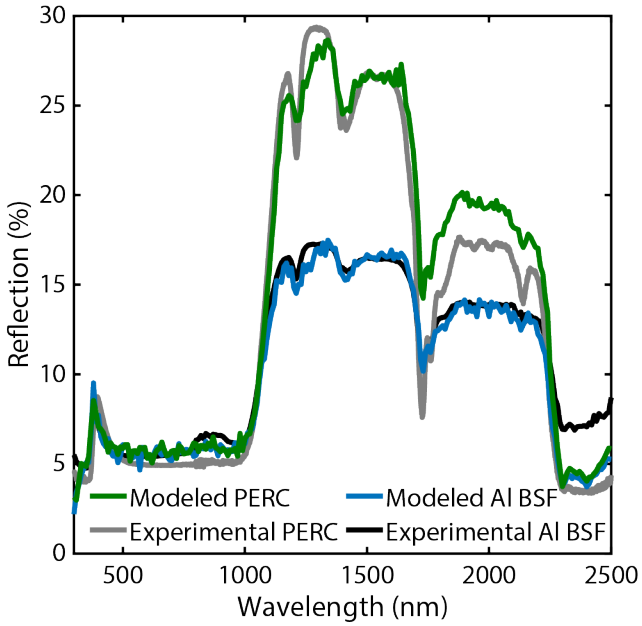

***Figure 7.1**: Comparison of experimental (black/grey) and modeled (blue/green) reflection for Al BSF and PERC modules.*

The reflection spectra in **Figure 7.1** can be understood in terms of the module materials and their optical properties. Outside of the cell, the encapsulant materials are responsible for some parasitic absorption in both the Al BSF and PERC modules. These

materials, low-Fe glass and EVA, are transparent at visible wavelengths, but have some sub-bandgap absorption. In particular, the EVA has absorption peaks at approximately 1200 nm, 1400 nm, 1750 nm, and 2300–2500 nm which are observed in the experimental data and ray-tracing results as these wavelengths would otherwise be reflected more strongly. Reflection at visible wavelengths is due mostly to specular reflection from the glass, which is uncoated in both the experimental measurements and in the optical model. Some reflection at visible wavelengths also comes from the cell, but between the SiN_x ARC and the surface texturing, the vast majority of visible light is not reflected, and is instead absorbed in the cell.

At sub-bandgap wavelengths, the bulk Si cannot absorb light, other than via free-carrier absorption. At these wavelengths, since the Si is transparent, and the encapsulant materials are at least partially transparent, reflection and absorption at the cell rear contact dominates the total amount of parasitic absorption in the module. In the optical model for both cell types, the rear contact is Al and includes a layer of Al/Si eutectic as the back surface field. The eutectic layer absorbs light, and accounts for the vast majority of the cell parasitic absorption. In the PERC cell, the back contacts are localized in a line pattern, with dielectric passivation layers between contact lines. In this case, the width of the back contact lines within the PERC optical model was varied to reach better agreement with experimental results. The PERC cell, with some passivated non-contact area at the cell rear, absorbs less sub-bandgap light and reflects more compared to the Al BSF cell.

7.3.2 Reflection of Modules with Idealized Mirrors

To isolate effects of sub-bandgap reflection, idealized mirrors are incorporated into Al BSF and PERC modules at the glass and cell surface. The idealized mirrors at these interfaces have constant wavelength- and angle-independent reflection for $\lambda > 1160$ nm, but do not modify reflection at shorter wavelengths, where the wavelength and angle dependence are retained. Schematics showing the placement of these mirrors within the module are given in **Figures 7.2a** and **b**, respectively. At the cell surface, the mirror replaces the existing SiN_x ARC. To illustrate the effects of mirrors on module reflection, **Figure 7.3** shows the module reflection at normal incidence as a function of mirror sub-bandgap reflection. These modules have spectrally-selective mirrors on the cell surface in

Figures 7.3a and **c**, and on the glass in the **Figures 7.3b** and **d**. Reflection from Al BSF modules is given in **Figures 7.3a** and **b**, and from PERC modules in **Figures 7.3c** and **d**.

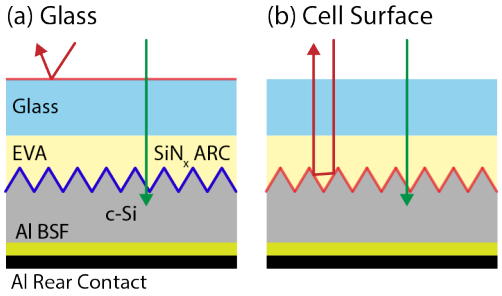

***Figure 7.2**: Schematic showing the location of idealized spectrally-selective mirrors within the module at either (a) the glass interface or (b) the cell surface interface. At the cell surface, the mirror follows the texture and replaces the SiN_x ARC.*

The reflection spectra shown in **Figure 7.3** illustrate key differences between mirrors applied to the cell surface versus the glass. For modules with interior mirrors, module reflection is always less than 100%, even when the mirror reflects all sub-bandgap light, as reflection from the cell surface does not prevent parasitic absorption in the glass or encapsulant. Particularly near 1200 nm, 1400 nm, 1750 nm, and 2300-2500 nm where encapsulant absorption is strong, most light entering the module does not leave, even if the cell surface reflection is high. Modules that have mirrors on glass, however, can reflect up to 100% of incident sub-bandgap light, since reflection occurs before any opportunity for parasitic absorption. Furthermore, the module reflection is at least as high as the mirror reflection for glass mirrors, since the module reflection is the sum of reflection from the mirror and reflection from the module interior. In contrast, when the mirror is applied to the cell surface, module reflection is less than mirror reflection when the mirror is more than 50% reflective. Light must reflect at least twice from the cell texture before escaping the module, which increases transmission to the cell. For example, if incident light reflects twice from a 50%-reflective mirror on the cell, only 25% will return towards the module surface, and 75% will transmit to the cell. This leads to a non-linear dependence of module reflection on mirror reflection at the cell surface, such that low reflectivity mirrors are ineffective.

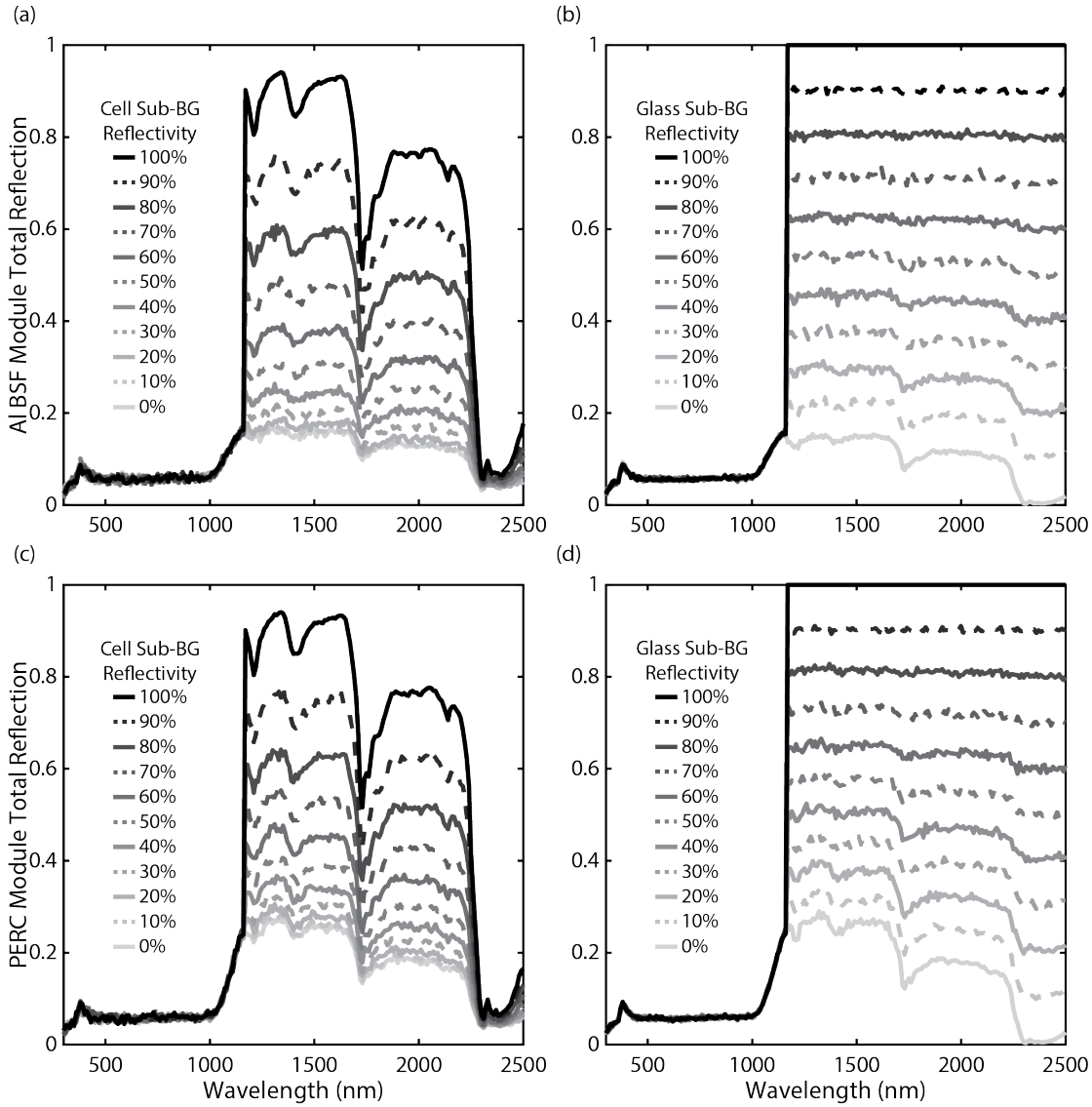

***Figure 7.3**: Module reflection, for (a) and (b) an Al BSF module and (c) and (d) a PERC module as the sub-bandgap reflectivity of a spectrally-selective mirror is varied from 0% to 100%. In (a) and (c), the mirror is on the cell surface. In (b) and (d) the mirror is on the glass. From 300 nm to 1160 nm, reflection is unmodified compared to the baseline module. Incident light is normal to the module.*

The sub-bandgap reflected power in the AM1.5G spectrum is shown in **Figure 7.4**, based on the spectra in **Figures 7.3a-d**. Modules with mirrors on the glass and reflect up to 170 Wm^{-2} sub-bandgap light, or all sub-bandgap light in the solar spectrum. Modules, with mirrors on the cell reflect up to 136 Wm^{-2} sub-bandgap power. For perfectly reflective mirrors, the total power reflected by the module does not depend on the module type since no sub-bandgap light reaches the cell. However, the increase in sub-bandgap reflection for

a particular mirror does depend on the module type. The baseline Al BSF module already reflects 24 Wm^{-2} sub-bandgap light, and the baseline PERC module reflects 37 Wm^{-2}. The dielectric passivation at the cell rear contact increases the reflection of PERC modules relative to Al BSF modules, and when the same mirror is applied, PERC modules always have higher reflection. However, the mirrors provide a greater benefit to Al BSF modules in the sense that they have a greater increase in their sub-bandgap reflection.

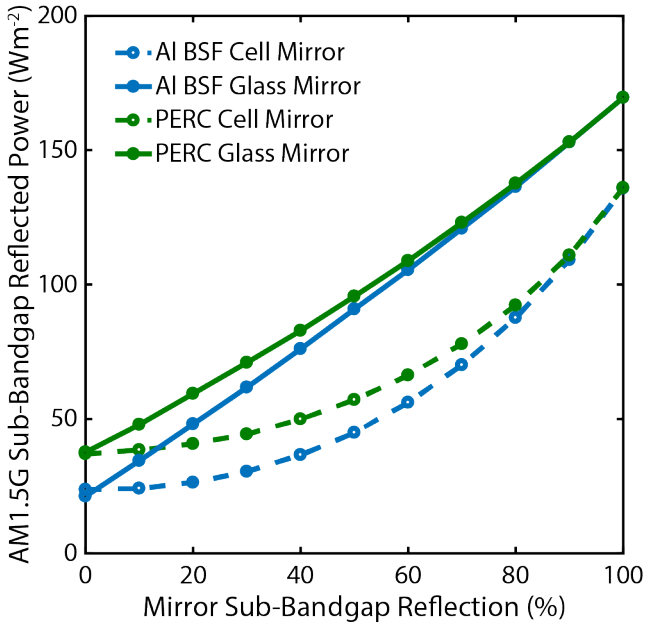

***Figure 7.4**: Reflected power from Al BSF (blue) and PERC (green) modules as a function of idealized mirror reflection at the cell surface (dashed lines) or glass (solid lines), integrated over the sub-bandgap portion of the AM1.5G spectrum (>1160 nm).*

Figure 7.4 also reinforces the same comparisons between glass mirrors and cell surface mirrors made above. If the mirror is applied to the cell, parasitic absorption in the glass and encapsulant, and multiple reflections from the cell texture decrease the total power reflected by the module. Given incident sub-bandgap power of 170 Wm^{-2}, both Al BSF and PERC modules require more than 70% reflection at the cell to reject at least 85 Wm^{-2}, or half the incident power. Even when all sub-bandgap light is reflected from the cell, parasitic absorption of 34 Wm^{-2}, or 20% of the incident power, cannot be prevented.

7.3.3 TOMCAT Simulations of Modules with Integrated Idealized Mirrors

Simulations of idealized mirrors under a full year of outdoor conditions using TOMCAT determined the cooling provided. These mirrors are applied to both Al BSF and

PERC modules, either on the module outer glass, textured cell surface, or cell rear. These 'mirrored' modules are compared to the 'baseline' modules established earlier, whose reflection matches experimental measurements. Modifications to Al BSF modules are compared to the Al BSF baseline, and likewise for PERC modules. When comparing to a baseline module using these idealized mirrors, the operating temperature differences arise only from sub-bandgap reflection. A realistic, optimized, mirror design for the front of the module would reduce reflection for $\lambda < 1160$ nm to some extent, in addition to increasing sub-bandgap reflection.[78] Then, module temperature depends on the changes in visible reflection on waste heat sources such as thermalization and recombination of hot carriers, or parasitic UV absorption.

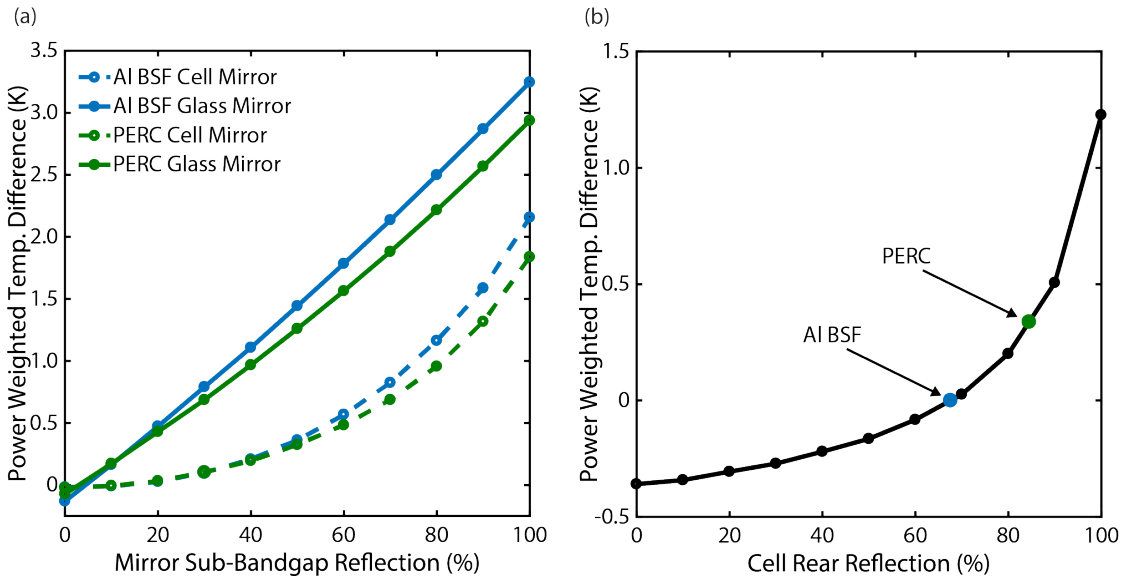

***Figure 7.5**: (a) Power-weighted average module operating temperature difference from the baseline case for Al BSF (blue) and PERC (green) modules including spectrally-selective mirrors at the glass (solid lines) or cell surface (dashed lines). (b) Temperature differences as a function of cell rear reflection (at all wavelengths). The equivalent rear reflections of Al BSF (blue) and PERC (green) cells are marked. Temperature differences are calculated from full-year simulations results with weather and irradiance corresponding to Denver, CO, with modules at 30° fixed tilt facing due south. Reflection was swept from 0% to 100%, shown by the circular symbols. The lines are to guide the eye.*

As greater sub-bandgap reflection is applied to a module, its temperature difference with respect to the baseline increases regardless of the interface at which reflection occurs. **Figure 7.5a** shows the calculated temperature differences for idealized mirrors on the glass and cell surface, and **Figure 7.5b**, for idealized mirrors at the cell rear. Annual average

temperature differences were calculated such that a positive temperature difference indicates a reduction in operating temperature. For all modules, idealized cases with 0% sub-bandgap reflection operate warmer than baseline modules. In the baseline modules, the glass, cell surface, and cell rear all have some sub-bandgap reflection, so applying 0% reflection at either interface is a reduction in sub-bandgap reflection, leading to an increase in parasitic absorption and operating temperature. In the best case, a 3.3 K annual average reduction in operating temperature was calculated for a 100% reflective mirror on glass in an Al BSF module.

While idealized mirrors on glass could provide ~3 K cooling or more, idealized mirrors on the cell only offered up to 2.2 K and 1.8 K cooling for Al BSF and PERC modules, respectively. Furthermore, while the module operating temperature decreases approximately linearly with sub-bandgap reflection on glass, the temperature reduction has a higher order dependence on reflection at the cell surface. As noted earlier, this suggests disadvantages for cell surface sub-bandgap reflection compared to sub-bandgap reflection from the glass. The cell texture, which increases absorption of photons with energy above the bandgap by forcing multiple reflections, also hinders the ability of spectrally-selective mirrors to reduce module operating temperature both by increasing the interactions with the parasitically absorbing encapsulant and by requiring high reflectivity surfaces.

Furthermore, there are differences between modules containing Al BSF and PERC cells. The data in **Figure 7.5a** show that for a given sub-bandgap reflection, the temperature difference compared to baseline is generally lower for PERC than for Al BSF. According to the experimental reflection measurements and ray-tracing reflection shown in fig. 2, the baseline PERC module reflects more, and absorbs less, sub-bandgap light than the baseline Al BSF module. Additionally, the PERC cell is more efficient than the Al BSF cell, so a greater fraction of the energy of each carrier is extracted instead of converted to waste heat. Comparison of the two baseline modules using our combined optical, thermal, and electrical simulations show the PERC module operating 0.53 K cooler than the Al BSF module based on an annual average operating temperature. Experimentally, Vogt *et al.*[154] have demonstrated a 1.7 K temperature difference between PERC modules and Al BSF modules under 1000 Wm^{-2} AM 1.5G illumination. This larger temperature difference arises both from the high incident intensity used during the measurement and the lack of

convective heat transfer from wind. When mirrors are applied, the operating temperature decreases as sub-bandgap parasitic absorption is suppressed. As there is less waste heat from sub-bandgap parasitic absorption for the PERC module than for the Al BSF module, the change relative to baseline is greater for Al BSF than for PERC.

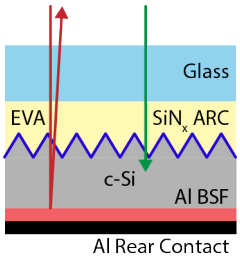

***Figure 7.6**: Schematic showing a cell rear reflector within the module. This reflector does not need to be spectrally-selective, but would ideally passivate the rear contact.*

The thermal improvements offered by reflection at the cell back contact was then studied, along with a comparison of the back contact reflection of Al BSF and PERC modules. A schematic is given in **Figure 7.6**. A PERC module is ~5% more efficient than an Al BSF module in our simulations, an improvement arising mainly from dielectric passivation at the back contact. The Al/Si electrical contact covers a relatively small area in the PERC cell compared to the full area contact in the Al BSF cell. The remainder of the cell back surface is passivated by dielectrics, which form a much more reflective interface with the Al than the exposed Si. To place this in the context of the idealized mirrors discussed above, and to determine the possible temperature reductions of further improvement in back contact reflection, included in **Figure 7.5b** are points corresponding to the Al BSF baseline (at zero temperature change) and the PERC baseline module to show the equivalent reflection of the back contact. The 0.53 K temperature reduction of PERC modules compared to Al BSF modules arises from reduced sub-bandgap absorption and improved efficiency. To determine the equivalent rear reflection of PERC cells, we run a full-year simulation using the PERC optical model, but using the Al BSF electrical properties from **Table 7.1**. The resulting temperature difference of 0.34 K and the equivalent rear contact reflection are shown in **Figure 7.5b**. Therefore, the remaining temperature difference of 0.19 K is due to improved cell efficiency.

Overall, when varying the reflection at the back contact, the temperature reduction has a similar non-linear dependence as that seen when varying cell surface reflection. This

is likely due to light trapping within the cell forcing multiple interactions of sub-bandgap light at the rear contact. While the equivalent reflections of the rear contact in Al BSF and PERC modules are already high, at 67% and 85%, respectively, further temperature reduction is possible if rear contact reflection were improved.[155] However, optimizing reflection at other interfaces provides more module cooling. With 100% reflection, a 1.2 K operating temperature decrease is possible, although such high reflection is not realistic given the requirement to also form an electrical contact at the back surface. A 90% reflective rear surface yields only a 0.51 K temperature difference compared to the Al BSF baseline, only a couple of tenths of a degree more than the PERC baseline. But, there is no requirement for spectral-selectivity at this interface, making design of alternate rear passivation coatings simpler than mirrors at other interfaces.

Our simulations show that, regardless of module type, spectrally-selective mirrors on either the glass or cell surface, or increases in the cell rear reflection, can reduce annual average module operating temperature. The largest temperature reductions are available for glass mirrors. Glass mirrors reflect sub-bandgap light before it enters the module, and therefore have the greatest potential to prevent parasitic absorption. In the limit of 100% sub-bandgap reflection, cell surface mirrors cannot provide as much cooling as glass mirrors, but are protected from weathering effects inside the module. Multiple reflections from the cell texture allow sub-bandgap light to enter the cell unless mirror reflection approaches 100%, which greatly hinders cooling. Modifications to the cell rear contact are typically performed to improve the electrical properties of the cell, with improved reflection being a side-effect. Even if efficiency was unchanged, our simulations show that cooling up to 1.2 K is possible with increased cell rear reflection. We note that the high efficiency pluto cells from Suntech[156] have 65% sub-bandgap reflection, a drastic improvement compared to the Al BSF and PERC cells studied here.

Realistically, if 50% - 60% reflection is attained at the glass interface,[8] ~1.5K temperature reductions compared to baseline are possible. Assuming a 0.39% relative increase in cell efficiency per degree cooling,[92] ~0.6% energy yield increases are possible from thermal effects of the mirror alone. Optimization of the mirror to provide antireflection of useful light could increase module energy yield further.[78]

7.4. Optimization of Cell Surface Mirrors

Three cell mirrors were optimized as described previously, making reference to ray-tracing results of constant reflectance mirrors. The mirrors have either 6 layers, 25 layers, or 31 layers, none of which are the SiN_x ARC layer of the baseline cell. The initial condition for optimization of the 6-layer mirror was one layer of Al_2O_3 on top of one layer of TiO_2, each of 100 nm thickness. The initial condition for both the 25- and 31-layer mirrors was a 5 period Bragg stack of SiO_2 and TiO_2, where each layer had 400 nm optical thickness. Additional layers were added as optimization progressed, with materials selected from SiO_2, SiN_x, Al_2O_3, TiO_2, and MgF_2.[134] The 31-layer mirror was also allowed to include HfO_2.

Table 7.2: TOMCAT Simulation results for optimized cell surface mirrors

Mirror	Optical Benefit	Thermal Benefit	Op. Temp. Decrease (K)
6-Layer	0.23%	0.00%	-0.02
25-Layer	-1.38%	0.20%	0.52
31-Layer	0.02%	0.06%	0.06

Cell mirror reflection at an angle of incidence of 50.1°, corresponding to the first reflection at the cell of light normally incident to the module, is given for all cell mirrors and the baseline cell in **Figure 7.7**. The optical benefit, thermal benefit, and annual average operating temperature decrease relative to baseline resulting from full-year TOMCAT simulations are given in **Table 7.2** for all cell mirrors. The 6-layer mirror has the highest optical benefit at 0.23%, but zero thermal benefit, essentially making it an improved ARC over the single-layer SiN_x coating, although at some visible wavelengths reflection is higher for the 6-layer mirror. The 25-layer mirror has the highest thermal benefit at 0.20%, and has reflection >50% between ~1100 nm and 1500 nm with a peak of 63.4% reflection at 1240 nm. However, the 25-layer mirror also blocks visible light, yielding a negative optical benefit and a negative total benefit with an estimated power loss of over 1% compared to baseline. The 31-layer mirror does not block visible light, and has a sub-bandgap reflection band peaking at 48% reflection, but can only offer small optical and thermal benefits, with the total benefit being <0.1%.

The performance of optimized cell mirrors emphasizes some of the difficulties we identified regarding thermal management at the cell interface. Unavoidable parasitic absorption in the glass and encapsulant, and multiple reflections from the textured cell surface require cell mirror sub-bandgap reflection to be significantly higher to achieve the same thermal benefit as a mirror on a flat interface or an interface at the module exterior. The 25-layer cell mirror has a similar reflection bandwidth to and higher reflection peak than our previously designed spectrally-selective mirrors for the module glass, yet has a lower thermal benefit because it operates at the cell interface. Comparing to the previous simulation of idealized cell surface mirrors, the ~50% reflection over a band containing most of the sub-bandgap AM1.5G power would offer <0.5K temperature reduction. The 0.52 K simulated temperature reduction is increased by the reduced thermalization and entropic losses given the negative optical benefit, and is still lower than temperature reductions of glass mirrors. Optical benefits are also limited at this interface, as, with the exception of blue wavelengths, reflection from the SiN_x ARC is low. Full-year simulations with TOMCAT of a cell with a perfect ARC give only a 0.54% optical benefit. The 6-layer mirror achieves slightly under half of the ideal optical benefit at the cell interface at 0.23%, a similar fraction of the ideal optical benefit achieved by optimized mirrors on glass, where between 40% and 50% of the >7% ideal optical benefit was calculated. A mirror design which simultaneously achieves a significant optical and thermal benefit was not found.

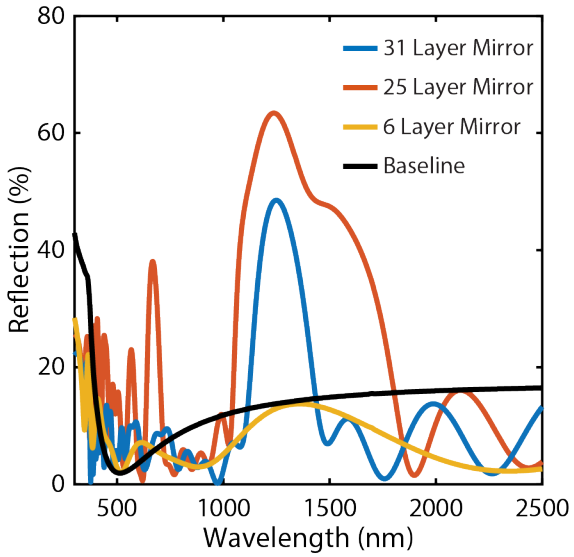

***Figure 7.7**: Cell mirror reflection at a 50.1° angle of incidence, the approximate base angle of the cell pyramid texture. The baseline refers to the SiN_x cell ARC.*

7.5. Deposition of Thin Films on c-Si Cells

To test feasibility of cell surface mirror fabrication. Additional dielectric layers were deposited onto c-Si cells over top of the existing SiN_x ARC. **Figures 7.8a-b** give representative SEM images of cross sections of the surface texture of two different cells with two additional layers deposited on each. In **Figure 7.8a**, the sample is a cell with two layers deposited by ALD, Al_2O_3 on top of TiO_2, and the existing SiN_x ARC. The cell in **Figure 7.8b** has two layers deposited by PECVD, SiN_x on top of SiO_2, and the SiN_x ARC. These two cells are chosen as deposition quality may change depending on the instrument used, with possible ramifications for their reflection. As shown in **Figure 7.8a**, the layers deposited by ALD are very conformal and have uniform thickness on the imaged pyramid. The TiO_2 layer is measured at 20 nm and the Al_2O_3 layer is 55 nm. Deposition by PECVD, **Figure 7.8b**, gives layers which are still conformal, but not perfectly uniform in thickness. Compared to the 252 nm measurement on the right side of the pyramid, the thickness at the peak is the same, but the thickness near the valley is measured at only 236 nm, about 6% thinner. The trend of thinner measurements in valleys compared to the rest of the pyramid is consistent across multiple images of cells with additional dielectric layers deposited by PECVD. On the left side of the pyramid, the thickness measures 242 nm. However, the left and right sides of the pyramid have different views of the Pt source during deposition, and correspondingly different Pt deposition quality. The boundary between the Pt and the PECVD layers is more uncertain, and the 242 nm measurement is not taken to mean that one side of the pyramid has a different thickness than the other.

Due to the poor contrast between SiN_x and SiO_2 in secondary electron imaging, the boundary between the dielectric layers on the pyramid was not identified, only total thickness was measured. However, given the film thicknesses on the witness slides for these depositions, the thicknesses of SiO_2 and SiN_x are expected to be approximately equal. In addition, **Figure 7.8b** shows measurements of the apparent base angle of the pyramids. Given the relative angle between the image plane and pyramid cross section, the theoretical base angle of 54.74° would appear to be ~48° in the SEM image. The lower measurement of ~46° is at least qualitatively consistent with the results of scanning probe microscopy, showing a predominant base angle of less than 54.74° (see Appendix). On the far right side

of **Figure 7.8b**, there is a slope measurement of 22°. This is likely due to a shoulder between two adjacent pyramids. The face through which the cross section cuts likely has a normal which is nearly contained in the cross section, as there is no significant increase in film thickness on the right side of the valley. Again, this shows that planes other than the ideal {111}-type planes are exposed following texturization of the Si.

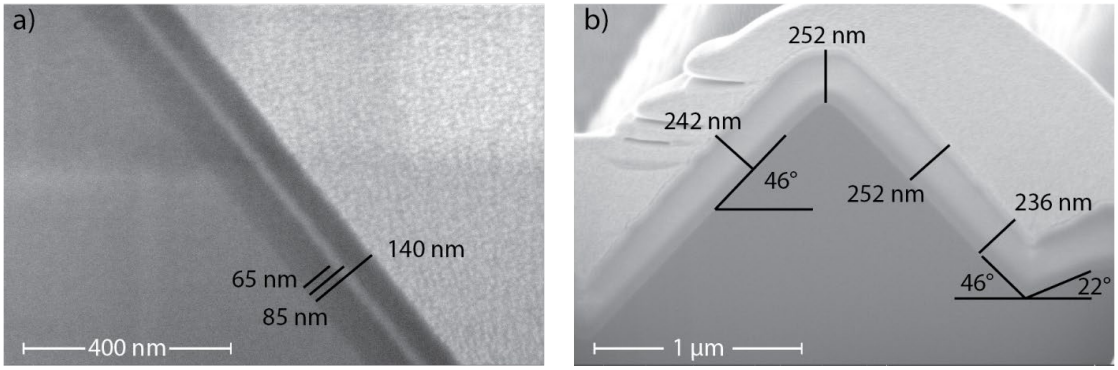

***Figure 7.8**: SEM images of cross sections of pyramidally-textured Si cells with a SiN_x ARC and a) a layer of Al_2O_3 on top of a layer of TiO_2, both deposited via ALD, or b) a layer of SiN_x on top of a layer of SiO_2, both deposited by PECVD. Thicknesses are referenced to the scale bars and labeled on the image itself. In b), the apparent base angle is also measured and labeled. A protective layer of Pt was deposited on top of the pyramid to protect it during ion beam milling.*

Prior to cross-sectional imaging, experimental reflection measurements were taken for each cell after additional layers were deposited. A comparison of experimental reflection results and ray-tracing results using the optical model described in Section 4.3.2 is shown in **Figure 7.9**. The additional layers were added on top of the SiN_x ARC with the measured thicknesses from cross-sectional imaging, and no additional model parameters were changed. In general agreement is very poor between the ray-tracing results and experiment. This is likely due to non-conformal or non-uniform deposition, which is not captured in ray-tracing. The ray-tracing algorithm assumes perfectly fine points at the tips of each pyramid of the cell texture. However, as additional thickness is added, the tips become more and more rounded, and take up a larger fraction of the surface area of the cell, making the assumption of fine tips invalid. Similarly, in the valleys between pyramids, rounding introduced by additional film thickness could distort the overall shape. Given the assumption in the ray-tracer of uniform thicknesses, any non-uniformity could cause disagreement with experimental measurements as well, although non-uniform thicknesses were only obvious for layers deposited by PECVD. It is not known how much these factors

contributed to the experimentally measured reflection, but it is clear that the existing ray-tracing model does not adequately describe the effects of the additional layers.

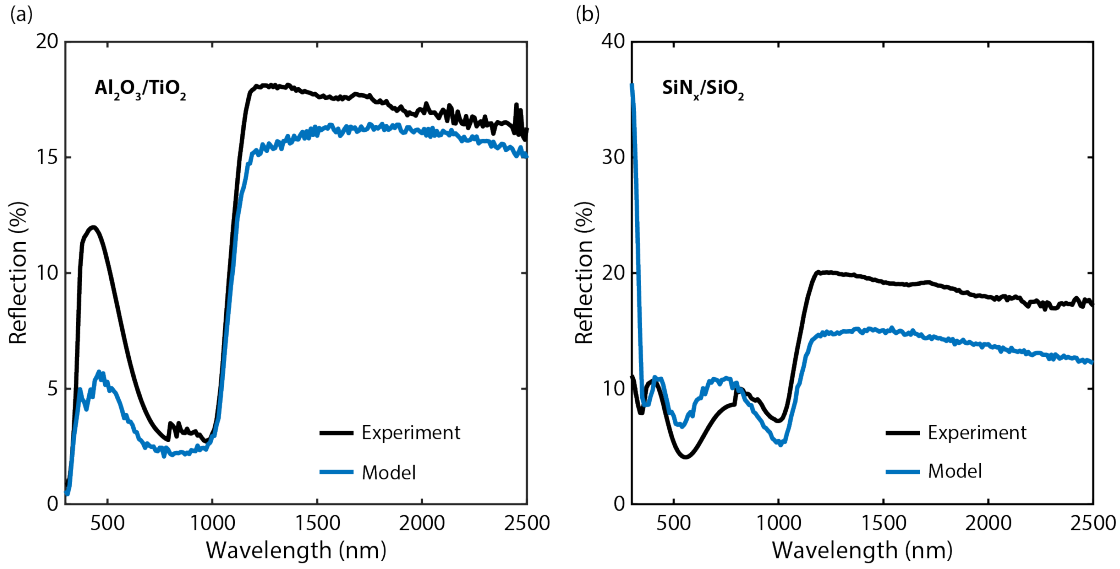

***Figure 7.9**: Comparison of experimentally measured reflection and modeled reflection for c-Si Al BSF cells with (a) a layer of Al_2O_3 deposited on top of a layer of TiO_2 by ALD and (b) a layer of SiN_x deposited on top of a layer of SiO_2 by PECVD. Both cells also include the SiN_x ARC. The model uses only the thicknesses of the deposited layers measured by cross-sectional imaging, no other parameters are changed.*

Given that the optimized cell mirrors are based on the optical model which has been shown to disagree with experimental measurements in the presence of additional layers on the cell surface, it may be possible to find successful mirror designs with an improved model. However, sub-bandgap reflection from the cell surface is disadvantaged because multiple interaction with the texture increase transmission and decrease reflection, and the position behind glass and encapsulant creates unavoidable parasitic absorption. These are limitations of the reflection itself, not of any particular mirror. Even if the model for changes in reflection at the cell surface due to additional layers improves, the limitations on cell surface mirrors as a whole remain.

7.6. Conclusions

In conclusion, this chapter has discussed and compared spectrally-selective mirrors on the outer module glass and cell surface, and reflectors at the cell rear contact. Each of these methods reduces the total parasitic absorption in a photovoltaic module by reflecting

sub-bandgap light, thereby reducing the module operating temperature. Temperature reduction estimates follow from ray-tracing optical models which agree with experimental module reflection measurements for both Al BSF and PERC cells. Full-year simulations of outdoor module performance showed that the greatest reductions in operating temperatures were provided by mirrors on the outer glass, with a 100% reflective mirror offering 3.3 K cooling for Al BSF modules and 2.9 K for PERC modules. Mirrors on glass reflect sub-bandgap light before it enters the module, and prevents its absorption in the encapsulant materials and the cell. Spectrally-selective mirrors on the cell surface, however, cannot prevent parasitic absorption in the glass or encapsulant. Therefore, these mirrors offer only up to 2.2 K cooling for Al BSF and 1.8 K cooling for PERC. In addition, the textured cell surface forces multiple reflections from the mirror. When sub-bandgap reflection is less than 100%, as it would be in any realistic scenario, sub-bandgap transmission to the cell increases. This renders cell surface mirrors much less effective than their glass counterparts. An 80% reflective cell mirror only achieves half of the cooling as a 100% reflective cell mirror, while the cooling of glass mirrors scales approximately linearly with mirror reflection.

Comparing simulations of Al BSF and PERC modules, we found that the baseline PERC module operated on average 0.53 K cooler than the baseline Al BSF module. The cooler operation of the PERC module arises from a more reflective cell rear contact and improved efficiency. Further increases to cell rear reflection could decrease the operating temperature by another 0.7 K. Spectral selectivity is not required at the cell rear, and high efficiency cells can take advantage of the high reflectivity provided by rear passivation.

Additionally, several mirror designs were optimized for the cell surface, and additional dielectric layers were deposited onto cells to test the feasibility of cell surface mirror fabrication. No optimized mirror design was able to provide both an optical and thermal benefit. A 6-layer design yielded an 0.23% optical benefit, but no thermal benefit, while a 25-layer design gave a 0.20% thermal benefit that was outweighed by an optical penalty from blocking light above the bandgap. The results of optimization emphasize the findings on idealized mirrors, that multiple reflections from the cell and placement behind glass an encapsulant limit the thermal benefit. Additionally, the optical benefit is limited by the already excellent performance of the SiN_x ARC.

Deposition of dielectric layers of Al_2O_3, TiO_2, SiN_x, and SiO_2 onto c-Si cells significantly changed its reflection. Cross-sectional imaging suggested that layers deposited by ALD were mostly uniform in thickness and conformally deposited, while layers deposited by PECVD varied in thickness, being thinner in valleys between pyramids. Inclusion of the additional layers in the optical model gave ray-tracing results which did not agree with experimental measurements, possibly due to rounding at pyramid tips or in valleys which is not captured in the model. More precise characterization or modeling of these additional layers is required to fully understand their effects on cell reflection.

Chapter 8 Backscattering Within the Module to Reject Sub-Bandgap Light

8.1. Introduction

In the previous chapter it was shown that with high enough reflection spectrally selective mirrors at the cell can effectively lower the module operating temperature, but that multiple reflections from the cell texture make realizing a given temperature reduction more difficult. Spectrally selective architectures at the cell interface that avoid multiple interaction can circumvent this issue. Therefore, selectively backscattering light from the cell before it can be parasitically absorbed is an alternative possibility for photovoltaic thermal management. Only one scattering event is required to redirect sub-bandgap light out of the module, compared to two or more reflections from the textured surface. A schematic showing selective backscattering is given in **Figure 8.1**.

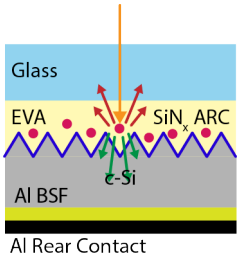

***Figure 8.1**: Schematic showing a particle (red circle) scattering sub-bandgap light out of the cell while allowing transmission above the bandgap. The particles do not replace the SIN$_x$ ARC and are not necessarily arranged in periodic fashion.*

Highly directional scattering from spheres exhibiting both dielectric and magnetic response was first proposed by Kerker *et al.*[158] More recent work has demonstrated that magnetic response can be induced in dielectric particles,[159,160] and that the lowest order resonant responses, the electric and magnetic dipoles, can be tuned to enhance forward scattering.[161–166] Enhanced backscattering is possible in a properly designed dielectric nanoparticle when its electric and magnetic dipole resonances are equal in magnitude, but oscillate out of phase.[167–169] When this condition is achieved, >90% of the incident light can be backscattered after a single interaction with the particle. The scattering particle also does not interfere with or replace the existing SiN$_x$ ARC. A functional spectrally-selective

scattering nanoparticle would require a precise design which is not attempted in this chapter. Instead, the amount of sub-bandgap rejection possible in an idealized case is considered, along with calculations necessary to determine this result. Backscattering sub-bandgap light can reduce operating temperatures as much as reflection from the cell surface, however both approaches are limited by absorption in the glass and encapsulant.

8.2. Calculations of Light Scattered Near the Cell Surface

Scattered power per unit solid angle (P_{scat}, $Wm^{-2}sr^{-1}$) from a multipole source near a planar substrate with thin films at the interface was calculated using eqs. 8.1 – 8.12. The scattered field as a function of direction (given by azimuthal angle φ and polar angle θ) and (vacuum) wavelength λ was determined separately for regions above ($\theta < 90°$) and below ($\theta > 90°$) the planar substrate, as shown in eqs. 8.1 and 8.2, where ε_0 is the vacuum permittivity, c is the vacuum speed of light, n is the refractive index, and $\underline{E}$ is the electric field vector. The subscripts *a*, and *t* refer to the regions above and below the substrate, respectively.

$$P_{scat}(\varphi, \theta < 90°, \lambda) = \frac{1}{2}\varepsilon_0 c n_a \underline{E_a} \cdot \underline{E_a} \tag{8.1}$$

$$P_{scat}(\varphi, \theta > 90°, \lambda) = \frac{1}{2}\varepsilon_0 c n_t \underline{E_t} \cdot \underline{E_t} \tag{8.2}$$

The field above the substrate, $\underline{E_a}$, is given by the superposition of fields directly scattered from the source, $\underline{E_0}$, and fields scattered and subsequently reflected, $\underline{E_r}$, as shown in eq. 8.3. In the region below the substrate, only the field $\underline{E_t}$ that was scattered and subsequently transmitted into the substrate is present.

$$\underline{E_a} = \underline{E_0} + \underline{E_r} \tag{8.3}$$

Electric field calculations for directly scattered light, scattered and reflected light, and scattered and transmitted light are performed following Evlyukhin *et al.*[170] and Novotny and Hecht.[171] Expressions for $\underline{E_0}$, $\underline{E_r}$, and $\underline{E_t}$ can be obtained using Green's tensor approximations for the far-field region, as shown in eqs. 8.4 – 8.6, where $\underline{P}$ is the polarization field, ω is the angular frequency, μ_0 is the vacuum permeability, and the integrals are performed over the volume of the scattering source.[170,171]

$$\underline{E}_0(\underline{r}) = \omega^2\mu_0 \int_{V_s} \hat{G}_0^{FF}(\underline{r},\underline{r}')\,\underline{P}(\underline{r}')d\underline{r}' \tag{8.4}$$

$$\underline{E}_r(\underline{r}) = \omega^2\mu_0 \int_{V_s} \hat{G}_r^{FF}(\underline{r},\underline{r}')\,\underline{P}(\underline{r}')d\underline{r}' \tag{8.5}$$

$$\underline{E}_t(\underline{r}) = \omega^2\mu_0 \int_{V_s} \hat{G}_t^{FF}(\underline{r},\underline{r}')\,\underline{P}(\underline{r}')d\underline{r}' \tag{8.6}$$

The Green's tensor expressions for directly scattered light, scattered and reflected light, and scattered and transmitted light are given by eqs. 8.7 – 8.9, respectively.[170,171]

$$\hat{G}_0^{FF}(\underline{r},\underline{r}') = \frac{e^{ik_a r}}{4\pi r}\left(\hat{U} - \underline{n}\underline{n}\right)e^{-ik_a(\underline{n}\cdot\underline{r}')} \tag{8.7}$$

$$\hat{G}_r^{FF}(\underline{r},\underline{r}') = \frac{e^{ik_a r}}{4\pi r}\hat{R}e^{-ik_a(\underline{\tilde{n}}\cdot\underline{r}')} \tag{8.8}$$

$$\hat{G}_t^{FF}(\underline{r},\underline{r}') = \frac{e^{ik_t r}}{4\pi r}\hat{T}e^{-ik_a(\underline{\tilde{\tilde{n}}}\cdot\underline{r}')} \tag{8.9}$$

In the above equations, k_a is the wavevector in the region above the substrate, k_t is the wavevector in the substrate, $\underline{n} = \underline{r}/r$, $\underline{\tilde{n}} = \underline{\tilde{r}}/r$, $\underline{\tilde{\tilde{n}}} = \underline{\tilde{\tilde{r}}}/r$, $\underline{r} = (x,y,z)$, $\underline{\tilde{r}} = (x,y,-z)$, $\underline{\tilde{\tilde{r}}} = \left(x,y,-\sqrt{r^2 - \frac{n_t^2(x^2+y^2)}{n_a^2}}\right)$, and $\hat{U}$ is the identity tensor. Expressions for tensors $\hat{R}$ and $\hat{T}$ can be found in Novotny and Hecht.[171] These tensors depend only on the observation point $\underline{r}$ and the amplitude reflection and transmission coefficients of the substrate interface, accounting for the presence of any thin films, such as the SiN_x cell ARC. Inserting expressions for the Green's tensors from eqs. 8.7 – 8.9 into eqs. 8.4 – 8.6 and carrying out the integration according to Evlyukhin *et al.*[170] yields expressions for the electric fields. The field resulting from direct scattering towards point $\underline{r}$ is given in eq. 8.10.

$$\underline{E}_0(\underline{r}) = \frac{k_0^2 e^{ik_a r - \underline{n}\cdot\underline{r}_0}}{4\pi\varepsilon_0 r}\left(\left[\underline{n}\times\left[\underline{p}\times\underline{n}\right]\right] + \frac{n_a}{c}\left[\underline{m}\times\underline{n}\right] + \frac{ik_a}{6}\left[\underline{n}\times\left[\underline{n}\times\hat{Q}\underline{n}\right]\right] + \frac{ik_a n_a}{6c}\left[\underline{n}\times\hat{M}\underline{n}\right]\right) \tag{8.10}$$

Here, k_0 is the vacuum wavevector and $\underline{r}_0$ is the center of the scattering source with respect to the substrate. Expressions for scattered and reflected fields, and scattered and transmitted fields are given in eqs. 8.11 – 8.12.

$$\underline{E}_r(\underline{r}) = \frac{k_0^2 e^{ik_a r - \underline{\tilde{n}}\cdot\underline{r}_0}}{4\pi\varepsilon_0 r}\hat{R}\left\{\underline{p} - \frac{k_a}{\omega}\left[\underline{\tilde{n}}\times\underline{m}\right] - \frac{ik_a}{6}\hat{Q}\underline{\tilde{n}} + \frac{ik_a^2}{2\omega}\left[\underline{\tilde{n}}\times\hat{M}\underline{\tilde{n}}\right]\right\} \tag{8.11}$$

$$\underline{E_t}(\underline{r}) = \frac{k_0^2 e^{ik_t r - ik_a \tilde{\hat{n}} \cdot \underline{r}_0}}{4\pi\varepsilon_0 r} \hat{T} \left\{ \underline{p} - \frac{k_a}{\omega} [\tilde{\hat{n}} \times \underline{m}] - \frac{ik_a}{6} \hat{Q} \tilde{\hat{n}} + \frac{ik_a^2}{2\omega} [\tilde{\hat{n}} \times \hat{M} \tilde{\hat{n}}] \right\} \quad (8.12)$$

In eqs. 8.10– 8.12, $\underline{p}$ is the electric dipole moment, $\underline{m}$ is the magnetic dipole moment, $\hat{Q}$ is the electric quadrupole moment tensor, and $\hat{M}$ is the magnetic quadrupole moment tensor. These quantities can be determined from decomposition of the polarization field internal to the scattering source into an infinite series of multipole moments.[172–175] The dipoles and quadrupoles are the lowest order terms in this series. In this chapter, the direction and magnitude of the dipole terms are assumed and inserted into eqs. 8.10 – 8.12. The quadrupole tensors are ignored.

8.3. Idealized Backscattering and Pseudo-Ray Tracing

Out-of-phase electric and magnetic dipole moments $\underline{p}$ and $\underline{m}$ are assumed to exist with equal magnitude in an n = 1.48 material at a location $\underline{r_0}$ above a Si substrate coated with 55 nm of SiN_x. The dipoles are assumed to be strong enough to scatter all light incident on the cell at all wavelengths, and are assumed to be randomly spaced at the same height above the substrate, such that coupling effects between them can be ignored. A bi-directional scattering function $f_{scat}(\theta_1, \varphi_2, \theta_2, \lambda)$ is calculated using eqs. 10.1 – 10.12, where θ_1 is an incident angle ranging from 0° (normal to the substrate) and 90° (grazing incidence on the substrate), φ_2 is the azimuthal angle, and θ_2 is the polar angle of the scattering direction. At every incident angle θ_1, the dipole moment vectors $\underline{p}$ and $\underline{m}$ are assumed to polarize perpendicular to the incident ray, and dependence on the incident azimuthal angle is ignored. The magnitudes and relative phases of $\underline{p}$ and $\underline{m}$ are assumed to be independent of wavelength and incident angle.

The bi-directional scattering function is used to estimate the fraction of sub-bandgap light which would escape from a PV module if such scattering existed near the cell surface. For simplicity, the bi-directional scattering function is integrated over the azimuthal angle so that only the polar scattering angle is considered.

$$F_{scat}(\theta_1, \theta_2, \lambda) = \int f_{scat}(\theta_1, \varphi_2, \theta_2, \lambda)\, d\varphi_2 \quad (8.13)$$

When scattering is considered, reflection, absorption, and transmission of light is determined by a pseudo-ray tracing algorithm. A flowchart in **Figure 8.2** describes the calculations, and example results for the bi-directional scattering function $F_{scat}(\theta_1, \theta_2, \lambda)$ are given in **Figure 8.3** for several values of θ_1 and λ for the idealized scattering considered here. A ray with wavelength λ is incident on the outer glass, the probability of reflection or transmission is determined by the Fresnel reflection coefficient. If the ray is reflected, it is no longer considered. Rays which transmit through the glass can either reach the cell with incident angle θ_1 or are absorbed in the glass (3.2 mm thick) or EVA (0.4 mm thick). Upon reaching cell, all rays have their outgoing angle θ_2 randomly decided, weighted by $F_{scat}(\theta_1, \theta_2, \lambda)$. If $\theta_2 > 90°$, then the ray is considered transmitted to the cell and absorbed there. If $\theta_2 < 90°$, then the ray heads back to the surface of the module. While transmitting between the cell surface and module surface, a ray could be absorbed into the glass or EVA, with a probability determined by the Beer-Lambert Law. A ray impinging on the module surface from below has its reflection and transmission probabilities determined again by Fresnel coefficients. If transmitted, it escapes the module. If reflected, it returns again to the cell surface. It is possible for rays to be scattered into angles θ_2 where it is trapped by total internal reflection and cannot escape the module. In that event, a second scattering event would be required for the ray to escape.

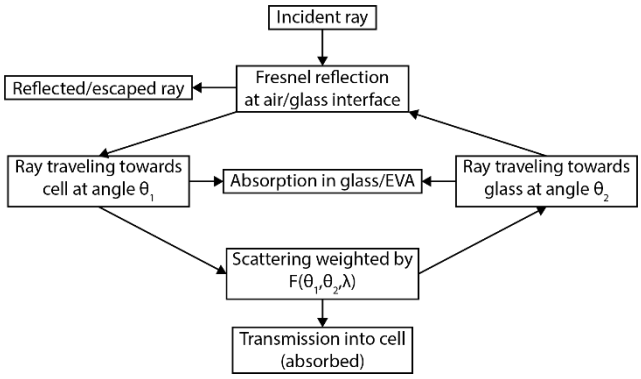

***Figure 8.2**: Flow chart of the pseudo-ray-tracing algorithm. Incident rays which transmit into the module will scatter from the cell, and back scattered light will return to the glass. The cycle repeats unless the ray is absorbed in the glass or encapsulant, scattered into the cell, or transmitted out of the module.*

At every wavelength 50,000 rays are considered, and the pseudo-ray-tracing algorithm returns the number of rays which reflect from the module, are absorbed parasitically, and escape the module after scattering. Incident light arrives at a range of

angles with respect to the module, and the fraction of light which escapes is calculated as a function of this angle. The overall escape fraction is the combination of the escape fraction at each incident angle, weighted to reflect the outdoor conditions of the full-year simulations.

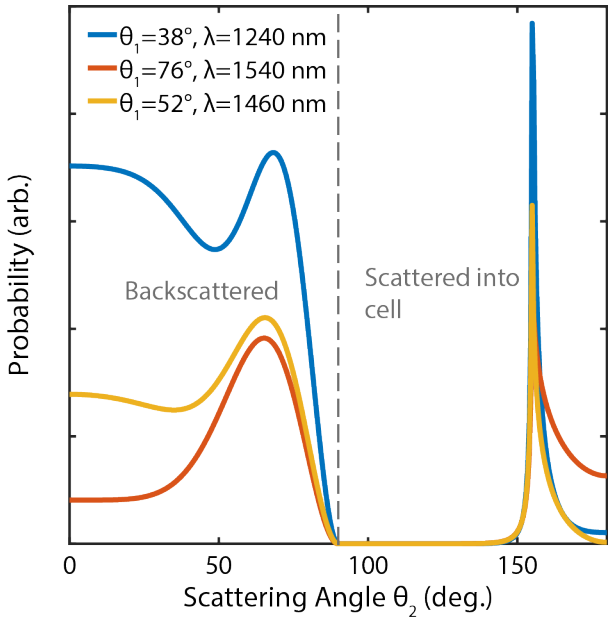

***Figure 8.3**: Examples of the bi-directional scattering function for several values of incidence angle θ_1 and incident wavelength λ in the idealized directional backscattering scenario. Regions of $\theta_2 > 90°$, where light is scattered into the cell, and $\theta_2 < 90°$, where light scatters backwards, are marked.*

8.4. Results of Idealized Scattering within the Module

The existing cell surface texture forces multiple reflections of incident light and increases transmission into the cell at all wavelengths, but, as shown previously, is detrimental to module cooling. Alternatively, application of selective backscattering at the cell surface to reduce the number of interactions with the cell surface could effectively reduce module operating temperature.

Idealized scatterers are modeled as out of phase electric and magnetic dipoles. Their overall escape fractions as a function of wavelength for several distances of the dipoles above the cell surface are shown in **Figure 8.4**, as well as the escape fraction of the baseline module. According to the results of the pseudo-ray-tracing algorithm, the greatest amount of light scatters and escapes the module when the scattering dipoles are placed 500 nm

from the cell surface. When scattering occurs in close proximity to a substrate, phase interference between waves directly scattered into a given direction, and waves which were scattered and reflected into that direction depends on the distance between the scatterer and the substrate.

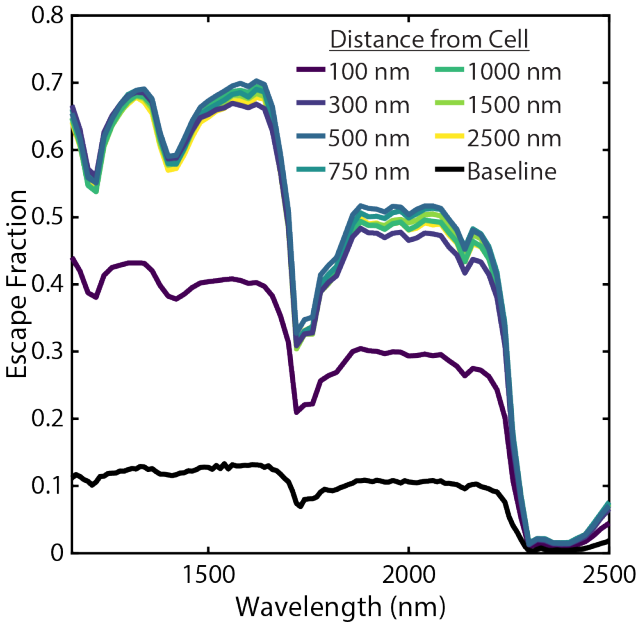

***Figure 8.4**: Escape fractions determined from the pseudo-ray-tracing algorithm for out-of-phase dipoles placed at various distances from the from the cell substrate. Once the distance reaches 300nm, the magnitude of further changes to the escape fraction decreases. The maximum is achieved at a distance of 500 nm. For comparison, the escape fraction for the Al BSF baseline module is also shown, determined from ray tracing.*

In the system of out-of-phase dipoles near the cell, the particular phase interference at a distance of 500 nm allowed more light to escape the module than any other distance investigated. In this case, either the total fraction of light backscattered was increased, or a greater fraction of light was backscattered near the normal to the module surface, such that it was unlikely to be internally reflected. Placing the dipoles at distances greater than 500 nm reduced the total amount of light escaping the module, but not by enough to increase module operating temperature by more than 0.1 K compared to the 500 nm case. However, scattering too close to the substrate allows coupling of evanescent waves above the substrate into propagating waves at oblique angles in the substrate.[171] This 'forbidden light' increases the total transmission to the cell and decreases the amount of backscattering. The

fraction of light escaping from the module when dipoles are placed only 100 nm from the cell surface is reduced for this reason.

When out-of-phase dipoles are placed 500 nm from the cell surface, the resulting decrease in parasitic absorption corresponds to a ~1.5 K reduction in annual module operating temperature, based on temperature reduction estimates of the model previously used to optimize 1-D mirrors. The 1.5 K temperature reduction given idealized scattering is approximately equivalent to the temperature reduction of a 90% reflective idealized sub-bandgap mirror at the cell surface. However, as is the case with spectrally-selective mirrors on the cell, scattering from the cell cannot prevent absorption in the glass or encapsulant, as is evident in the minima in the escape fraction in **Figure 8.4** which correspond to absorption peaks of those materials. Furthermore, while it is possible for a single scattering event to allow sub-bandgap light to escape the module, frequently light is backscattered into an angle where transmission out of the module is forbidden. While one scattering event can redirect light from the cell, multiple may be required before light escapes the module. In the idealized case considered here, the vast majority of incident light will scatter backwards upon any interaction, and, barring absorption into the glass or encapsulant, can be scattered backwards multiple times consecutively with little probability of transmitting to the cell. However, should these idealized assumptions be relaxed, the effect of multiple scattering events, each with some probability of transmission to the cell, would likely increase parasitic absorption in a similar manner to multiple reflections from a 1-D mirror.

The calculations and temperature reduction estimates discussed here form an outline for consideration of scattering near an interface in a photovoltaic module. Several studies have shown directional scattering in theory and experiment,[161–169,176] but the bandwidth of the effect is small compared to the sub-bandgap portion of the solar spectrum. Zhang *et al.*[177] have achieved unidirectional forward scattering by a single particle in two wavelength bands, and broadband forward scattering has been demonstrated for photovoltaic applications on planar Si substrates using colloidally lithographed oligomers.[178] Techniques such as these may allow broadband backscattering in practice. Additionally, it is possible to tune the angular width of directional scattering if light is incident on an array of scattering particles.[161,177] In such a design, total internal reflection of backscattered light is avoided. Fewer scattering interactions would be required before

light escapes the module in such a design compared to the out-of-phase dipoles considered here.

The analysis shown here was performed only for sub-bandgap wavelengths, but if the best possible spectral-selectivity is desired in a real design, a single set of scattering particles would simultaneously forward-scatter visible light while backscattering sub-bandgap light. However, examples of particles which satisfy forward and back scattering conditions at separate wavelengths[176,179] satisfy the forward scattering conditions at longer wavelengths. Concurrent backscattering in the sub-bandgap spectral range and forward scattering visible light may require multiple particle designs, such as one set of particles tailored for backscattering sub-bandgap light and another to forward scatter visible light. The forward scattering particle could be placed closer to the cell to enhance transmission. Ultimately, inverse design and deep-learning methods similar to those used by So *et al.*[180] may be required to realize practical broadband spectrally-selective scattering near an interface in a photovoltaic module.

8.5. Conclusions

Spectrally-selective scattering from the cell surface can redirect sub-bandgap light from the module without requiring multiple interactions. The necessary calculations to determine far-field scattering patterns including the presence of the substrate have been outlined. In the idealized scenario considered here, 1.5 K cooling is possible, similar to a 90% reflective cell mirror based on simulation results from Chapter 7. However, in terms of temperature reduction, the most effective method we have considered is spectrally-selective reflection from the outer module glass. Scattering structures near the cell are still limited by unavoidable parasitic absorption in the glass and encapsulant, and still may interact multiple times with sub-bandgap light due to internal reflection at the module surface. Tuning of the scattering profile from a particle near the cell may be possible beyond the out-of-phase electric and magnetic dipoles considered here. Still, in a realistic design scattering at all wavelength must be considered, and it is likely that scattering of visible light would interfere too much with current production to be viable without a sophisticated design. Nonetheless, the calculations outlined here may be useful in other

contexts within photovoltaics, where for example selective redirection of light is required in e.g. spectrum-splitting devices or in luminescent solar concentrators.

Chapter 9 Summary and Outlook

This thesis discusses recent work in developing passive thermal management for photovoltaic modules by spectrally-selective reflection of sub-bandgap light from the module. The designs of spectrally-selective photonic mirrors are based on models which explicitly account for outdoor irradiance and weather conditions to calculate the improvement in energy yield offered by a given mirror. Successful optimized designs require consideration of light in incident at all angles, so that proper spectral-selectivity is maintained under all outdoor conditions. Some mirror designs can achieve significant improvement in energy yield with a small number of thin-film layers. These mirrors are mostly improved anti-reflection coatings, but avoid increasing the temperature of the module even as they increase is power output. Two of these designs were fabricated, and their ability to reduce module operating temperature was demonstrated in an outdoor test. While spectrally-selective reflection or backscattering was investigated at interfaces interior to the module, the most effective mirror designs apply to the outside of the module glass.

9.1. Summary

In Chapter 2 the modeling methods used to characterize photovoltaic modules with integrated spectrally-selective mirrors was introduced. These models are informed by real weather and irradiance conditions, and so can model performance away from the standard test conditions typical of many measurements. The time-independent matrix model, the tool used for optimization of mirror design, is a streamlined model which quickly and accurately computes the effects of a photonic mirror on all energy pathways within the module, which is crucial for understanding the changes in energy yield and operating temperature.

Chapter 3 discusses some properties of optimized mirrors. Mirrors optimized for either the module outer glass or the interface between the glass and encapsulant have spectrally-selective reflection regardless of the angle of incidence. While the reflection peak wavelength blue-shifts at high angles of incidence, optimization considering all

angles ensures that light above the bandgap is not strongly reflected under any conditions. Mirrors optimized in this way efficiently collect both direct and diffuse light, contributing to ~4% increase in annual module energy yield. Optimization for only a narrow range of angles of incidence led to poor mirror performance otherwise, such that incident light at high angles was blocked from the cell, leading to a decrease in power output. Each optimized mirror serves two functions, first to reflect sub-bandgap light, and second to increase admission of useful light into the cell. Therefore, mirrors on glass stand to greatly improve absorption of light in the cell, more so than mirrors between the glass and encapsulant. While the goal of thermal management is to decrease the operating temperature, most of the energy benefit comes from improves antireflection above the bandgap for mirrors on glass.

In Chapter 4, the performance of optimized mirrors as calculated by the time-independent matrix model was compared to calculations from TOMCAT multi-physics simulations. The time-independent matrix model calculates the changes in waste heat and energy yield due to a photonic mirror. While the primary aim of the mirror is to reduce parasitic absorption in the module, the mirror affects all energy pathways in the module, including power output, and waste heat from thermalization and recombination. The increases in thermalization and recombination result from the anti-reflective effect of the mirrors, but these are more than outweighed by the decrease in parasitic absorption, leading to a net thermal benefit.

Chapter 5 discusses low-complexity mirror designs. While a larger thermal benefit is achieved by increasing the layer count to allow for a Bragg-like reflection band, low-complexity designs can still improve module energy yield, mainly through improving anti-reflection on glass. Designs with as few as two layers are considered, capable of ~1% energy improvements compared to a single layer glass ARC. The thermal aspect of the optimization gives the mirrors slightly higher reflection in the sub-bandgap range, which allows improvements in energy yield without an increase in operating temperature. These designs are simple enough to fabricate that they could lead to lower costs of photovoltaic electricity.

Chapter 6 discusses fabrication and testing of two spectrally-selective mirror designs. These mirrors, and all mirrors considered in this thesis, are designed accounting for realistic

material refractive indices, measured on thin films made using deposition techniques relevant for mirror fabrication. Therefore, the reflection expected from the optimized design is also realistic. One four-layer and one twelve-layer mirror were fabricated on glass, and integrated into test modules. Reflection measurements on the fabricated mirrors confirmed both sub-bandgap reflection and above bandgap anti-reflection. A five-week outdoor test demonstrated that both mirrored modules operated cooler than a module with a single-layer glass ARC. However, an absorbing impurity in the mirror, likely TiN_x, caused the mirrors themselves to absorb some light and decrease the module power output. If this were not the case, it is likely that both an optical and thermal benefit would have been achieved for modules including fabricated mirrors.

In Chapter 7, sub-bandgap rejection was investigated by reflection from the module interior. It was found that spectrally-selective reflection from the glass was the most beneficial in terms of maximum temperature reduction. Reflection from the cell surface is possible with high enough sub-bandgap reflection, but multiple reflection from the texture tended to decrease the overall rejection of light. Increasing the cell rear contact reflection, and decreasing its absorption, is promising for module thermal management, and is an effect of the rear passivation of PERC cells. However, any interior reflection of sub-bandgap light is limited by absorption in the glass and encapsulant. Efforts to optimize mirrors at the cell surface were unsuccessful, as simultaneous optical and thermal benefits could not be achieved. Optical benefit is also difficult to achieve at the cell surface since the SiN_x ARC is already very effective, and candidate mirror designs tended to reflect too much useful light from the cell.

Finally, Chapter 8 covers calculations related to scattering of sub-bandgap light from the cell. Highly directional scattering particles are possible through tuned electric and magnetic resonances. As shown, in an idealized scenario this can lead to significant reduction in parasitic absorption in the module. However, realizing such a design would not be simple. The problem of multiple reflections from the textured surface is partially avoided by backscattering the light, however absorption in the glass and encapsulant still limits the possible reduction in parasitic absorption. Furthermore, any real design would also scatter light at shorter wavelengths as well, which could interfere with current production. While scattering particles may not be the most useful for photovoltaic thermal

management, the ability to calculate scattering profiles near interfaces may be useful in other contexts, such as spectrum-splitting or luminescent concentrators.

9.2. Outlook

9.2.1 Modeling Spectrally-Selective Reflection for Photovoltaic Thermal Management

Sub-bandgap reflection from photovoltaic modules is a promising method to reduce their operating temperatures and increase their efficiency and power output. However, photonic structures designed for this purpose will interact will the full solar spectrum, incident at every possible angle. In Chapter 2, the time-independent matrix model was introduced, which captured changes to module optical properties caused by integration of a thin-film mirror and the effects on module temperature and energy yield considering outdoor conditions. Optimization of mirrors following this model led to effective designs which achieved a ~4% increase in annual module energy yield and ~1 K reduction in operating temperature, as discussed in Chapter 3 and Chapter 4.

Furthermore, these mirror designs are robust to changes in the location of the installed module. Thermal or optical benefits change slightly depending on the location of the installed module and the corresponding in incident weather conditions, but mirrors need not be re-optimized for each new location. Still, spectrally-selective mirrors have been designed in this thesis for specific application to mono-facial Al BSF or PERC modules. Questions remain about their potential applications in other photovoltaic technologies. Modeling efforts focused on accounting for the relative importance of light at each wavelength incident at each angle could determine the potential for spectrally-selective mirrors in the context of bifacial photovoltaic modules, for example. The ability to tune the reflection band could allow improved rear reflectors for thin-film photovoltaics or optical filters for window luminescent solar concentrators.

In a bifacial system, the module is partially transparent to sub-bandgap light, but receives light from both sides of the module. An extension of the modeling in this thesis to include rear irradiance and the transparency of the module could yield effective designs which minimize module parasitic absorption. Similarly, a luminescent solar concentrator

integrated into a building window could use a spectrally-selective filter to maintain color neutrality of transmitted light while still effectively trapping and using some sunlight for power conversion. Knowledge of the incident spectrum and desired transmitted spectrum would dictate the design of the filter in a similar manner to how the maximization of energy yield controls the designs in this thesis.

9.2.2 Reducing Energy Costs

Several mirror designs in this thesis focus on reducing the layer count while maintaining the energy benefit provided, as discussed in Chapter 5. Two such simple designs were fabricated and tested in Chapter 6. While the fabricated mirrors did have the desired spectrally-selective reflection, a reduction in the cost of energy requires not only a simple design, but also long-term performance. The five week test in this thesis does not capture potential degradation of the mirror over longer time scales, especially since the mirror is on the outside of the glass and exposed to weathering. In contrast to standard single-layer glass ARCs, where the material is porous and prone to scratching,[126] the films used in this thesis are at their full density, and potentially more resistant to scratching. However, while erosion of a single-layer glass ARC over time does reduce module energy yield, erosion of one layer of many in a thin-film stack potentially has a more severe impact if the layer removed results in increased instead of decreased reflection above the bandgap. More testing is required to determine to what degree fabricated mirrors can withstand weathering outdoors.

Additionally, the cost of depositing the mirror itself must be low enough to justify its inclusion. The fabrication methods used in Chapter 6, namely PECVD and sputtering, are amenable to industrial module production, but the costs of the mirror materials themselves were not explicitly calculated in this thesis. Estimates from the NREL LCOE calculator[181] suggest that an additional fabrication cost of up to 2 USD m^{-2} for every 1% increase in module energy yield is possible while reducing LCOE. An improved optimization model, for example, which includes the cost of materials in the calculations and minimizes the overall cost of energy would return the most useful designs. Furthermore, a reduced operating temperature could also improve the lifetime of the module, by delaying thermally activated degradation mechanisms.[4,182] Module lifetime

extension has not been probed or included in any calculations in this thesis, but could be determined with accelerated testing of modules with integrated mirrors.

9.3. Conclusions

Photovoltaic thermal management by selective reflection of sub-bandgap light is a promising way to passively cool modules under outdoor conditions. This work has developed modeling and optimization techniques capable of generating designs for photonic mirrors which achieve this cooling. These mirrors serve a dual purpose, both reflecting sub-bandgap light and admitting higher energy light into the cell, both of which increase the module energy yield. Low-complexity mirror designs have the potential to reduce the cost per Watt of photovoltaic energy, if they can be fabricated cheaply and durably enough to improve energy yield over the long term. These mirrors function effectively because they operate over all possible angles of incidence, considering the full solar spectrum. The design principles developed in this work can be used in a variety of applications to increase photovoltaic power output while reducing operating temperature.

Bibliography

(1) *The SunShot 2030 Goals: 3 Cents per Kilowatt Hour for PV and 5 Cents per Kilowatt Hour for Dispatchable CSP*; Solar Energy Technologies Office, U.S. Department of Energy, 2017.

(2) Haegel, N. M.; Atwater, H.; Barnes, T.; Breyer, C.; Burrell, A.; Chiang, Y.-M.; Wolf, S. D.; Dimmler, B.; Feldman, D.; Glunz, S.; Goldschmidt, J. C.; Hochschild, D.; Inzunza, R.; Kaizuka, I.; Kroposki, B.; Kurtz, S.; Leu, S.; Margolis, R.; Matsubara, K.; Metz, A.; Metzger, W. K.; Morjaria, M.; Niki, S.; Nowak, S.; Peters, I. M.; Philipps, S.; Reindl, T.; Richter, A.; Rose, D.; Sakurai, K.; Schlatmann, R.; Shikano, M.; Sinke, W.; Sinton, R.; Stanbery, B. J.; Topic, M.; Tumas, W.; Ueda, Y.; Lagemaat, J. van de; Verlinden, P.; Vetter, M.; Warren, E.; Werner, M.; Yamaguchi, M.; Bett, A. W. Terawatt-Scale Photovoltaics: Transform Global Energy. *Science* **2019**, *364* (6443), 836–838. https://doi.org/10.1126/science.aaw1845.

(3) Dupré, O.; Vaillon, R.; Green, M. A. Physics of the Temperature Coefficients of Solar Cells. *Sol. Energy Mater. Sol. Cells* **2015**, *140*, 92–100.

(4) Park, N. C.; Oh, W. W.; Kim, D. H. Effect of Temperature and Humidity on the Degradation Rate of Multicrystalline Silicon Photovoltaic Module https://www.hindawi.com/journals/ijp/2013/925280/ (accessed Jun 4, 2020). https://doi.org/10.1155/2013/925280.

(5) Ogbomo, O. O.; Amalu, E. H.; Ekere, N. N.; Olagbegi, P. O. Effect of Operating Temperature on Degradation of Solder Joints in Crystalline Silicon Photovoltaic Modules for Improved Reliability in Hot Climates. *Sol. Energy* **2018**, *170*, 682–693. https://doi.org/10.1016/j.solener.2018.06.007.

(6) Kurtz, S.; Whitfield, K.; TamizhMani, G.; Koehl, M.; Miller, D.; Joyce, J.; Wohlgemuth, J.; Bosco, N.; Kempe, M.; Zgonena, T. Evaluation of High-Temperature Exposure of Photovoltaic Modules. *Prog. Photovolt. Res. Appl.* **2011**, *19* (8), 954–965. https://doi.org/10.1002/pip.1103.

(7) Brovelli, L. R.; Keller, U. Simple Analytical Expressions for the Reflectivity and the Penetration Depth of a Bragg Mirror between Arbitrary Media. *Opt. Commun.* **1995**, *116* (4), 343–350. https://doi.org/10.1016/0030-4018(95)00084-L.

(8) Li, W.; Shi, Y.; Chen, K.; Zhu, L.; Fan, S. A Comprehensive Photonic Approach for Solar Cell Cooling. *ACS Photonics* **2017**, *4*, 774–782.

(9) An, Y.; Sheng, C.; Li, X. Radiative Cooling of Solar Cells: Opto-Electro-Thermal Physics and Modeling. *Nanoscale* **2019**, *11* (36), 17073–17083. https://doi.org/10.1039/C9NR04110A.

(10) Sengupta, M.; Xie, Y.; Lopez, A.; Habte, A.; Maclaurin, G.; Shelby, J. The National Solar Radiation Data Base (NSRDB). *Renew. Sustain. Energy Rev.* **2018**, *89*, 51–60. https://doi.org/10.1016/j.rser.2018.03.003.

(11) Iqbal, M. The Solar Constant and Its Spectral Distribution. In *An Introduction to Solar Radiation*; Academic Press, 1983.

(12) Hu, C. C.; White, R. M. *Solar Cells: From Basics to Advanced Systems*; McGraw-Hill, 1983.

(13) *Tables for Reference Solar Spectral Irradiances: Direct Normal and Hemispherical on 37 Tilted Surface*; ASTM International. https://doi.org/10.1520/G0173-03R12.

(14) Bird, R. E.; Hulstrom, R. L.; Lewis, L. J. Terrestrial Solar Spectral Data Sets. *Sol. Energy* **1983**, *30* (6), 563–573. https://doi.org/10.1016/0038-092X(83)90068-3.
(15) Gueymard, C. A.; Myers, D.; Emery, K. Proposed Reference Irradiance Spectra for Solar Energy Systems Testing. *Sol. Energy* **2002**, *73* (6), 443–467. https://doi.org/10.1016/S0038-092X(03)00005-7.
(16) Particles Small Compared with the Wavelength. In *Absorption and Scattering of Light by Small Particles*; John Wiley & Sons, Ltd, 2007; pp 130–157. https://doi.org/10.1002/9783527618156.ch5.
(17) Gueymard, C. Simple Model for the Atmospheric Radiative Transfer of Sunshine (SMARTS2) Algorithms and Performance Assessment. 84.
(18) Andreas, A.; Stoffel, T. *NREL Solar Radiation Research Laboratory (SRRL): Baseline Measurement System (BMS)*; NREL Report No. DA-5500-56488; 1981; p NREL Report No. DA-5500-56488.
(19) Wilcox, S.; Marion, W. *Users Manual for TMY3 Data Sets*; Dataset NREL/TP-581-43156; National Renewable Energy Laboratory: Golden, CO (United States), 2008.
(20) Holgate, S. A. *Understanding Solid State Physics*; CRC Press, 2009.
(21) Würfel, P.; Würfel, U. *Physics of Solar Cells: From Basic Principles to Advanced Concepts*; John Wiley & Sons, 2016.
(22) Kasap, S. *Springer Handbook of Electronic and Photonic Materials*; Springer Science & Business Media, 2006.
(23) Markvart, T.; Castañer, L. Principles of Solar Cell Operation. In *Solar Cells (Second Edition)*; McEvoy, A., Castañer, L., Markvart, T., Eds.; Elsevier, 2013; pp 3–25. https://doi.org/10.1016/B978-0-12-386964-7.00001-9.
(24) Yang, W. J.; Ma, Z. Q.; Tang, X.; Feng, C. B.; Zhao, W. G.; Shi, P. P. Internal Quantum Efficiency for Solar Cells. *Sol. Energy* **2008**, *82* (2), 106–110. https://doi.org/10.1016/j.solener.2007.07.010.
(25) Ananda, W. External Quantum Efficiency Measurement of Solar Cell; Institute of Electrical and Electronics Engineers Inc.: Bali, Indonesia, 2017.
(26) Gatz, S.; Müller, J.; Dullweber, T.; Brendel, R. Analysis and Optimization of the Bulk and Rear Recombination of Screen-Printed PERC Solar Cells. *Energy Procedia* **2012**, *27*, 95–102. https://doi.org/10.1016/j.egypro.2012.07.035.
(27) Lindholm, F. A.; Fossum, J. G.; Burgess, E. L. Application of the Superposition Principle to Solar-Cell Analysis. *IEEE Trans. Electron Devices* **1979**, *26* (3), 165–171. https://doi.org/10.1109/T-ED.1979.19400.
(28) Böer, K. W. The Physics of Solar Cells. *J Appl Phys* **1979**, *50*, 16.
(29) Nelson, J. *The Physics of Solar Cells*; World Scientific Publishing Company, 2003.
(30) Green, M. A. *Solar Cells: Operating Principles, Technology and System Applications*; University of New South Wales, 1986.
(31) Green, M. A.; Emery, K.; Blakers, A. W. Silicon Solar Cells with Reduced Temperature Sensitivity. *Electron. Lett.* **1982**, *18* (2), 97–98. https://doi.org/10.1049/el:19820066.
(32) Fan, J. C. C. Theoretical Temperature Dependence of Solar Cell Parameters. *Sol. Cells* **1986**, *17* (2), 309–315. https://doi.org/10.1016/0379-6787(86)90020-7.
(33) Augusto, A.; Herasimenka, S. Y.; King, R. R.; Bowden, S. G.; Honsberg, C. Analysis of the Recombination Mechanisms of a Silicon Solar Cell with Low Bandgap-Voltage Offset. *J. Appl. Phys.* **2017**, *121* (20), 205704. https://doi.org/10.1063/1.4984071.

(34) Varshni, Y. P. Temperature Dependence of the Energy Gap in Semiconductors. *Physica* **1967**, *34* (1), 149–154. https://doi.org/10.1016/0031-8914(67)90062-6.
(35) Hishikawa, Y.; Yoshita, M.; Ohshima, H.; Yamagoe, K.; Shimura, H.; Sasaki, A.; Ueda, T. Temperature Dependence of the Short Circuit Current and Spectral Responsivity of Various Kinds of Crystalline Silicon Photovoltaic Devices. *Jpn. J. Appl. Phys.* **2018**, *57* (8S3), 08RG17. https://doi.org/10.7567/JJAP.57.08RG17.
(36) Zhao, J.; Wang, A.; Robinson, S. J.; Green, M. A. Reduced Temperature Coefficients for Recent High-Performance Silicon Solar Cells. *Prog. Photovolt. Res. Appl.* **1994**, *2* (3), 221–225. https://doi.org/10.1002/pip.4670020305.
(37) Ponce-Alcántara, S.; Connolly, J. P.; Sánchez, G.; Míguez, J. M.; Hoffmann, V.; Ordás, R. A Statistical Analysis of the Temperature Coefficients of Industrial Silicon Solar Cells. *Energy Procedia* **2014**, *55*, 578–588. https://doi.org/10.1016/j.egypro.2014.08.029.
(38) Dash, P.; Gupta, N. Effect of Temperature on Power Output from Different Commercially Available Photovoltaic Modules. *Int J. Eng. Res. Appl.* **2015**, *5* (1).
(39) Kasu, M.; Abdu, J.; Hara, S.; Choi, S.; Chiba, Y.; Masuda, A. Temperature Dependence Measurements and Performance Analyses of High-Efficiency Interdigitated Back-Contact, Passivated Emitter and Rear Cell, and Silicon Heterojunction Photovoltaic Modules. *Jpn. J. Appl. Phys.* **2018**, *57* (8S3), 08RG18. https://doi.org/10.7567/JJAP.57.08RG18.
(40) Schinke, C.; Christian Peest, P.; Schmidt, J.; Brendel, R.; Bothe, K.; Vogt, M. R.; Kröger, I.; Winter, S.; Schirmacher, A.; Lim, S.; Nguyen, H. T.; MacDonald, D. Uncertainty Analysis for the Coefficient of Band-to-Band Absorption of Crystalline Silicon. *AIP Adv.* **2015**, *5* (6), 067168. https://doi.org/10.1063/1.4923379.
(41) Glunz, S. W.; Preu, R.; Biro, D. Crystalline Silicon Solar Cells: State-of-the-Art and Future Developments. In *Comprehensive Renewable Energy*; Elsevier, 2012; Vol. 1.
(42) Boehme, C.; Lucovsky, G. Origins of Silicon Solar Cell Passivation by SiNx:H Anneal. *J. Non-Cryst. Solids* **2002**, *299–302*, 1157–1161. https://doi.org/10.1016/S0022-3093(01)01135-8.
(43) Mäckel, H.; Holst, H.; Löhmann, M.; Wefringhaus, E.; Altermatt, P. P. Detailed Analysis of Random Pyramid Surfaces With Ray Tracing and Image Processing. *IEEE J. Photovolt.* **2016**, *6* (6), 1456–1465. https://doi.org/10.1109/JPHOTOV.2016.2601947.
(44) Fung, T. H.; Khan, M. U.; Zhang, Y.; Western, N. J.; Payne, D. N. R.; Mclntosh, K. R.; Abbott, M. D. Improved Ray Tracing on Random Pyramid Texture via Application of Phong Scattering. *IEEE J. Photovolt.* **2019**, *9* (3), 591–600. https://doi.org/10.1109/JPHOTOV.2019.2894688.
(45) von Roos, O. A Simple Theory of Back Surface Field (BSF) Solar Cells. *J. Appl. Phys.* **1978**, *49* (6), 3503–3511. https://doi.org/10.1063/1.325262.
(46) Blakers, A. Development of the PERC Solar Cell. *IEEE J. Photovolt.* **2019**, *9* (3), 629–635. https://doi.org/10.1109/JPHOTOV.2019.2899460.
(47) Khalil, E.; El-Batal, F.; Hamdy, Y.; Zidan, H.; Aziz, M.; Abdelghany, A. UV-Visible and IR Spectroscopic Studies of Gamma Irradiated Transition Metal Doped Lead Silicate Glasses. *Silicon* **2010**, *2*, 49–60. https://doi.org/10.1007/s12633-009-9029-8.

(48) Pern, F. J.; Czanderna, A. W. EVA Degradation Mechanisms Simulating Those in PV Modules. In *AIP Conference Proceedings*; AIP: Denver, Colorado (USA), 1992; Vol. 268, pp 445–452. https://doi.org/10.1063/1.42901.
(49) Vogt, M. R. Development of Physical Models for the Simulation of Optical Properties of Solar Cell Modules, 2015.
(50) Polman, A.; Atwater, H. A. Photonic Design Principles for Ultrahigh-Eficiency Photovoltaics. *Nat. Mater.* **2012**, *11*, 174–177.
(51) Yablonovitch, E.; Cody, G. D. Intensity Enhancement in Textured Optical Sheets for Solar Cells. *IEEE Trans. ELECTRON DEVICES* **1982**, *ED-29* (2), 300–305.
(52) Campbell, P.; Green, M. A. Light Trapping Properties of Pyramidally Textured Surfaces. *J. Appl. Phys.* **1987**, *62* (1), 243–249. https://doi.org/10.1063/1.339189.
(53) Baruch, P.; De Vos, A.; Landsberg, P. T.; Parrott, J. E. On Some Thermodynamic Aspects of Photovoltaic Solar Energy Conversion. *Sol. Energy Mater. Sol. Cells* **1995**, *36* (2), 201–222. https://doi.org/10.1016/0927-0248(95)80004-2.
(54) Griffiths, D. J. Electromagnetic Waves in Matter. In *Introduction to Electrodynamics*; Cambridge University Press, 2017.
(55) Chew, W. C. Planarly Layered Media. In *Waves and Fields in Inhomogeneous Media*; IEEE Press, 1999; pp 45–160.
(56) Subedi, I.; Silverman, T. J.; Deceglie, M. G.; Podraza, N. J. Al+Si Interface Optical Properties Obtained in the Si Solar Cell Configuration. *Phys. Status Solidi A* **2017**, *214* (12), 1700480. https://doi.org/10.1002/pssa.201700480.
(57) Shukla, A.; Kant, K.; Sharma, A.; Biwole, P. H. Cooling Methodologies of Photovoltaic Module for Enhancinh Electrical Efficiency: A Review. *Sol. Energy Mater. Sol. Cells* **2017**, *160*, 275–286.
(58) Bahaidarah, H. M. S.; Baloch, A. A. B.; Gandhidasan, P. Uniform Cooling of Photovoltaic Panels: A Review. *Renew. Sustain. Energy Rev.* **2016**, *57*, 1520–1544.
(59) Siecker, J.; Kusakana, K.; Numbi, B. P. A Review of Solar Photovoltaic Systems Cooling Technologies. *Renew. Sustain. Energy Rev.* **2017**, *79*, 192–203. https://doi.org/10.1016/j.rser.2017.05.053.
(60) Nižetić, S.; Giama, E.; Papadopoulos, A. M. Comprehensive Analysis and General Economic-Environmental Evaluation of Cooling Techniques for Photovoltaic Panels, Part II: Active Cooling Techniques. *Energy Convers. Manag.* **2018**, *155*, 301–323. https://doi.org/10.1016/j.enconman.2017.10.071.
(61) Nizetic, S.; Papdopoulos, A. M.; Giama, E. Comprehensive Analysis and General Economic-Environmental Evaluation of Cooling Techniques for Photovoltaic Panels, Part I: Passive Cooling Techniques. *Energy Convers. Manag.* **2017**, *149*, 334–354.
(62) Koehl, M.; Heck, M.; Wiesmeier, S.; Wirth, J. Modeling of the Nominal Operating Cell Temperature Based on Outdoor Weathering. *Sol. Energy Mater. Sol. Cells* **2011**, *95* (7), 1638–1646. https://doi.org/10.1016/j.solmat.2011.01.020.
(63) Schulte-Huxel, H.; Silverman, T. J.; Deceglie, M. G.; Friedman, D. J.; Tamboli, A. C. Energy Yield Analysis of Multiterminal Si-Based Tandem Solar Cells. *IEEE J. Photovolt.* **2018**, *8* (5), 1376–1383.
(64) Fraisse, G.; Ménézo, C.; Johannes, K. Energy Performance of Water Hybrid PV/T Collectors Applied to Combisystems of Direct Solar Floor Type. *Sol. Energy* **2007**, *81* (11), 1426–1438. https://doi.org/10.1016/j.solener.2006.11.017.

(65) Candanedo, L. M.; Athienitis, A.; Park, K.-W. Convective Heat Transfer Coefficients in a Building-Integrated Photovoltaic/Thermal System. *J. Sol. Energy Eng.* **2011**, *133* (2). https://doi.org/10.1115/1.4003145.
(66) Huang, M. J.; Eames, P. C.; Norton, B.; Hewitt, N. J. Natural Convection in an Internally Finned Phase Change Material Heat Sink for the Thermal Management of Photovoltaics. *Sol. Energy Mater. Sol. Cells* **2011**, *95* (7), 1598–1603. https://doi.org/10.1016/j.solmat.2011.01.008.
(67) Huang, M. J.; Eames, P. C.; Norton, B. Phase Change Materials for Limiting Temperature Rise in Building Integrated Photovoltaics. *Sol. Energy* **2006**, *80* (9), 1121–1130. https://doi.org/10.1016/j.solener.2005.10.006.
(68) Rosa-Clot, M.; Rosa-Clot, P.; Tina, G. M.; Scandura, P. F. Submerged Photovoltaic Solar Panel: SP2. *Renew. Energy* **2010**, *35* (8), 1862–1865. https://doi.org/10.1016/j.renene.2009.10.023.
(69) Anderson, W. G.; Dussinger, P. M.; Sarraf, D. B.; Tamanna, S. Heat Pipe Cooling of Concentrating Photovoltaic Cells. In *2008 33rd IEEE Photovoltaic Specialists Conference*; 2008; pp 1–6. https://doi.org/10.1109/PVSC.2008.4922577.
(70) Sun, X.; Silverman, T. J.; Zhou, Z.; Khan, M. R.; Bermel, P.; Alam, M. A. Optics-Based Approach to Thermal Management of Photovoltaics: Selective-Spectral and Radiative Cooling. *IEEE J. Photovolt.* **2017**, *7* (2), 566–574.
(71) Li, W.; Buddhiraju, S.; Fan, S. Thermodynamic Limits for Simultaneous Energy Harvesting from the Hot Sun and Cold Outer Space. *Light Sci. Appl.* **2020**, *9*, 68.
(72) Zakharchenko, R.; Licea-Jiménez, L.; Pérez-García, S. A.; Vorobiev, P.; Dehesa-Carrasco, U.; Pérez-Robles, J. F.; González-Hernández, J.; Vorobiev, Yu. Photovoltaic Solar Panel for a Hybrid PV/Thermal System. *Sol. Energy Mater. Sol. Cells* **2004**, *82* (1), 253–261. https://doi.org/10.1016/j.solmat.2004.01.022.
(73) Zhu, L.; Raman, A.; Wang, K. X.; Anoma, M. A.; Fan, S. Radiative Cooling of Solar Cells. *Optica* **2014**, *1* (1), 32–38. https://doi.org/10.1364/OPTICA.1.000032.
(74) Sun, X.; Silverman, T. J.; Zhou, Z.; Khan, M. R.; Bermel, P.; Alam, M. A. Optics-Based Approach to Thermal Management of Photovoltaics: Selective-Spectral and Radiative Cooling. *IEEE J. Photovolt.* **2017**, *7* (2), 566–574. https://doi.org/10.1109/JPHOTOV.2016.2646062.
(75) Zhu, L.; Raman, A.; Fan, S. Color-Preserving Daytime Radiative Cooling. *Appl. Phys. Lett.* **2013**, *103* (22), 223902. https://doi.org/10.1063/1.4835995.
(76) Rephaeli, E.; Raman, A.; Fan, S. Ultrabroadband Photonic Structures To Achieve High-Performance Daytime Radiative Cooling. *Nano Lett.* **2013**, *13* (4), 1457–1461. https://doi.org/10.1021/nl4004283.
(77) Rubin, M. Optical Properties of Soda Lime Silica Glasses. *Sol. Energy Mater.* **1985**, *12* (4), 275–288. https://doi.org/10.1016/0165-1633(85)90052-8.
(78) Zhao, B.; Hu, M.; Ao, X.; Xuan, Q.; Pei, G. Spectrally Selective Approaches for Passive Cooling of Solar Cells: A Review. *Appl. Energy* **2020**, *262*, 114548. https://doi.org/10.1016/j.apenergy.2020.114548.
(79) Sheppard, C. J. R. Approximate Calculation of the Reflection Coefficient from a Stratified Medium. *Pure Appl. Opt. J. Eur. Opt. Soc. Part A* **1995**, *4* (5), 665–669. https://doi.org/10.1088/0963-9659/4/5/018.
(80) Ibrahim, H.; Anani, N. Variations of PV Module Parameters with Irradiance and Temperature. *Energy Procedia* **2017**, *134*, 276–285.

(81) Mahmoud, Y.; Xiao, W.; Zeineldin, H. H. A Simple Approach to Modeling and Simulation of Photovoltaic Modules. *IEEE Trans. Sustain. Energy* **2012**, *3* (1), 185–186.
(82) Aljoaba, S. Z.; Cramer, A. M.; Walcott, B. L. Thermoelectrical Modeling of Wavelength Effects on Photovoltaic Module Performance-Part I: Model. *IEEE J. Photovolt.* **2013**, *3* (3), 1027–1033.
(83) Baenas, T.; Machado, M. Optical Model for Multilayer Glazing Systems: Application to Laminated Glass and Photovoltaic Modules. *Sol. Energy* **2016**, *125*, 256–266.
(84) Hamed, H.; Pfau, C.; Turek, M.; Schneider, J. A Practical Optical and Electrical Model to Estimate the Power Losses and Quantification of Different Heat Sources in Silicon Based PV. *Renew. Energy* **2018**, *127*, 602–612.
(85) de la Parra, I.; Muñoz, M.; Lorenzo, E.; García, M.; Marcos, J.; Martínez-Moreno, F. PV Performance Modelling: A Review in the Light of Quality Assurance for Large PV Plants. *Renew. Sustain. Energy Rev.* **2017**, *78*, 780–797. https://doi.org/10.1016/j.rser.2017.04.080.
(86) Ba, M.; Ramenah, H.; Tanougast, C. Forseeing Energy Photovoltaic Output Determination by a Statistical Model Using Real Module Temperature in the North East of France. *Renew. Energy* **2018**, *119*, 935–948.
(87) Abdolzadeh, M.; Zarei, T. Optical and Thermal Modeling of a Photovoltaic Module and Experimental Evaluation of the Modeling Performance. *Environ. Prog. Sustain. Energy* **2017**, *36* (1), 277–293.
(88) Fernandez, E. F.; Pérez-Higueras, P.; Almonacid, F.; Ruiz-Arias, J. A. Model for Estimating the Energy Yield of a High Concentrator Photovoltaic System. *Energy* **2015**, *87*, 77–85.
(89) Duck, B. C.; Fell, C. J.; Anderson, K. F.; Sacchetta, C.; Du, Y.; Zhu, Y. Determining the Value of Cooling in Photovoltaic for Enhanced Energy Yield. *Sol. Energy* **2018**, *159*, 337–345.
(90) Vaillon, R.; Dupré, O.; Cal, R. B.; Calaf, M. Pathways for Mitigating Thermal Losses in Solar Photovoltaics. *Sci. Rep.* **2018**, *8*, 13163.
(91) *COMSOL Multiphysics*; COMSOL AB: Stockholm, Sweden, 2018.
(92) Silverman, T. J.; Deceglie, M. G.; Subedi, I.; Podraza, N. J.; Slauch, I. M.; Ferry, V. E.; Repins, I. Reducing Operating Temperature in Photovoltaic Modules. *IEEE J. Photovolt.* **2018**, *8* (2), 532–540. https://doi.org/10.1109/JPHOTOV.2017.2779842.
(93) Reda, I.; Andreas, A. *Solar Position Algorithm for Solar Radiation Applications (Revised)*; NREL/TP-560-34302, 15003974; 2008; p NREL/TP-560-34302, 15003974. https://doi.org/10.2172/15003974.
(94) Mondol, J. D.; Yohanis, Y. G.; Norton, B. Solar Radiation Modelling for the Simulation of Photovoltaic Systems. *Renew. Energy* **2008**, *33* (5), 1109–1120. https://doi.org/10.1016/j.renene.2007.06.005.
(95) Monteith, J.; Unsworth, M. *Principles of Environmental Physics - 3rd Edition*, 3rd Edition.; Academic Press, 2007.
(96) Murray, F. W. On the Computation of Saturation Vapor Pressure. *J. Appl. Meteorol.* **1967**, *6* (1), 203–204. https://doi.org/10.1175/1520-0450(1967)006<0203:OTCOSV>2.0.CO;2.
(97) *SunSolve*; PVLigthouse. https://www.pvlighthouse.com.au.

(98) Lucarini, V.; Peiponen, K.-E.; Saarinen, J. J.; Vartiainen, E. M. Kramers-Kronig Relations in Optical Materials Research. *Kramers-Kronig Relat. Opt. Mater. Res. V Lucarini J Saarinen K Peiponen E Vartiainen X 162 P 37 Illus 3-540-23673-2 Berl. Springer 2005* **2005**. https://doi.org/10.1007/b138913.
(99) Pedrotti, F. L.; Pedrotti, L. S. *Introduction to Optics*; Englewood Cliffs, N.J. : Prentice Hall, 1993.
(100) Blinn, J. F. Models of Light Reflection for Computer Synthesized Pictures. *ACM SIGGRAPH Comput. Graph.* **1977**, *11* (2), 192–198. https://doi.org/10.1145/965141.563893.
(101) Vogt, M. R.; Hahn, H.; Holst, H.; Winter, M.; Schinke, C.; Köntges, M.; Brendel, R.; Altermatt, P. P. Measurement of the Optical Constants of Soda-Lime Glasses in Dependence of Iron Content and Modeling of Iron-Related Power Losses in Crystalline Si Solar Cell Modules. *IEEE J. Photovolt.* **2016**, *6* (1), 111–118. https://doi.org/10.1109/JPHOTOV.2015.2498043.
(102) Vogt, M. R.; Holst, H.; Schulte-Huxel, H.; Blankemeyer, S.; Witteck, R.; Hinken, D.; Winter, M.; Min, B.; Schinke, C.; Ahrens, I.; Köntges, M.; Bothe, K.; Brendel, R. Optical Constants of UV Transparent EVA and the Impact on the PV Module Output Power under Realistic Irradiation. *Energy Procedia* **2016**, *92*, 523–530. https://doi.org/10.1016/j.egypro.2016.07.136.
(103) Urrejola, E.; Peter, K.; Plagwitz, H.; Schubert, G. Silicon Diffusion in Aluminum for Rear Passivated Solar Cells. *Appl. Phys. Lett.* **2011**, *98* (15), 153508. https://doi.org/10.1063/1.3579541.
(104) Herzinger, C. M.; Johs, B.; McGahan, W. A.; Woollam, J. A.; Paulson, W. Ellipsometric Determination of Optical Constants for Silicon and Thermally Grown Silicon Dioxide via a Multi-Sample, Multi-Wavelength, Multi-Angle Investigation. *J. Appl. Phys.* **1998**, *83* (6), 3323–3336. https://doi.org/10.1063/1.367101.
(105) Baker-Finch, S. C.; McIntosh, K. R.; Yan, D.; Fong, K. C.; Kho, T. C. Near-Infrared Free Carrier Absorption in Heavily Doped Silicon. *J. Appl. Phys.* **2014**, *116* (6), 063106. https://doi.org/10.1063/1.4893176.
(106) *Free-Carrier Absorption Calculator*; PVLighthouse, 2014.
(107) *Refractive Index Library, Material: Glass, Low-Fe Sodalime [Pil]*; Dataset; PV Lighthouse.
(108) Vogt, M. R.; Holst, H.; Schulte-Huxel, H.; Blankemeyer, S.; Witteck, R.; Hinken, D.; Winter, M.; Min, B.; Schinke, C.; Ahrens, I.; Kontges, M.; Bothe, K.; Brendel, R. Optical Constants of UV Transparent EVA and the Impact on the PV Module Output Power under Realistic Irradiation. *Energy Procedia* **2016**, *2*, 523–530.
(109) Krauter, S. C. W. Energy Yield. In *Solar Electric Power Generation*; Springer, 2006.
(110) Magare, D.; Sastry, O.; Gupta, R.; Bora, B.; Singh, Y.; Mohammed, H. Wind Effect Modeling and Analysis for Estimation of Photovoltaic Module Temperature. *J. Sol. Energy Eng.* **2017**, *140* (1), 011008.
(111) Coskun, C.; Toygar, U.; Sarpdag, O.; Oktay, Z. Sensitivity Analysis of Implicit Correlations for Photovoltaic Module Temperature: A Review. *J. Clean. Prod.* **2017**, *164*, 1474–1485.

(112) Guldin, S. Optical Aspects of Thin Films and Interfaces. In *Inorganic Nanoarchitectures by Organic Self-Assembly*; Springer Theses; Springer International Publishing: Switzerland, 2013.
(113) Schinke, C.; Peest, P. C.; Schmidt, J.; Brendel, R.; Bothe, K.; Vogt, M. R.; Kroger, I.; Winter, S.; Schirmacher, A.; Lim, S.; Nguyen, H. T.; MacDonald, D. Uncertainty Analysis for the Coefficient of Band-to-Band Absorption of Crystalline Silicon. *AIP Adv.* **2015**, *5*, 067168.
(114) Herzinger, C. M.; Johs, B.; McGahan, W. A.; Woollam, J. A.; Paulson, W. Ellipsometric Determination of Optical Constants for Silicon and Thermally Grown Silicon Dioxide via a Multiple-Sample, Multi-Wavelength, Multi-Angle Investigation. *J. Appl. Phys.* **1998**, *83* (6), 3323.
(115) Rakic, A. D.; Djurisic, A. B.; Elazar, J. M.; Majewski, M. L. Optical Properties of Metallic Films for Vertical-Cavity Optoelectronic Devices. *Appl. Opt.* **1998**, *37* (22), 5271–5283.
(116) Tool, C. J. J.; Coletti, G.; Granek, F. J.; Hoornstra, J.; Koppes, M.; Kossen, E. J.; Rieffe, H. C.; Romijn, I. G.; Weeber, A. W. 17% Mc-Si Solar Cell Efficiency Using Full in-Line Processing with Improved Texturing and Screen-Printed Contacts on High-Ohmic Emitters. In *Proceedings of the 20th EU PVSEC 2005*; Barcelona, Spain, 2005.
(117) Schulte-Huxel, H.; Silverman, T. J.; Deceglie, M. G.; Friedman, D. J.; Tamboli, A. C. Energy Yield Analysis of Multiterminal Si Based Tandem Solar Cells. *IEEE J. Photovolt.* **2018**, *8* (5), 1376–1383.
(118) The ALLMAX M Plus Module Datasheet. Trina Solar 2016.
(119) Baker-Finch, S. C.; McIntosh, K. R.; Yan, D.; Fong, K. C.; Kho, T. C. Near-Infrared Free Carrier Absorption in Heavily Doped Silicon. *J. Appl. Phys.* **2014**, *116*, 063106.
(120) Subedi, I.; Silverman, T. J.; Deceglie, M. G.; Podraza, N. J. Ultraviolet to Infrared Spectral Range Optical Modeling of PERC Silicon Solar Cells. *IEEE J. Photovolt.* **2019**, In Review.
(121) Nelder, J. A.; Mead, R. A Simplex Method for Function Minimization. *Comput. J.* **1965**, *7* (4), 308–313. https://doi.org/10.1093/comjnl/7.4.308.
(122) Tikhonravov, A. V.; Trubetskov, M. K.; DeBell, G. W. Application of the Needle Optimization Technique to the Design of Optical Coatings. *Appl. Opt.* **1996**, *35* (28), 5493–5508. https://doi.org/10.1364/AO.35.005493.
(123) Sprafke, A. N.; Wehrspohn, R. B. Current Concepts for Optical Path Enhancement in Solar Cells. In *Photon Management in Solar Cells*; John Wiley & Sons, Ltd, 2015; pp 1–20. https://doi.org/10.1002/9783527665662.ch1.
(124) Passias, D.; Källbäck, B. Shading Effects in Rows of Solar Cell Panels. *Sol. Cells* **1984**, *11* (3), 281–291. https://doi.org/10.1016/0379-6787(84)90017-6.
(125) Knapp, C. L. Insolation Data Manual: Long-Term Monthly Averages of Solar Radiation, Temperature, Degree-Days, and Global Kt for 248 National Weather Service Stations. 295.
(126) Vogt, M. R. Development of Physical Models for the Simulation of Optical Properties of Solar Cell Modules. PhD, Leibniz University of Hanover, Hanover, Germany, 2015.

(127) Markvart, T.; Castaner, L. Solar Radiation. In *Practical Handbook of Photovoltaics: Fundamentals and applications*; Elsevier, 2011.
(128) Incropera, F. P.; Dewitt, D. P.; Bergman, T. L.; Lavine, A. S. External Flow. In *Fundamentals of Heat and Mass Transfer*; John Wiley and Sons, 2007.
(129) Jubayer, C. M.; Siddiqui, K.; Hangan, H. CFD Analysis of Convective Heat Transfer from Ground Mounted Solar Panels. *Sol. Energy* **2016**, *133*, 556–566.
(130) Marinic-Kragic, I.; Nizetic, S.; Grubisic-Cabo, F.; Papadopoulos, A. M. Analysis of Flow Separation Effect in the Case of Free-Standing Photovoltaic Panel Exposed to Various Operating Conditions. *J. Clean. Prod.* **2018**, *174*, 53–64.
(131) Kost, C.; Shammugam, S.; Jülch, V.; Nguyen, H.-T.; Schlegl, T. Levelized Cost of Electricity- Renewable Energy Technologies. 42.
(132) Woodhouse, M.; Feldman, D.; Fu, R.; Horowitz, K.; Chung, D. On the Path to SunShot: The Role of Advancements in Solar Photovoltaic Efficiency, Reliability, and Costs. 44.
(133) Jones-Albertus, R.; Feldman, D.; Fu, R.; Horowitz, K.; Woodhouse, M. Technology Advances Needed for Photovoltaics to Achieve Widespread Grid Price Parity: Widespread Grid Price Parity for Photovoltaics. *Prog. Photovolt. Res. Appl.* **2016**, *24* (9), 1272–1283. https://doi.org/10.1002/pip.2755.
(134) Marcos, L. V. R.; Larruquert, J. I.; Méndez, J. A.; Aznárez, J. A. Self-Consistent Optical Constants of MgF_2, LaF_3, and CeF_3 Films. *Opt. Mater. Express* **2017**, *7* (3), 989–1006. https://doi.org/10.1364/OME.7.000989.
(135) Raut, H. K.; Ganesh, V. A.; Nair, A. S.; Ramakrishna, S. Anti-Reflective Coatings: A Critical, in-Depth Review. *Energy Environ. Sci.* **2011**, *4* (10), 3779–3804. https://doi.org/10.1039/C1EE01297E.
(136) Wohlgemuth, J. H. Standards for PV Modules and Components – Recent Developments and Challenges: Preprint. 7.
(137) Mkasi, H. W.; May, S. I.; Basappa Ayanna, M.; Pratt, L. E.; Roro, K. T. *Characterization of Solar Photovoltaic Modules in Outdoor and Indoor Conditions*; CIGRE Southern Africa National Committee, 2019.
(138) Ransome, S. Validating Energy Yield Modelling with the NREL Outdoor Dataset. In *2018 IEEE 7th World Conference on Photovoltaic Energy Conversion (WCPEC) (A Joint Conference of 45th IEEE PVSC, 28th PVSEC 34th EU PVSEC)*; 2018; pp 2713–2718. https://doi.org/10.1109/PVSC.2018.8548135.
(139) Santiago, I.; Trillo-Montero, D.; Moreno-Garcia, I. M.; Pallarés-López, V.; Luna-Rodríguez, J. J. Modeling of Photovoltaic Cell Temperature Losses: A Review and a Practice Case in South Spain. *Renew. Sustain. Energy Rev.* **2018**, *90*, 70–89. https://doi.org/10.1016/j.rser.2018.03.054.
(140) Ali, H. M.; Mahmood, M.; Bashir, M. A.; Ali, M.; Siddiqui, A. M. Outdoor Testing of Photovoltaic Modules during Summer in Taxila, Pakistan. *Therm. Sci.* **2016**, *20* (1), 165–173.
(141) Hüttl, B.; Gottschalk, L.; Schneider, S.; Pflaum, D.; Schulze, A. Accurate Performance Rating of Photovoltaic Modules under Outdoor Test Conditions. *Sol. Energy* **2019**, *177*, 737–745. https://doi.org/10.1016/j.solener.2018.12.002.
(142) Meflah, A.; Rahmoun, K.; Mahrane, A.; Chikh, M. Outdoor Performance Modeling of Three Different Silicon Photovoltaic Module Technologies. *Int. J. Energy Environ. Eng.* **2017**, *8* (2), 143–152. https://doi.org/10.1007/s40095-017-0228-6.

(143) Azzam, R. M. A.; Bashara, N. M. *Ellipsometry and Polarized Light*; North-Holland Pub. Co., 1977.
(144) Ohlídal, I.; Franta, D. Ellipsometry of Thin Film Systems. In *Progress in Optics*; Wolf, E., Ed.; Elsevier, 2000; Vol. 41, pp 181–282. https://doi.org/10.1016/S0079-6638(00)80018-9.
(145) Jenkins, F.; White, H. *Fundamentals of Optics*, Fourth Edition.; McGraw-Hill, 1981.
(146) Dow, J. D.; Redfield, D. Toward a Unified Theory of Urbach's Rule and Exponential Absorption Edges. *Phys. Rev. B* **1972**, *5* (2), 594–610. https://doi.org/10.1103/PhysRevB.5.594.
(147) Siefke, T.; Kroker, S.; Pfeiffer, K.; Puffky, O.; Dietrich, K.; Franta, D.; Ohlídal, I.; Szeghalmi, A.; Kley, E.-B.; Tünnermann, A. Materials Pushing the Application Limits of Wire Grid Polarizers Further into the Deep Ultraviolet Spectral Range. *Adv. Opt. Mater.* **2016**, *4* (11), 1780–1786. https://doi.org/10.1002/adom.201600250.
(148) Sarkar, S.; Gupta, V.; Kumar, M.; Schubert, J.; Probst, P. T.; Joseph, J.; König, T. A. F. Hybridized Guided-Mode Resonances via Colloidal Plasmonic Self-Assembled Grating. *ACS Appl. Mater. Interfaces* **2019**, *11* (14), 13752–13760. https://doi.org/10.1021/acsami.8b20535.
(149) General Oscillator Layer. In *Guide to Using WVASE(R) Spectroscopic Ellipsometry Data Ascqusition and Analysis Software*; J. A. Woollam Co., Inc.: Lincoln, NE, USA.
(150) Pflüger, J.; Fink, J.; Weber, W.; Bohnen, K. P.; Crecelius, G. Dielectric Properties of TiC_x, TiN_x, VC_x, and VN_x from 1.5 to 40 EV Determined by Electron-Energy-Loss Spectroscopy. *Phys. Rev. B* **1984**, *30* (3), 1155–1163. https://doi.org/10.1103/PhysRevB.30.1155.
(151) Baker-Finch, S. C.; McIntosh, K. R. Reflection of Normally Incident Light from Silicon Solar Cells with Pyramidal Texture. *Prog. Photovolt. Res. Appl.* **2011**, *19* (4), 406–416. https://doi.org/10.1002/pip.1050.
(152) Nussbaumer, H.; Willeke, G.; Bucher, E. Optical Behavior of Textured Silicon. *J. Appl. Phys.* **1994**, *75* (4), 2202–2209. https://doi.org/10.1063/1.356282.
(153) Ingenito, A.; Luxembourg, S. L.; Spinelli, P.; Liu, J.; Ortiz Lizcano, J. C.; Weeber, A. W.; Isabella, O.; Zeman, M. Optimized Metal-Free Back Reflectors for High-Efficiency Open Rear c-Si Solar Cells. *IEEE J. Photovolt.* **2016**, *6* (1), 34–40. https://doi.org/10.1109/JPHOTOV.2015.2487827.
(154) Vogt, M. R.; Schulte-Huxel, H.; Offer, M.; Blankemeyer, S.; Witteck, R.; Köntges, M.; Bothe, K.; Brendel, R. Reduced Module Operating Temperature and Increased Yield of Modules With PERC Instead of Al-BSF Solar Cells. *IEEE J. Photovolt.* **2017**, *7* (1), 44–50. https://doi.org/10.1109/JPHOTOV.2016.2616191.
(155) Holman, Z. C.; Filipič, M.; Lipovšek, B.; De Wolf, S.; Smole, F.; Topič, M.; Ballif, C. Parasitic Absorption in the Rear Reflector of a Silicon Solar Cell: Simulation and Measurement of the Sub-Bandgap Reflectance for Common Dielectric/Metal Reflectors. *Sol. Energy Mater. Sol. Cells* **2014**, *120*, 426–430. https://doi.org/10.1016/j.solmat.2013.06.024.
(156) Wang, Z.; Han, P.; Lu, H.; Qian, H.; Chen, L.; Meng, Q.; Tang, N.; Gao, F.; Jiang, Y.; Wu, J.; Wu, W.; Zhu, H.; Ji, J.; Shi, Z.; Sugianto, A.; Mai, L.; Hallam, B.; Wenham, S. Advanced PERC and PERL Production Cells with 20.3% Record

Efficiency for Standard Commercial p-Type Silicon Wafers. *Prog. Photovolt. Res. Appl.* **2012**, *20* (3), 260–268. https://doi.org/10.1002/pip.2178.
(157) Pfann, W. G.; Van Roosbroeck, W. Radioactive and Photoelectric *P-n* Junction Power Sources. *J. Appl. Phys.* **1954**, *25* (11), 1422–1434. https://doi.org/10.1063/1.1721579.
(158) Kerker, M.; Wang, D.-S.; Giles, C. L. Electromagnetic Scattering by Magnetic Spheres. *JOSA* **1983**, *73* (6), 765–767. https://doi.org/10.1364/JOSA.73.000765.
(159) Alù, A.; Engheta, N. The Quest for Magnetic Plasmons at Optical Frequencies. *Opt. Express* **2009**, *17* (7), 5723–5730. https://doi.org/10.1364/OE.17.005723.
(160) Krasnok, A. E.; Miroshnichenko, A. E.; Belov, P. A.; Kivshar, Y. S. All-Dielectric Optical Nanoantennas. *Opt. Express* **2012**, *20* (18), 20599–20604. https://doi.org/10.1364/OE.20.020599.
(161) Sikdar, D.; Cheng, W.; Premaratne, M. Optically Resonant Magneto-Electric Cubic Nanoantennas for Ultra-Directional Light Scattering. *J. Appl. Phys.* **2015**, *117* (8), 083101. https://doi.org/10.1063/1.4907536.
(162) Shibanuma, T.; Matsui, T.; Roschuk, T.; Wojcik, J.; Mascher, P.; Albella, P.; Maier, S. A. Experimental Demonstration of Tunable Directional Scattering of Visible Light from All-Dielectric Asymmetric Dimers. *ACS Photonics* **2017**, *4* (3), 489–494. https://doi.org/10.1021/acsphotonics.6b00979.
(163) Albella, P.; Shibanuma, T.; Maier, S. A. Switchable Directional Scattering of Electromagnetic Radiation with Subwavelength Asymmetric Silicon Dimers. *Sci. Rep.* **2015**, *5* (1), 1–8. https://doi.org/10.1038/srep18322.
(164) Luk'yanchuk, B. S.; Voshchinnikov, N. V.; Paniagua-Domínguez, R.; Kuznetsov, A. I. Optimum Forward Light Scattering by Spherical and Spheroidal Dielectric Nanoparticles with High Refractive Index. *ACS Photonics* **2015**, *2* (7), 993–999. https://doi.org/10.1021/acsphotonics.5b00261.
(165) Fu, Y. H.; Kuznetsov, A. I.; Miroshnichenko, A. E.; Yu, Y. F.; Luk'yanchuk, B. Directional Visible Light Scattering by Silicon Nanoparticles. *Nat. Commun.* **2013**, *4* (1), 1–6. https://doi.org/10.1038/ncomms2538.
(166) Tsuchimoto, Y.; Yano, T.; Hayashi, T.; Hara, M. Fano Resonant All-Dielectric Core/Shell Nanoparticles with Ultrahigh Scattering Directionality in the Visible Region. *Opt. Express* **2016**, *24* (13), 14451–14462. https://doi.org/10.1364/OE.24.014451.
(167) Naraghi, R. R.; Sukhov, S.; Dogariu, A. Directional Control of Scattering by All-Dielectric Core-Shell Spheres. *Opt. Lett.* **2015**, *40* (4), 585–588. https://doi.org/10.1364/OL.40.000585.
(168) Alaee, R.; Filter, R.; Lehr, D.; Lederer, F.; Rockstuhl, C. A Generalized Kerker Condition for Highly Directive Nanoantennas. *Opt. Lett.* **2015**, *40* (11), 2645–2648. https://doi.org/10.1364/OL.40.002645.
(169) Pors, A.; Andersen, S. K. H.; Bozhevolnyi, S. I. Unidirectional Scattering by Nanoparticles near Substrates: Generalized Kerker Conditions. *Opt. Express* **2015**, *23* (22), 28808–28828. https://doi.org/10.1364/OE.23.028808.
(170) Evlyukhin, A. B.; Reinhardt, C.; Evlyukhin, E.; Chichkov, B. N. Multipole Analysis of Light Scattering by Arbitrary-Shaped Nanoparticles on a Plane Surface. *JOSA B* **2013**, *30* (10), 2589–2598. https://doi.org/10.1364/JOSAB.30.002589.

(171) Novotny, L.; Hecht, B. *Principles of Nano-Optics*; EngineeringPro; Cambridge University Press: Cambridge, U.K. ; New York, 2006.
(172) Alaee, R.; Rockstuhl, C.; Fernandez-Corbaton, I. An Electromagnetic Multipole Expansion beyond the Long-Wavelength Approximation. *Opt. Commun.* **2018**, *407*, 17–21. https://doi.org/10.1016/j.optcom.2017.08.064.
(173) Raab, R. E. *Multipole Theory in Electromagnetism: Classical, Quantum, and Symmetry Aspects, with Applications*; International series of monographs on physics (Oxford, England) 128; Clarendon Press ; Oxford University Press: Oxford : New York, 2005.
(174) John David Jackson. *Classical Electrodynamics*, 3rd ed..; Wiley: New York, 1999.
(175) Papas, C. H. *Theory of Electromagnetic Wave Propagation.*; McGraw-Hill physical and quantum electronics series; McGraw-Hill: New York, 1965.
(176) Geffrin, J. M.; García-Cámara, B.; Gómez-Medina, R.; Albella, P.; Froufe-Pérez, L. S.; Eyraud, C.; Litman, A.; Vaillon, R.; González, F.; Nieto-Vesperinas, M.; Sáenz, J. J.; Moreno, F. Magnetic and Electric Coherence in Forward- and Back-Scattered Electromagnetic Waves by a Single Dielectric Subwavelength Sphere. *Nat. Commun.* **2012**, *3* (1), 1–8. https://doi.org/10.1038/ncomms2167.
(177) Zhang, X. M.; Zhang, Q.; Zeng, S. J.; Liu, Z. Z.; Xiao, J.-J. Dual-Band Unidirectional Forward Scattering with All-Dielectric Hollow Nanodisk in the Visible. *Opt. Lett.* **2018**, *43* (6), 1275–1278. https://doi.org/10.1364/OL.43.001275.
(178) Zhang, Y.; Xu, Y.; Chen, S.; Lu, H.; Chen, K.; Cao, Y.; Miroshnichenko, A. E.; Gu, M.; Li, X. Ultra-Broadband Directional Scattering by Colloidally Lithographed High-Index Mie Resonant Oligomers and Their Energy-Harvesting Applications. *ACS Appl. Mater. Interfaces* **2018**, *10* (19), 16776–16782. https://doi.org/10.1021/acsami.8b03718.
(179) Li, Y.; Wan, M.; Wu, W.; Chen, Z.; Zhan, P.; Wang, Z. Broadband Zero-Backward and near-Zero-Forward Scattering by Metallo-Dielectric Core-Shell Nanoparticles. *Sci. Rep.* **2015**, *5* (1), 1–12. https://doi.org/10.1038/srep12491.
(180) So, S.; Mun, J.; Rho, J. Simultaneous Inverse Design of Materials and Parameters of Core-Shell Nanoparticle via Deep-Learning: Demonstration of Dipole Resonance Engineering. *ArXiv190402848 Phys.* **2019**.
(181) Silverman, T. J.; Deceglie, M. G.; Kelsey A. Horowitz. *NREL Comparative PV LCOE Calculator*; 2018.
(182) Kurtz, S.; Whitfield, K.; Miller, D.; Joyce, J.; Wohlgemuth, J.; Kempe, M.; Dhere, N.; Bosco, N.; Zgonena, T. Evaluation of High-Temperature Exposure of Rack-Mounted Photovoltaic Modules. In *2009 34th IEEE Photovoltaic Specialists Conference (PVSC)*; 2009; pp 002399–002404. https://doi.org/10.1109/PVSC.2009.5411307.

Appendix

Scanning Probe Microscopy Measurements

The pyramidal texture of a bare c-Si Al-BSF cell was analyzed using a Keysight 5500 environmental Scanning Probe Microscope (SPM). Measurements were made at room temperature and standard pressure; the sample chamber was purged with nitrogen prior to measurement. The scan area was 30 µm x 30 µm, with a resolution of 512 pixels per line, giving a resolution of 59 nm per pixel. From the raw height measurement $z(x, y)$, the local slope, S, was calculated using eq. A1.

$$S = \tan^{-1}\left(\sqrt{\left(\frac{\partial z}{\partial x}\right)^2 + \left(\frac{\partial z}{\partial y}\right)^2}\right) \quad \text{(A1)}$$

The distribution of slopes calculated from the cell texture measurement was used to inform the optical models for each photovoltaic module. **Figure A1** shows the distribution of slopes and the raw z-height measurement results.

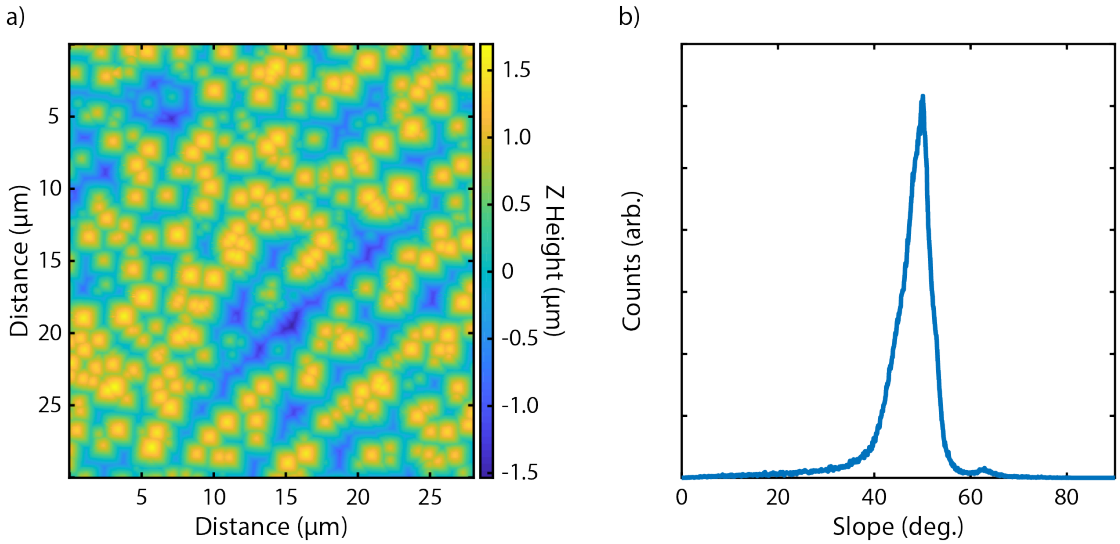

***Figure A1**: a) Z(x,y) results from SPM of a textured c-Si Al BSF solar cell. The scan area was 30 µm x 30 µm, a 28 µm x 30 µm area is shown as some data was ignored due to transient error. b) Histogram of local slopes measured using nearest neighbor points on the height map, with no additional data filtering.*

Sky and Ground Temperature Correlations

The NREL Solar Radiation Research Laboratory and Baseline Measurement System (SRRL BMS) records sky and ground temperature by measuring longwave IR radiation using longwave pyrgeometers and back calculation using the Stefan-Boltzmann Law. To

apply the full TOMCAT simulation at locations other than Golden, CO, sky and ground temperatures must be estimated based on other weather data. **Figure A2** shows a scatter plot of the correlations (eqs. 2.4 and 2.6 in the main text) and the measured values, both using weather data from SRRL BMS over a one year time span.

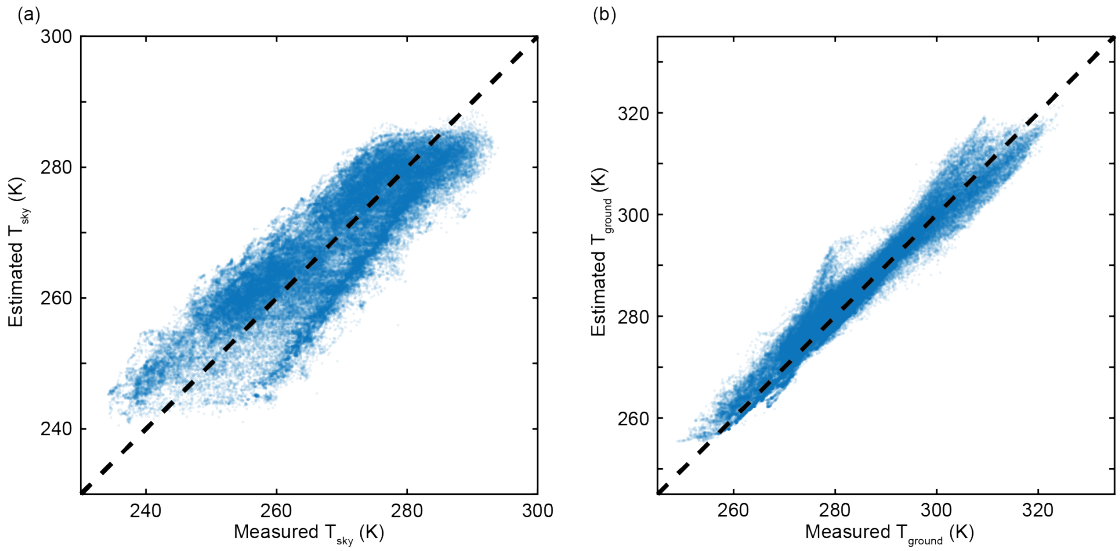

***Figure A2**: Scatter plots showing measured versus estimated values of (a) T_{sky} and (b) T_{ground}.*

Reflection from the SiN_x Cell ARC

Model agreement with simulation relies on accurate characterization of all module components, including the effect of the cell SiN_x antireflection coating on the textured cell. This reflection was estimated using transfer matrix calculations assuming the possibility of up to two reflections off of the pyramidal surface of the cell. The calculation assumes a 75 nm thick SiN_x coating on c-Si with C4-symmetric pyramidal texturing. The inclination angle of each face of the pyramid is 54.74° and cell is behind the EVA encapsulant.

Total reflection is calculated as a function of wavelength λ and angle of incidence (in air) θ made with the module normal. To keep the final result a function of only the angle θ, and because of the assumed C4 symmetry, reflection is averaged over $m_\varphi = 45$ azimuth angles φ equally spaced from 0 to 90 degrees, as shown in eq. A2. The reflection at a given azimuth angle is the average of reflection off of each of the four faces, weighted by the projected area of each face as seen by the incoming ray, shown in eq. A3. If the projected

area is negative (the incoming ray cannot see that face of the pyramid), then the projected area is replaced by zero.

$$R_{Total}(\lambda,\theta) = \frac{\sum_{\varphi=0}^{90} R(\lambda,\theta,\varphi)}{m_{\varphi}} \tag{A2}$$

$$R(\lambda,\theta,\varphi) = \frac{\sum_{i=1}^{4} R_i(\lambda,\theta,\varphi)\cdot \max(\cos(\alpha_i),0)}{\sum_{i=1}^{4} \max(\cos(\alpha_i),0)} \tag{A3}$$

All faces of the pyramid have equal area, therefore the projected area is proportional to the cosine of the angle that the incoming ray (after refraction into the encapsulant) makes with the surface normal of the pyramid face. The four surface normals are given in eq. A4a-d, where θ_{slope} is 54.74° and $\hat{x}$, $\hat{y}$, and $\hat{z}$ are the Cartesian unit vectors. The positive z-direction is defined as pointing away from the module towards the sky.

$$\hat{n}_1 = \sin(\theta_{slope})\hat{x} + \cos(\theta_{slope})\hat{z} \tag{A4a}$$

$$\hat{n}_2 = -\sin(\theta_{slope})\hat{x} + \cos(\theta_{slope})\hat{z} \tag{A4b}$$

$$\hat{n}_3 = \sin(\theta_{slope})\hat{y} + \cos(\theta_{slope})\hat{z} \tag{A4c}$$

$$\hat{n}_4 = -\sin(\theta_{slope})\hat{y} + \cos(\theta_{slope})\hat{z} \tag{A4d}$$

The projected area seen by the incoming ray, equal to the cosine of the angle of incidence the ray makes with a face of the pyramid, is given in eq. A5.

$$\cos(\alpha_i) = \hat{k}_{in} \cdot \hat{n}_i \tag{A5}$$

The unit vector pointing in the direction of travel of the incoming ray, $\hat{k}_{in}$, is given by eq. A6.

$$\hat{k}_{in} = \cos(\varphi)\sin(\theta_{refracted})\hat{x} + \sin(\varphi)\sin(\theta_{refracted})\hat{y} + \cos(\theta_{refracted})\hat{z} \tag{A6}$$

The angle of refraction, $\theta_{refracted}$, is determined via Snell's Law using the refractive index of the encapsulant, n_{EVA}.

$$\theta_{refracted} = \sin^{-1}\left(\frac{\sin(\theta)}{n_{EVA}(\lambda)}\right) \tag{A7}$$

It is possible that, after reflecting once off of one of the faces of the pyramid, an outgoing ray will reflect again off of the *opposite* face of the adjacent pyramid. The possibility of reflections off of other faces of the pyramid is ignored for simplicity. The unit vector in the direction of the outgoing ray, $\hat{k}_{out}$, (after the first reflection) is given in eq. A8, where the double bars indicate the vector magnitude.

$$\hat{k}_{out} = \frac{2\cdot\cos(\alpha_i)\cdot\hat{n}_i - \hat{k}_{in}}{\|2\cdot\cos(\alpha_i)\cdot\hat{n}_i - \hat{k}_{in}\|} \tag{A8}$$

The angle of incidence of the second reflection, β, is determined from $\hat{k}_{out}$ and the unit normal of the opposite pyramid face, as shown in eq. A9. For a first reflection off of face 1 ($\hat{n}_1$), the second reflection is off of face 2 ($\hat{n}_2$) and vice versa. Similarly, a ray that first reflected off of face 3 may reflect again from face 4, and vice versa.

$$\cos(\beta_i) = \hat{k}_{out} \cdot \hat{n}_{i,opposite} \tag{A9}$$

A second reflection is not necessarily guaranteed, depending on the direction of $\hat{k}_{out}$. If the z-component of $\hat{k}_{out}$ is negative (i.e. it points downwards), then another reflection is guaranteed. However, if $\hat{k}_{out}$ points upwards, then the chance that the ray reflects again (f_{Hit_chance}) is given by eq. A10a. The hit chance is estimated as the fraction of the area of the first pyramid face which would result in a second reflection if struck by an incident ray, and follows from the law of sines. Eq. A10a depends on the angle γ_i between the surface normal $\hat{n}_i$ and the unit vector, $\hat{k}_{in,proj}$, in the direction of the projection of $\hat{k}_{in}$ into the plane defined by $\hat{n}_i$ and $\hat{n}_{i,opposite}$, given by equations A10b and A10c, respectively.

$$f_{Hit\_chance} = \frac{\sin(2\theta_{slope} - 90 + \gamma_i)}{\sin(90 - \gamma_i)} \tag{A10a}$$

$$\gamma_i = \cos^{-1}\left(-1 \cdot \hat{k}_{in,proj} \cdot \hat{n}_i\right) \tag{A10b}$$

$$\hat{k}_{in,proj} = \frac{\hat{k}_{in} - \left(\hat{k}_{in} \cdot (\hat{n}_i \times \hat{n}_{i,opposite})\right)(\hat{n}_i \times \hat{n}_{i,opposite})}{\left\|\hat{k}_{in} - \left(\hat{k}_{in} \cdot (\hat{n}_i \times \hat{n}_{i,opposite})\right)(\hat{n}_i \times \hat{n}_{i,opposite})\right\|} \tag{A10c}$$

With all angles calculated, the first and second reflection coefficients, $R_{i,1}$ and $R_{i,2}$, are calculated via the transfer matrix method, represented as f_{TMM} in eqs. A11a-b.

$$R_{i,1}(\lambda, \theta, \varphi) = f_{TMM}(\lambda, \alpha_i) \tag{A11a}$$

$$R_{i,2}(\lambda, \theta, \varphi) = f_{TMM}(\lambda, \beta_i) \tag{A11b}$$

Finally, the reflection $R_i(\lambda, \theta, \varphi)$ is given by eq. A12a-b.

$$R_i(\lambda, \theta, \varphi) = R_{i,1}(\lambda, \theta, \varphi) \cdot R_{i,2}(\lambda, \theta, \varphi) \text{ if } \hat{k}_{out} \text{ points downwards} \tag{A12a}$$

$$R_i(\lambda, \theta, \varphi) = R_{i,1}(\lambda, \theta, \varphi) \cdot \left(R_{i,2}(\lambda, \theta, \varphi) \cdot f_{Hit\_chance} + 1 - f_{Hit\_chance}\right) \text{ if } \hat{k}_{out} \text{ points upwards} \tag{A12b}$$

The reflection calculated using eqs. A2 –A12 and a comparison to results from the ray tracer are shown in **Figure A3**. The angle of incidence is the angle that the light makes in air with the module normal. The ray tracer and the calculations described above do not

agree perfectly, however the agreement is good enough for the model. Note that the ray tracing results lose precision at wavelengths where AM1.5 spectral power is low.

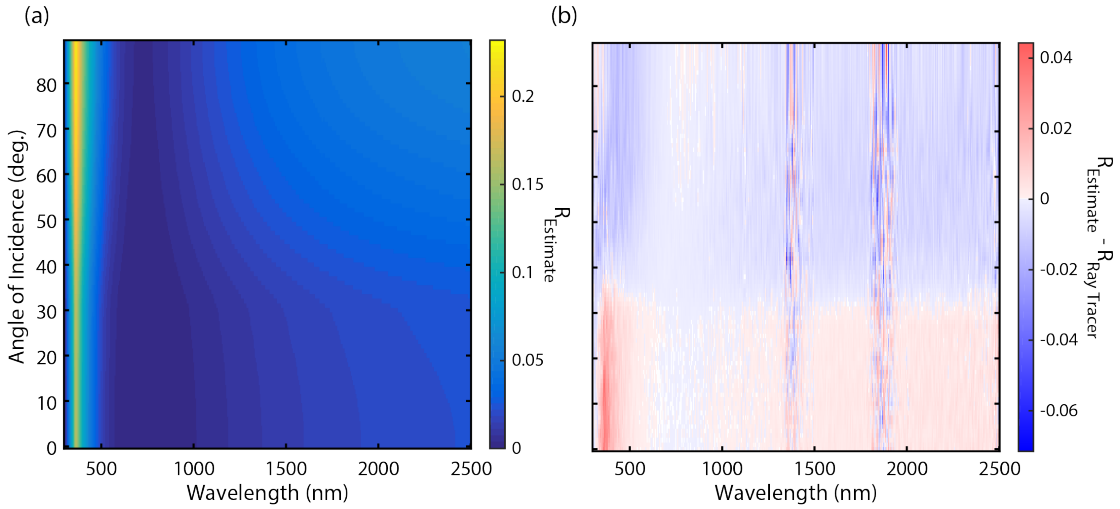

***Figure A3**: (a) Reflection of the SiN_x antireflection coating with pyramidal texture calculated using eqs. A2 – A12 as a function of wavelength and angle of incidence (in air). (b) Comparison of SiN_x antireflection coating reflection calculated using eqs. A2 – A12 and using the ray tracer.*

Mirrors Designed by the Time-Independent Matrix Model

Mirrors AG1, GE1, AG2, and AG3 were designed using an early version of the time-independent matrix model. Mirrors A and B were design using the time-independent matrix model as presented in Chapter 2.

Table A1: Designs on Mirrors AG1 and GE1

	Mirror AG1		**Mirror GE1**	
Layer #	Material	Thickness (nm)	Material	Thickness (nm)
1	SiO_2	116.6	SiO_2	232.2
2	TiO_2	19.1	TiO_2	5.2
3	SiO_2	17.4	SiO_2	56.9
4	TiO_2	109.5	TiO_2	12.1
5	Al_2O_3	25.2	SiO_2	29.5
6	TiO_2	16.5	SiN_x	162.7
7	Al_2O_3	185.1	SiO_2	38.3
8	TiO_2	8.0	TiO_2	9.9
9	Al_2O_3	21.6	SiO_2	229.8
10	SiN_x	117.8	TiO_2	9.2
11	Al_2O_3	26.0	SiO_2	38.2
12	TiO_2	7.6	SiN_x	156.7

13	Al_2O_3	192.6	SiO_2	37.2
14	SiN_x	155.7	TiO_2	9.1
15	Al_2O_3	36.3	SiO_2	221.5
16	TiO_2	5.7	TiO_2	9.1
17	Al_2O_3	136.2	SiO_2	37.4
18	TiO_2	5.4	SiN_x	155.6
19	Al_2O_3	37.2	SiO_2	37.4
20	SiN_x	150.2	TiO_2	9.1
21	Al_2O_3	37.7	SiO_2	222.5
22	TiO_2	5.5	TiO_2	9.2
23	Al_2O_3	139.0	SiO_2	37.6
24	TiO_2	5.8	SiN_x	157.9
25	Al_2O_3	36.8	SiO_2	38.5
26	SiN_x	149.6	TiO_2	9.4
27	Al_2O_3	33.8	SiO_2	233.9
28	TiO_2	5.8	TiO_2	10.2
29	Al_2O_3	159.2	SiO_2	39.0
30	TiO_2	6.3	SiN_x	167.9
31	Al_2O_3	34.3	SiO_2	33.2
32	SiN_x	165.1	TiO_2	12.9
33	SiO_2	33.0	SiO_2	64.1
34	SiN_x	24.9	TiO_2	4.9
35	-	-	SiO_2	234.0

Table A2: Design of Mirror AG2

Mirror AG2								
Layer #	Material	Thickness (nm)	Layer #	Material	Thickness (nm)	Layer #	Material	Thickness (nm)
1	Al_2O_3	96.6	12	SiN_x	121.3	23	Al_2O_3	26.8
2	TiO_2	114.1	13	Al_2O_3	22.0	24	SiN_x	137.6
3	Al_2O_3	24.1	14	TiO_2	6.5	25	Al_2O_3	32.7
4	TiO_2	14.3	15	Al_2O_3	163.2	26	TiO_2	5.4
5	Al_2O_3	175.2	16	TiO_2	6.3	27	Al_2O_3	141.7
6	SiN_x	144.2	17	Al_2O_3	23.1	28	TiO_2	5.4
7	Al_2O_3	32.8	18	SiN_x	119.8	29	Al_2O_3	34.2
8	TiO_2	3.9	19	Al_2O_3	24.6	30	SiN_x	157.2
9	Al_2O_3	136.2	20	TiO_2	6.5	31	SiO_2	31.3
10	TiO_2	5.7	21	Al_2O_3	158.6	32	SiN_x	23.1
11	Al_2O_3	27.1	22	TiO_2	5.3			

Table A3: Design of Mirror AG3

Mirror AG3					
Layer #	Material	Thickness (nm)	Layer #	Material	Thickness (nm)
1	Al_2O_3	99.4	6	TiO_2	3.5
2	TiO_2	119.4	7	Al_2O_3	20.7
3	Al_2O_3	25.0	8	SiN_x	158.1
4	TiO_2	13.8	9	SiO_2	31.7
5	Al_2O_3	175.1	10	SiN_x	21.9

Table A4: Designs of Mirrors A and B

	Mirror A		**Mirror B**	
Layer	**Thickness (nm)**	**Material**	**Thickness (nm)**	**Material**
1	111.5	SiO_2	112.5	SiO_2
2	19.9	TiO_2	16.1	TiO_2
3	14.6	SiO_2	23.4	SiN_x
4	100.8	TiO_2	94.7	TiO_2
5	27.0	SiO_2	26.1	MgF_2
6	17.2	TiO_2	17.0	TiO_2
7	216.9	SiO_2	201.1	SiO_2
8	5.9	TiO_2	65.2	SiN_x
9	54.1	SiN_x	103.9	TiO_2
10	110.4	TiO_2	27.8	SiO_2
11	12.3	SiO_2	16.8	TiO_2
12	57.9	SiN_x	220.0	SiO_2
13	220.2	SiO_2	15.3	TiO_2
14	-	-	33.2	Al_2O_3
15	-	-	117.8	TiO_2
16	-	-	20.4	SiO_2
17	-	-	21.6	TiO_2
18	-	-	41.8	SiO_2
19	-	-	22.5	SiN_x
20	-	-	215.8	SiO_2

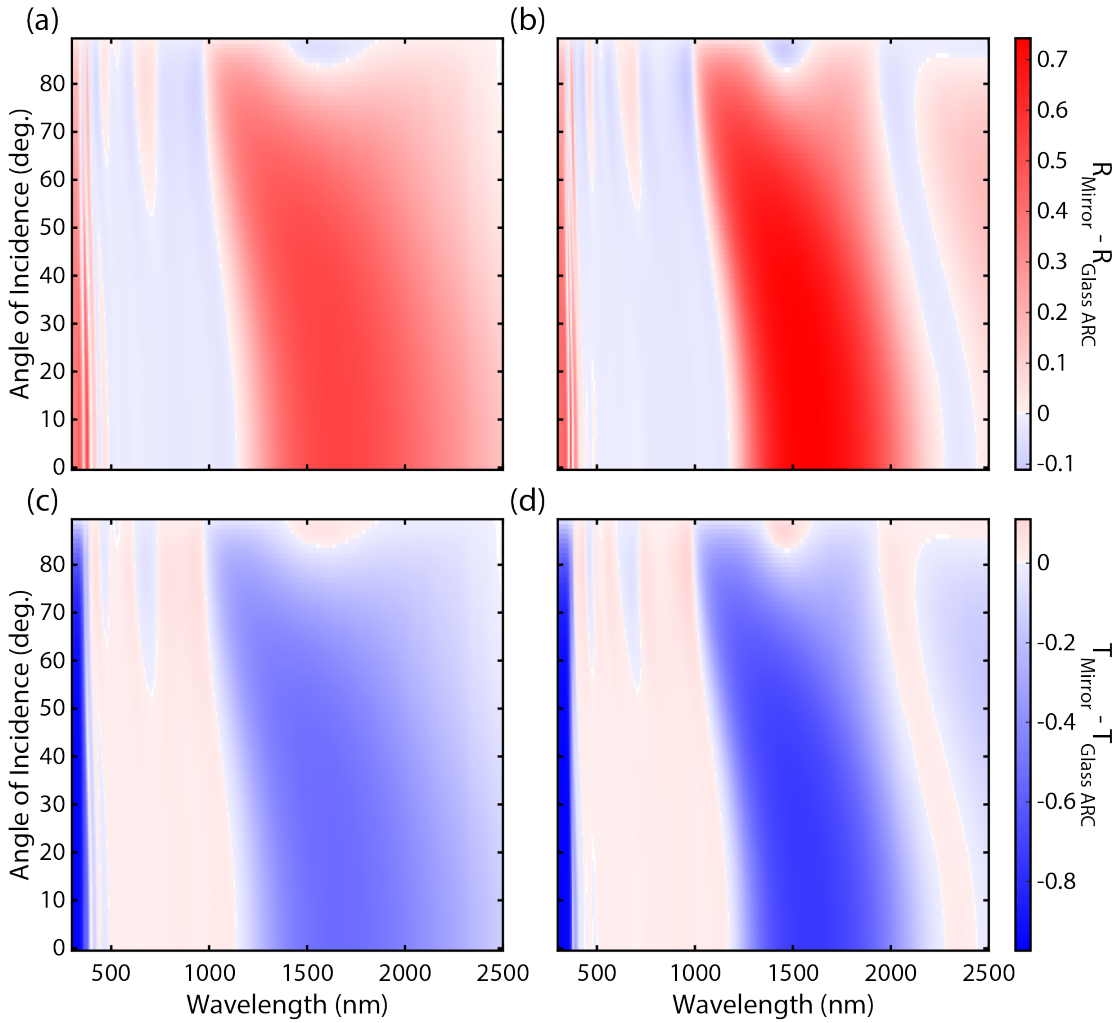

Figure A4*: Net Reflection of a) mirror A and b) Mirror B, and net transmission of c) mirror A and d) mirror B compared to a single layer ARC. Plots are shaded such that red regions refer to wavelengths and angles of incidence where reflection or transmission is increased, blue regions refer to decreased reflection or transmission.*

Figure A4 above demonstrates that Mirror A and Mirror B both offer optical and thermal advantages over glass coated with a single-layer ARC.